Systematic investigations of calcium phosphates produced by wet chemistry method and supercritical processing techniques

by Midhat Nabil Ahmad Salimi

A thesis submitted to the School of Chemical Engineering of the

University of Birmingham

for the degree of

Doctor of Philosophy

Chemical Engineering

University of Birmingham

Edgbaston, Birmingham

B15 2TT, UK

Abstract

Calcium phosphate (CaP) based material, especially hydroxyapatite (HAp) nanoparticles have a wide range of applications in a number of fields, such as drug delivery, gene therapy, bone cements, dental applications, chromatography and waste water remediation. Depending on the application, there is often a need for the nanoparticles to be in a particular size range. One of the potential applications of HAp is for drug delivery; as a transfection vector in specific. The main aim of this study was to evaluate the potential of various produced CaP nanoparticles for this matter. The HAp and CaP nanoparticles in this study were systematically investigated and produced by several methods, firstly by the wet chemistry method of sol-gel, where the process conditions of varying its stirring rates and temperatures were taken into consideration; secondly by the supercritical fluid techniques of Gas Anti-Solvent (GAS) and Solution Enhanced Dispersion of Supercritical Fluids (SEDS), where the process conditions of varying the processing temperature, pressure and supply of antisolvent flowrate were investigated. Lastly, several phases of CaPs were produced by a systematic investigation of CaP precipitation processes (*via* direct precipitation method and SEDS processing technique) by varying the Ca/P ratios. The processing conditions such as the stirring rate, temperature, pressure and antisolvent flowrate played a significant role on the nanoparticle size and morphology. The produced HAp and CaP nanoparticles were then complexed with plasmid DNA (pDNA) to evaluate the pDNA binding efficiencies and thus their potential as a transfection vector in NIH/3T3 fibroblastic and MC3T3 osteoblastic cell lines *via in-vitro* transfection study. It had been shown that the particle size played a significant role on the pDNA binding efficiencies and also on the green fluorescence protein (GFP) expression in the transfection results obtained.

Acknowledgments

This thesis would not have been possible unless with the superior encouragement, guidance and support from my wonderful supervisors, Dr. Gary A. Leeke, Dr. Liam M. Grover and Dr. Rachel H. Bridson, from the initial to the final level enabled me to develop an understanding of the subject.

I would like to thank to the academic staff in the School of Chemical Engineering, including Dr. Ping Ding, Dr. Shangfeng Du and Dr. James Bowen. I would also like to thank Dr. Adrian Wright who is in the School of Chemistry for the usage of the XRD facility. I would like to express my gratitude to all technicians and staff who have helped with a number of aspects of my PhD in Biochemical Engineering, School of Chemistry and Centre for Microscopy. Especially, thank to Dr. Jennifer Paxton, Mrs. Elaine Mitchell and Mrs. Theresa Morris.

Most importantly, I would like to thank my parents, Dato' Haji Ahmad Salimi Ismail and Datin Badriyah Md. Tamin who are always near to my heart and for their continuing emotional support and encouragement.

Lastly, I offer my regards and blessings to all of those who supported me in any respect during the completion of the project, especially to Norsyafina Roslan, who had been through thick and thin of this wonderful journey.

Thank you.

Table of contents

List of Figures

List of Tables

1.0 Introduction

Specific characteristics of particles (size, shape, surface, crystal structure and morphology) are among the important factors needed to control technological and biopharmaceutical properties of drug products. In general, morphology (crystal habit) can influence the physical and chemistry stability of solid dosage forms, a narrow size distribution is important to obtain content uniformity, while spherical particles allow good flowability and tablettability. Furthermore, micronisation increases the surface area with a consequent increase of dissolution rate and bioavalability of the drug, thus promoting the formulation of active principle ingredients which may be insoluble or slightly soluble in aqueous media.

1.1 The production of calcium phosphate for biomedical usage

Calcium phosphate nanoparticles have a range of applications in a number of fields, such as drug delivery, gene therapy, bone cements, dental applications, chromatography and waste water remediation. Each application has a need for the nanoparticles to be of a particular size range. There are various techniques reported in the literature for the production of nanosized calcium phosphate particles. These include mechano-chemical synthesis [Kano et al. (2006)], combustion preparation [Tas (2000)], and various wet chemistry techniques, such as direct precipitation from aqueous solutions [Rodriquez-Clemente et al. (2000)], sol-gel procedures [Weng & Baptista (1997)], hydrothermal preparation [Yoshmura et al. (1994)] and emulsion synthesis routes [Lim et al. (1999)]. The production of this material by supercritical fluid processing has never been reported. It is anticipated that by this method, particles can be produced with higher purity, different morphology, narrow size distribution and fewer processing steps.

1.2 Objectives of the Present Work

The objectives of this work were firstly to examine the literature and summarise the background to supercritical fluid technology and the work carried out to date in the area of particle formation. Secondly, to construct a suitable apparatus to study the production of calcium phosphate based biomaterial powders using supercritical carbon dioxide as an anti-solvent under various conditions. These powders were to be characterised using a variety of analytical techniques to obtain information on their physical properties such as its chemical phase, functional groups, particle size and morphology. Objectives also cover the investigations of process parameters of wet chemistry precipitation, the comparison of particles produced by wet chemistry precipitation to supercritical fluid (SCF) processing and loading of calcium phosphate (CaP) particles with plasmid DNA (pDNA) to test efficacy as potential gene vector in *in vitro* transfection studies.

2.0 Literature Survey

2.1 Types of calcium phosphates

Calcium phosphates are of interest for many biomedical applications owing to their good biocompatibility and bioactivity. Hydroxyapatite (HAp) has been used in implant coatings [Sun et al. (2001)] and bone substitutes [LeGeros (1991)]. Amorphous calcium phosphate (ACP) are used as remineralisation agents both *in-situ* [Tung et al. (1997)] and in tooth restorative materials [Skrtic et al. (2004)]. Dicalcium phosphate anhydrous (DCPA) and dicalcium phosphate dehydrate (DCPD) [Brown & Chow (1986)], octacalcium phosphate (OCP) [Bermudez et al. (1994)] and other calcium phosphate compounds [Mejdoubi et al. (1994), Ginebra et al. (1997), Lee et al. (1999)] are used either as components or form as products of calcium phosphate bone cements.

Previous studies on nano-calcium phosphates have focused almost exclusively on nano-HAp, primarily because it is considered as a prototype of bioapatites, which are in nano-crystalline forms [LeGeros (1991)]. Most of these preparations were done in a solution environment, such as chemical precipitation [Tas (2000) & Bertoni et al. (1998)], sol-gel [Chai & Ben-Nissan (1994) & Layrolle et al (1998)], microemulsion [Bose & Saha (2003) & Lim et al. (1999)], electro-deposition [Shirkhanzadeh (1998)], and mechanochemical preparation followed by hydrothermal treatment [Suchanek et al. (2004)]. These methods generally can be used for preparing nano-HAp only because HAp is the least soluble calcium phosphate under most solution conditions; hence it is the phase that would form exclusively [Dorozhkin (2007 &

2009)]. Nanoparticles of the more soluble calcium phosphate phases, such as monocalcium phosphate monohydrate (MCPM), dicalcium phosphate monohydrate (DCPA), dicalcium phosphate dehydrate (DCPD), octacalcium phosphate (OCP), and amorphous calcium phosphate (ACP) have not been prepared by these methods. Their preparations are discuss in respective calcium phosphate phase later in this chapter.

In this section, the details of the existing calcium phosphates are briefly explained, with respect to their properties and synthesis process methods. Some particle characterisation techniques are also explained.

2.1.1 Calcium phosphates

By definition, all calcium orthophosphates consist of three major chemical elements; calcium (oxidation state +2), phosphorus (oxidation state +5) and oxygen (reduction state -2), as part of orthophosphate anions. There are a large variety of calcium phosphates in existence, which are distinguished by the type of the phosphate anion: ortho- (PO_4^{3-}), meta- (PO_3^-) or pyro- ($P_2O_7^{4-}$) and poly- ($(PO_3)n^{n-}$). Several phases of crystallised calcium phosphates can be formed which depend on temperature, partial pressure of water and impurities [Dorozhkin (2009)]. The different phases of calcium phosphate are summarised in Table 2.1. It is interesting to note that, the lower the Ca/P molar ratio, the more acidic and water soluble the calcium phosphate is, due to the solubility criteria and the kinetics of precipitate formation and transformation [Elliott (1994)]. The solubility isotherm profile shown in Figure 2.1 indicates the likely conditions required for synthesis of a variety of calcium phosphates. The saturation boundary is represented

by the curve of each phosphate composition. The calcium phosphate compositions below the curve are supersaturated, whereas those above are under-saturated. From the figure, it can be seen that hydroxyapatite (HAp) is the least soluble calcium phosphates at a pH value of > 4.2 (the most stable calcium phosphate phase). Therefore, above this pH all calcium phosphates are likely to hydrolyse to HAp.

Ca/P ionic ratio	Compound	Chemical formula	Solubility at 25 °C, -log (K_s)	pH stability range in aqueous solutions at 25 °C
0.5	Monocalcium phosphate monohydrate (MCPM)	$Ca(H_2PO_4)_2.H_2O$	1.14	0.0 – 2.0
0.5	Monocalcium phosphate anhydrous (MCPA)	$Ca(H_2PO_4)_2$	1.14	[c]
1.0	Dicalcium phosphate dehydrate (DCPD), mineral brushite	$CaHPO_4.2H_2O$	6.59	2.0 – 6.0
1.0	Dicalcium phosphate anhydrous (DCPA), mineral monetite	$CaHPO_4$	6.90	[c]
1.33	Octacalcium phosphate (OCP)	$Ca_8(HPO_4)_2(PO_4)_4.5H_2O$	96.6	5.5 – 7.0
1.5	α-Tricalcium phosphate (α-TCP)	α-$Ca_3(PO_4)_2$	25.5	[a]
1.5	β-Tricalcium phosphate (β-TCP)	β-$Ca_3(PO_4)_2$	28.9	[a]
1.2 – 2.2	Amorphous calcium phosphate (ACP)	$Ca_xH_y(PO_4)_z.nH_2O$, n = 3 – 4.5; 15 – 20% H_2O	[b]	~ 5 – 12
1.5 – 1.67	Calcium – deficient hydroxyapatite (CDHA)[e]	$Ca_{10-x}(HPO_4)_x(PO_4)_{6-x}(OH)_{2-x}$ (0<x<1)	~ 85.1	6.5 – 9.5
1.67	Hydroxyapatite (HAp)	$Ca_{10}(PO_4)_6(OH)_2$	116.8	9.5 – 12
1.67	Fluorapatite (FAp)	$Ca_{10}(PO_4)_6F_2$	120.0	7 – 12
2.0	Tetracalcium phosphate (TTCP), mineral hilgenstockite	$Ca_4(PO_4)_2O$	38 - 44	[a]

[a] These compounds cannot be precipitated from aqueous solutions.
[b] Cannot be measured precisely. However, the following values were found: 25.7 ± 0.1 (pH = 7.40), 29.9 ± 0.1 (pH = 6.00), 32.7 ± 0.1 (pH = 5.28).
[c] Stable at temperatures above 100 °C.
[d] Always metastable.
[e] Occasionally, CDHA is named as precipitated HAp.

Table 2.1 Existing calcium orthophosphates and their major properties [reproduced from Dorozhkin (2009)].

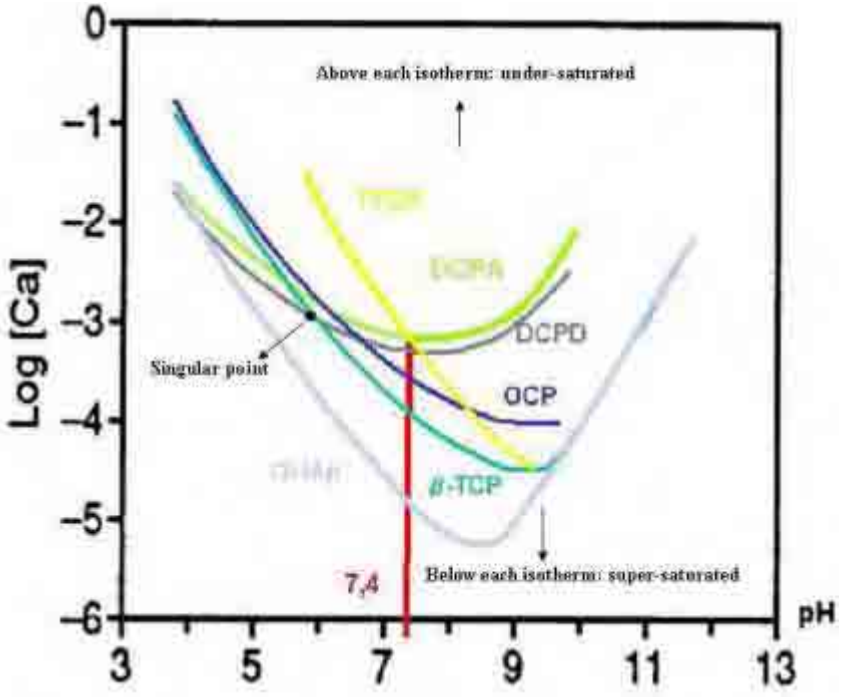

Figure 2.1 Solubility isotherm of calcium phosphate phases in the ternary system $Ca(OH)_2$-H_3PO_4-H_2O at 37 ^oC; log [Ca] versus pH [reproduced from Hoffmann (2003)].

Variations in pH alter the relative concentrations of the four polymorphs of orthophosphoric acid (Figure 2.2) and thus both the chemical composition and the amount of calcium orthophosphates that forms by direct precipitation [Lynn & Bonfield (2003)].

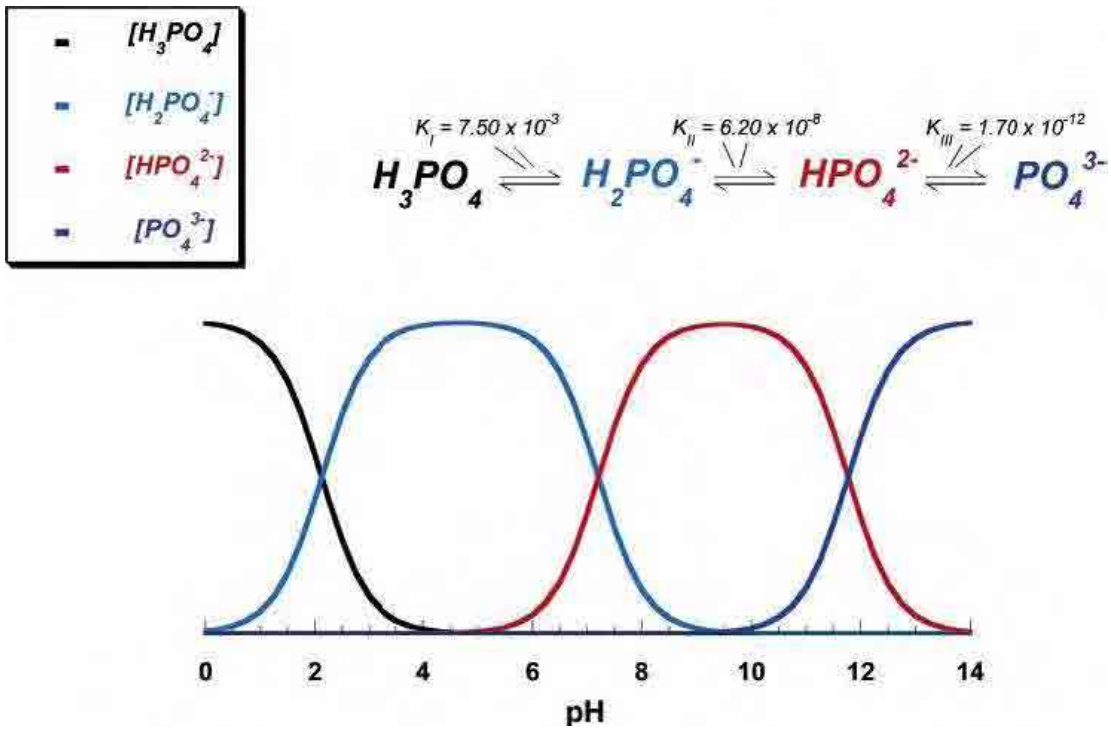

Figure 2.2 pH variation of ionic concentration for phosphoric acids solutions [Lynn & Bonfield (2003)].

2.1.2 Monocalcium phosphate (monohydrate and anhydrous)

Monocalcium phosphate can either form the monohydrate (MCPM) or anhydrous salt (MCPA). MCPM has a chemical formula of $Ca(H_2PO_4)_2.H_2O$ and its chemically correct name is calcium dihydrogen phosphate monohydrate. Meanwhile, MCPA has a chemical formula of $Ca(H_2PO_4)_2$ and its chemically correct name is calcium dihydrogen phosphate anhydrous. With a Ca/P ratio of 0.5, MCPM and MCPA are the most acidic and water soluble calcium phosphates as shown on Table 2.1 [Dorozhkin (2009)].

MCPM can be produced by the 'triple superphosphate' reaction for phosphorus-containing fertilizer production [Becker (1989)]. In this process, MCPM is produced by the reaction of concentrated phosphoric acid with powdered phosphate rock. At temperatures above 100 ^oC, it releases a molecule of water and transforms into MCPA.

The presence of MCPM and MCPA can be distinguished from the peaks of an XRD pattern at 7^o, 23 - 24^o, and 24 - 26^o 2θ. In addition, the HPO_4^{2-} group is present at 870 cm^{-1} in the FTIR spectrum. Both have the crystallographic structure of triclinic space group.

Although MCPM is not biocompatible (due to being the most acidic calcium phosphate compound), in medicine, it is used as a component of several self-hardening calcium orthophosphate cements [Bermudez et al. (1994)]. There is no current application of MCPA in medicine.

2.1.3 Dicalcium phosphate (dehydrate - brushite and anhydrate - monetite)

Dicalcium phosphate dihydrate (DCPD) or better known as the mineral brushite can easily be crystallised from aqueous solutions at pH <6.5. Briefly, DCPD crystals consist of $CaHPO_4$ chains arranged parallel to each other, while lattice water molecules are interlayed between them. DCPD can be precipitated by mixing a calcium hydroxide, $Ca(OH)_2$ suspension and an orthophosphoric acid, H_3PO_4 solution in equimolar quantities at room temperature [Oliveira et al. (2007)]. DCPD is also formed by neutralising dilute H_3PO_4 by the addition of calcium sucrate (calcium carbonate and sucrose) [St. Pierre (1995)]. It transforms into dicalcium phosphate anhydrous (DCPA) at temperatures above 80 ^oC. DCPD has the crystallographic structure of monoclinic space group. In medicine, DCPD is used in calcium orthophosphate cements [Bermudez et al. (1994)] and as an intermediate for tooth remineralisation. DCPD is added to toothpaste both for dental caries protection (it is coupled with F-containing compounds such as NaF and/or Na_2PO_3F) and as a gentle polishing agent [Crall & Bjerga (1987)].

Meanwhile, dicalcium phosphate anhydrous (DCPA) or better known as the mineral monetite is the anhydrous form of DCPD. It is less soluble than DCPD due to the absence of water inclusions. Unlike DCPD, DCPA occurs in neither normal nor pathological calcifications. DCPA has the crystallographic structure of triclinic space group. It is used in calcium phosphate cements [Takagi et al. (1998)]. Other applications include uses as a polishing agent, a source of calcium and phosphate in nutritional supplements, a tabletting aid and a toothpaste component [Budavari et al. (1996)].

2.1.4 Octacalcium phosphate

Octacalcium phosphate (OCP) has a chemical formula of $Ca_8(HPO_4)_2(PO_4)_4.5H_2O$ and is often found as an unstable transient intermediate during the precipitation of the thermodynamically more stable HAp in aqueous solutions. OCP has a similar structure to HAp, in which it has apatitic layers separated by hydrated layers [LeGeros (1991) & Elliot (1994)].

OCP can be synthesised by means of homogeneous crystallisation, where a solution of calcium nitrate tetrahydrate and disodium hydrogen orthophosphate are held at temperatures between 45 and 55 ^oC and a pH between 6.49 and 7.15 for 48 h [Shelton et al. (2006)]. Pure OCP can be precipitated by the addition of calcium acetate to an equal volume of sodium and phosphorus at pH 4.5 at 70 ^oC for 1 h or pH 4 at 80 ^oC for 1 h [LeGeros (1985)]. OCP hydrolyses to HAp in water, depending on the availability of calcium ions [Elliot (1994)]. The hydrolysis reaction is represented by the chemical formula:

$$Ca_8H_2(PO_4)_65H_2O + 2Ca^{2+} \rightarrow Ca_{10}(PO_4)_6(OH)_2 + 3H_2O + 4H^+ \qquad \textbf{Equation 2.1}$$

OCP has the crystallographic structure of triclinic space group. Intense peaks for OCP on the XRD patterns are at 26^o and 32^o 2θ. It exhibits HPO_4^{2-} bands at 865 and 910 cm^{-1} on FTIR spectra.

2.1.5 Tricalcium phosphates and whitlockite

Tricalcium phosphates (TCPs) can exist in either α-TCP or β-TCP crystal form. β-TCP cannot be precipitated from aqueous solutions. β-TCP can be prepared by addition of Na_3PO_4 solution to a $CaCl_2$ solution at a Ca/P molar ratio of 1.5. The reaction conditions are at pH value of 9 and temperature of 5 ^oC. As it is a high temperature phase, β-TCP can also be prepared by thermal decomposition (> 800 ^oC) of calcium defficient HAp (CDHAp) or by solid-state interaction of acidic calcium orthophosphates, *e.g.*, DCPA with a base, *e.g.*, CaO. Apart from the chemical preparation route, ion-substituted β-TCP can be prepared by calcining bones: such types of β-TCP are occasionally called "bone ash" [Dorozhkin (2009)]. α-TCP is stable at temperatures between 1180 – 1400 ^oC and is formed by the phase transformation of β-TCP. At temperatures above ~ 1125 ^oC, β-TCP transforms into the high-temperature phase, α-TCP. Whitlockite is the Mg-substituted form of β-TCP.

Although α-TCP and β-TCP have exactly the same chemical composition, they differ in term of their solubility, where β-TCP is found to be more stable than the α-phase [Yin et al. (2003)]. Hence, α-TCP is more reactive in aqueous systems, has higher specific energy and can be hydrolysed to a mixture of other calcium phosphates. α-TCP has the crystallographic structure of monoclinic space group, meanwhile, β-TCP has the crystallographic structure of rhombohedral space group.

β-TCP is widely used as calcium orthophosphate bone cements [Mirtchi et al. (1990)], gentle polishing agent in toothpaste and complexes in multivitamin. Meanwhile, α-TCP is used mainly as calcium orthophosphate cements [Bermudez et. al. (1994)]. In terms of FTIR

analysis, the phosphorus absorption (P-O) is present at 600 cm^{-1} as a single band for α-TCP, but at 550 and 616 cm^{-1} as split bands for β-TCP. For whitlockite, there is a P-OH stretching band at 850 cm^{-1} [Elliott (1994)]. In terms of XRD, it is denoted by the peak occurring at 22^{o} and the overlapping of peaks at 2θ range of $31.7 – 33^{o}$.

2.1.6 Hydroxyapatite

Hydroxyapatite (HAp) has the chemical formula of $Ca_5(PO_4)_3(OH)$, but is usually written as $Ca_{10}(PO_4)_6(OH)_2$ as to denote that the crystal unit cell comprises of two molecules. HAp is the second most stable and least soluble calcium orthophosphate in water with a K_s of –log 116.8 after fluoroapatite, FAp; K_s of –log 120.0 (refer to Table 2.1). Pure HAp has a stoichiometric Ca/P ratio of 1.67, above this, it indicates the presence of calcium rich HAp or carbonated HAp, whereas, a Ca/P ratio below 1.67 indicates the apatite is calcium deficient or contains other impurity phases [Hench and Wildson (1993)]. HAp has attracted significant interest as a biomaterial because of its similarity in composition to the mineral component of bone [Shi (2004)]. A table comparing both compositions is shown on the next page (Table 2.2):

Composition	Bone (wt%)	HAp (wt%)
Calcium as C	34.80	39.60
Phosphorus as P	15.20	18.50
Ca/P (molar ratio)	1.71	1.67
Sodium	0.90	-
Magnesium	0.72	-
Potassium	0.03	-
Carbonate as CO_3^{2-}	7.4	-
Fluoride	0.03	-
Chloride	0.13	-
Pyrophosphate as $P_2O_7^{4-}$	0.07	-
Total inorganic components	65	100
Total organic components	25	-
H_2O	10	-

Table 2.2 Chemical composition of human bone and HAp [reproduced from Dorozhkin et al. (2007)].

Several techniques can be used for HAp preparation, in general, they can be divided into solid-state reactions (materials chemistry) and wet methods [Briak-Ben et al. (2008)], which include precipitation, hydrothermal and hydrolysis of other calcium orthophosphates. One of the wet methods is by mixing exact stoichiometric quantities of Ca- and PO_4- containing solutions at pH > 9, followed by boiling for several days in CO_2-free atmosphere (the ageing or maturation stage), followed by filtration, drying and, usually sintering at about 1000 ^oC [LeGeros (1993)].

To obtain stoichiometric HAp (s-HAp) by direct precipitation, the reactants used must be H_3PO_4 and $Ca(OH)_2$ or salts of calcium and phosphates with ions such as nitrates or ammonium, which are unlikely to be incorporated in the apatitic phase. Because of the low solubility of apatites, if the calcium and phosphate ions have exact molar values in the reaction medium, s-HAp can be obtained.

In the sol-gel technique, HAp powder is obtained by reacting phosphoric pentoxide (P_2O_5) and calcium nitrate tetrahydrate ($Ca(NO_3)_2.\ 4H_2O$). In this technique, a sintering step at 600 ^oC was included as to obtain s-HAp [Feng et al. (2005)]. In hydrothermal precipitation, HAp whiskers were prepared by a precipitation-hydrolysis method in moderately acid solutions at a temperature between 85 to 95 ^oC for 48 to 120 h [Zhang et al. (2003)]. In emulsion synthesis of HAp, calcium hydroxide, $Ca(OH)_2$ aqueous solution was mixed with potassium dihydrogenphosphate (KH_2PO_4) for 24 h under intense agitation at 50 ^oC and calcined at 650 ^oC for 1 h [Sonoda et al. (2002)].

Hydroxyapatite can be synthesised through solid-state reaction by using calcium pyrophosphate ($Ca_2P_2O_7$) and calcium carbonate ($CaCO_3$). The two powders were mixed in acetone and water, respectively, and the single phase of hydroxyapatite was observed to occur during heat treatment at 1100 ^oC for 1 h [Rhee (2002)].

The deposition of HAp coatings onto prostheses can be accomplished by spontaneously nucleating and growing HAp using metastable synthetic body fluids composed of an inorganic salt composition [Ferraz et al. (2004)]. The thickness of HAp coating is usually in

the range of 200 to 400 μm. Other techniques of HAp coating include plasma spraying, sputter coating, laser deposition and sol-gel processing. Plasma spraying uses a stream of gas such as pure argon or a mixture of argon and other gases to carry HAp powders, which are then passed through plasma produced using a low voltage, and high current electrical discharge. Plasma spraying, however has its own problems including: binding between coatings and the substrates, and the alteration of HAp structure [Yang et al. (2005)]. Like plasma spraying, sputter coating deposits HAp layers on the substrate, but with low pressure during sputtering. Laser deposition uses an active medium to produce the optical gain under proper pumping conditions, and the optical resonator is composed of a pair of mirrors and reflects to produce optical feedback and amplified beam [Paital et al. (2008)].

The crystallographic structure of HAp could either be monoclinic or hexagonal space group. The FTIR spectra of HAp has been summarised in Table 1.3 [Elliot (1994)]. HAp has a characteristic HPO_4^{2-} ion adsorption at 870 cm^{-1}. However, the carbonate ion absorption appears at 870 cm^{-1} because of the out-of-plane stretching. Therefore, it will interfere with the analysis of HAp. In addition to PO_4^{3-} bands, the OH^- band is expected at 3600 cm^{-1}.

Sample	PO_4^{3-} ν1 Stretching mode (cm^{-1})	PO_4^{3-} ν2 Vibration mode (cm^{-1})	PO_4^{3-} ν3 Stretching mode (cm^{-1})	PO_4^{3-} ν4 Bending mode (cm^{-1})	CO_3^{2-} ν2 Vibration mode (cm^{-1})	CO_3^{2-} ν2 Stretching mode (cm^{-1})	CO_3^{2-} ν2 Bending mode (cm^{-1})	OH^- Rotary mode (cm^{-1})
HAp	963	470	1029 1092	536 603	876	-	-	635 679
CHAp	960	-	1023	561 603	875	1409 1486	-	-

Table 2.3 Positions of different vibrations of hydroxyl, phosphate, and carbonate in FTIR analysis of HAp and carbonated substituted apatite (CHAp).

HAp is widely used as a coating on orthopaedic prostheses, and also with biological components (*e.g.* pDNA) for drug delivery due to the similarity to bone and teeth [Dorozhkin (2007)].

2.1.7 Tetracalcium phosphate (Hilgenstockite)

Tetracalcium phosphate (TTCP or TetCP) has a Ca/P ratio of 2.0 and is the most basic among all of the existing calcium phosphate orthophosphates. However, its solubility in water is higher than that of HAp. TTCP can not be synthesised in an aqueous environment (owing to the oxygen atom in its formula, $Ca_4(PO_4)_2O$ [Jalota et al. (2005)], precipitates formed in basic aqueous solutions will incorporate hydroxyl ions, and therefore, always consist of carbonate- and/or hydroxyl ion-containing apatitic phases. Hence, common methods for the synthesis of TTCP are limited to solid-state reactions at high temperatures [Matsuya et al. (1999)]. These methods are usually based on mixtures of calcium carbonate ($CaCO_3$) and dicalcium phosphate anhydrate ($CaHPO_4$), which are then heated to 1400 – 1500 ^oC for 6 – 12 h. The reaction is given by the following equation:

$2CaHPO_4 + 2CaCO_3 \rightarrow Ca_4(PO_4)_2O + 2CO_2 + H_2O$ **Equation 2.2**

After heating, the mixture must be rapidly quenched to room temperature in order to avoid the formation of undesired secondary phases, such as HAp, CaO, $CaCO_3$ and β-TCP. TTCP has the monoclinic space group.

Miao et al. [Miao et al. (2204)] have reported on the use of TTCP as scaffolds in tissue engineering.

2.2 Particle formation

In a crystallisation process, size and morphology are regarded as important properties of the crystalline product. One of the main aims of the crystallisation process can be for the synthesis of single crystals of very small size, if a high specific surface area is the desired property. Crystallisation process involves complex mechanisms but its theories can be simplified into 3 major steps which are achievement of supersaturation or supercooling, nucleation (formation of crystal nuclei) and crystal growth [Mackellar et al. (1994)]. The achievement of supersaturation can be done by cooling or evaporating a solution or by the addition of other substance(s), such that a deviation from equilibrium solubility is achieved. The crystal development is initiated by the collision of molecules of solute that form embryos [Florence & Attwood (1998)]. When solute molecules aggregate around each other and when nuclei occur spontaneously, nucleation is termed homogeneous. Embryos can also be formed by the addition of a seed crystal, a dust particle or by migrated particles from a container's wall. This is termed heterogeneous nucleation and occurs when nuclei are induced artificially. Homogeneous and heterogeneous mechanisms form the primary nucleation [Mullin (2000)]. Surface energy, temperature and supersaturation are the most important variables that affect nucleation [Myerson & Ginde (1993)]. In heterogeneous nucleation, the consequences of added solid particles reduce the surface free energy and thus induce nucleation.

Secondary nucleation results from the presence of solute particles in a supersaturated solution [Boistelle & Astier (1998)]. The solute crystals catalyse the nucleation; hence, nucleation occurs at relatively low supersaturation. Secondary nucleation has been recognised as being the major source of nuclei in many industrial crystallisers.

The next step of nucleation in a crystallisation process is crystal growth. The crystal growth is governed by a 4-step process, by which a growth unit passes from the bulk solution to the crystal lattice. Initially, the growth unit moves from the bulk solution to the crystal surface, where it adsorbs onto the surface. Then, possible diffusion of the growth units to a more favourable site may occur. Finally, growth units integrate into the crystal lattice [Zipp & Rodríguez (1993)]. The rate-limiting steps for crystal growth are generally considered to be the rate of transport of growth units to the crystal surface (diffusion-controlled) and/or integration into the crystal lattice [Mackellar et al. (1994)].

Adsorption of the crystal forming elements (depicted as a cube) on the surface structure of a growing crystal may occur at three possible sites [Sangwal (1998)]:

[1] Ledge sites (incorporation at a flat surface (terrace) having only one site of intermolecular interaction available),

[2] Step sites (incorporation at a surface having two sites of intermolecular interactions available), or

[3] Kink sites (three possible sites of intermolecular interactions).

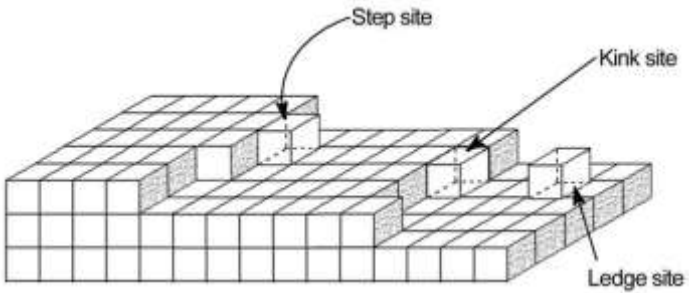

Figure 2.3 Incorporation of crystal forming elements on the surface of a growing crystal [Sangwal (1998)].

Because crystal forming elements with the highest coordination number are bound most strongly to the surface, incorporation at a kink site will provide a new kink site; the kink site is thus a 'repeatable-step' in the formation of the crystal. For example, HAp ($Ca_{10}(PO4)_6(OH)_2$) has Ca^{2+} as its central cation, which has a coordination number of 8. Crystal growth can follow two possible mechanisms, two-dimension nucleation or spiral growth at screw-dislocations. In two-dimension growth, before growth can occur a monolayer island nucleus, usually called a 'two-dimensional nucleus', must come into existence on an existing layer (Figure 2.4 a). This island becomes the source of new steps and kink sites at which additional units can join the surface. Subsequent crystal forming elements will tend to incorporate at sites where attractive forces are greatest, *i.e.* they will migrate towards the energetically favourable kink sites (Figure 2.4 b). The step-growth will advance until the whole plane is completed (Figure 2.4 c) and a new two-dimensional nucleus has to be generated before growth can advance [Mullin (1961), Garside & Davey (2000)].

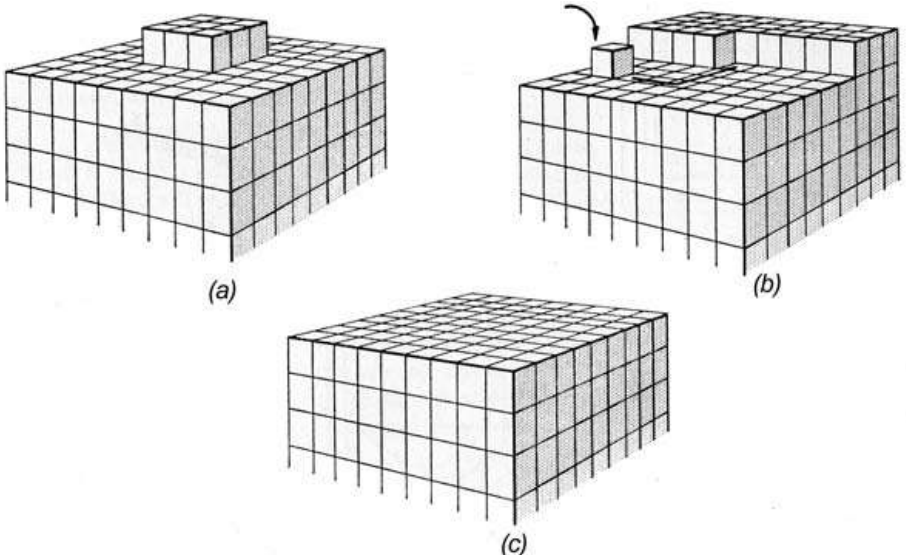

Figure 2.4 a – c Two dimensional growth [Mullin (1961)].

At low supersaturation, growth occurs along screw dislocations (Burton-Cabrera-Frank (BCF) model) [Burton et al. (1951)]. This model (Figure 2.4 a, b and c) is based on a defect in the structure of the crystal lattice formed by stress inside the crystal lattice, which produces spiralling mounds. From Figure 2.5, it can be seen that these screw dislocations in the crystal are a continuous source of new steps and that this screw mechanism provides a way for steps to grow uninterrupted.

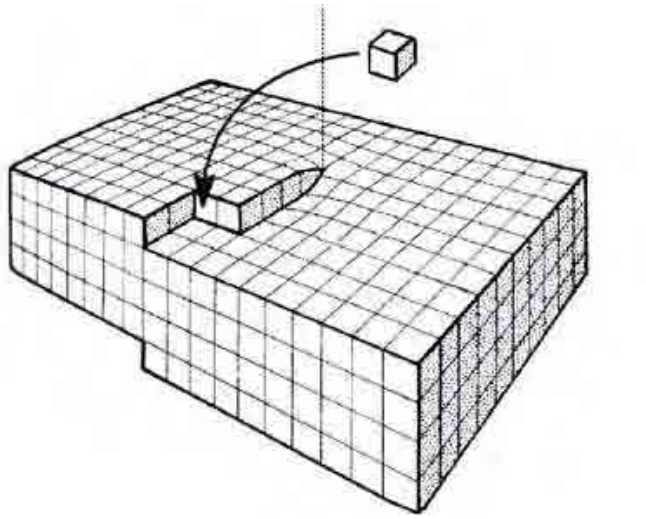

Figure 2.5 Spiral growth from a screw [Burton et al. (1951)].

Significant changes in the particle size, shape and purity can be due to minor changes of the crystallisation conditions, such as supersaturation, cooling rate and impurities. A condition where supersaturation is very high and fast will dramatically affect the nucleation rate, which usually leads to a decrease in the mean size of the particles.

Surfactants are commonly used in pharmaceutical suspensions in order to lower the interfacial tension between the solid and the solvent facilitating wetting of the solid. They can also be used as colloids to improve the stability of the suspension. Surfactants have been found to promote, to slow down, or to prevent crystal growth in solutions.

2.2.1 The effect of temperature on particle size

Cooling of a solution is one of the most widely used methods for achieving the supersaturation essential for crystallisation. Cooling temperature is known to influence the rate of growth and size of crystals through its effect on supersaturation [Jones (1974), Myerson & Ginde (1993), Mullin (2000), Chernyshev (2009) & Seoudi et al. (2010)]. In general, the crystal size decreases at higher levels of supersaturation due to increased nucleation rates. Therefore, a larger number of small crystals can be achieved with low cooling temperatures. A minor factor influencing the nucleation and crystal growth as the temperature decreases is the resulting increase in the viscosity of the solution, causing diminished molecular movement. This, in turn, slows down both nuclei formation and growth rate on the nuclei formed [Mullin (2000)].

2.2.2 The effect of stirring rate on the particle size

It is known that the stirring rate has a strong influence upon the nucleation rate. While gentle stirring causes nucleation in solutions that are otherwise stable, strong stirring creates an even greater tendency to form nuclei [Mullin & Raven (1961)]. The reduced crystal size observed with increased stirring rates is therefore likely to result from secondary nucleation. Nucleation has been considered as a 2-step process: first, the diffusional transport step, followed by integration of molecules into the crystal lattice [Mullin & Raven (1961), Dogua & Simon (1978)]. Secondary nucleation is critically dependent on stirring rates. It is well known that as stirring rates increase, so does the secondary nucleation [Mullin (2000)]. It is also known that the stirring rate has a strong influence upon the nucleation rate of solutions until a particular stirring rate is reached. After this no increase occurs because solute diffusion is maximised.

2.3 Supercritical fluid processing

Supercritical fluids, the properties of which can be tuned by changing the fluid density between those of liquid and gases, have been adopted or are being explored as: (a) alternative solvents for classical separation processes such as crystallisation, adsorption, fractionation, extraction and chromatography, (b) as reaction media as in polymerisation or depolymerisation, or (c) simply as a reprocessing fluid as in the production of fibers, particles or foams. A wide variety of organic and inorganic materials have been processed in the form of particles, fibers, films and foams, employing supercritical fluids as solvent or antisolvents.

The history of supercritical fluids started when Baron Cagniard de la Tour, a French engineer and physicist discovered the critical point of a substance in his famous cannon barrel experiments in 1822 [Berche et al. (2009)]. He observed the critical temperature by listening to the discontinuities in the sound of a rolling flint ball in sealed cannon filled with fluids at various temperatures. The densities of the liquid and gas phases become equal above this temperature and the distinction between them disappears, resulting in a single supercritical fluid phase. Hanny and Hogarth [Hanny & Hogarth (1879)] are considered as pioneers in laying the fundamental properties of supercritical fluids, based on their basic concept of Rapid Expansion of Supercritical Solutions (RESS). They described that when the solid is precipitated by suddenly reducing the pressure, it is crystalline, and may be brought down as a ‘snow’ in the gas. This concept was further understood and developed after the pioneering works of Krukonis [Krukonis (1984)] and especially the Battelle Institute Research team [Smith et al. (1987)] that described and modelled the flow pattern and nucleation process. Since the mid 1980s, a lot of work on particle production using supercritical fluids, and especially supercritical carbon dioxide ($scCO_2$) has been carried out [Jung & Perrut (2001)].

Jung and Perrut have described in detail about a number of techniques for the production of particles using SCFs. These details can be found in section 2.3.2.

2.3.1 Definition of a supercritical fluid

A supercritical fluid (SCF) can be defined as any substance that is above both of its critical pressure (P_c) and critical temperature (T_c). Some of the common substances and their critical conditions are shown in Table 2.4.

Name	T_c (^oC)	P_c (bar)
Nitrogen	-147.1	33.9
Carbon dioxide	31.0	73.8
Butane	153.0	36.5
Water	374.2	221.9

Table 2.4 Critical values of some common substances [Reid et al. (1987)].

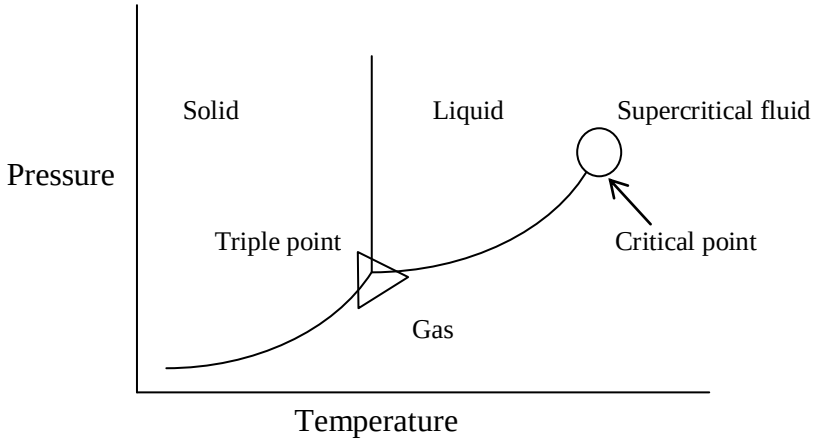

Figure 2.6 Generic phase diagram illustrating critical point and supercritical phase region [York (1999)].

From Figure 2.6, it can be noted that above the critical point condition (denoted by the critical point), the fluid is no longer in a gas or a liquid phase, but midway between these two phases. At this condition, it can diffuse into solids like a gas, and dissolve materials like a liquid. This means that SCFs have higher diffusivities than corresponding liquids and higher densities than the equivalent gases [Tsutsumi et al. (1995)]. In term of its viscosity, it is lower than that of the same liquid but more equivalent to that of the gas phase. Close to the critical point, small changes in pressure or temperature will result in large changes in density, allowing many properties of a supercritical fluid to be "fine –tuned" [Tsutsumi et al. (1995)]. Table 2.5 shows the density, diffusivity and viscosity for a typical gas, liquid and supercritical phases:

Phase	Density (kg/m^3)	Diffusivity (m^2s^{-1})	Viscosity ($Ns\ m^{-2}$)
Gas	6 -20	$(1 – 4) \times 10^{-5}$	$(1 – 3) \times 10^{-5}$
Liquid	600 - 1600	$(2 – 20) \times 10^{-10}$	$(2 – 30) \times 10^{-4}$
Supercritical	200 - 1000	$(2 – 7) \times 10^{-8}$	$(1 – 9) \times 10^{-5}$

Table 2.5 Typical selected properties for materials in gas, liquid and supercritical phases [reproduced from Raynie (1997)].

A SCF makes a good solvent due to its density and diffusivity properties (solvating power is directly linked to density), thus it is the main principle behind the bulk of SCF processing. Once the system is expanded to atmospheric conditions, the SCF is no longer a solvent thus causing the solute to disengage. This leaves the solute 'residue-free' [Weidner et al. (1994)], which is of use for industries with high regulatory control, such as the pharmaceutical industry.

There are many industrial uses for SCFs, such as extraction, chromatography, chemical reactions, micro and nano particle formation, supercritical water oxidation, supercritical water power generation, biodiesel production and for storage of carbon capture. An in depth review on some of these other uses for SCFs can be gained by texts published by McHugh [McHugh & Krukonis (1994)] and Clifford [Clifford (1999)]. One of the main advantages of using SCF to produce nano and micro particles is the reduction in the amount of process steps (mostly being a single step process) as compared to conventional particle production techniques and the use of milder temperature conditions if the SCF is CO_2. Figure 2.7

illustrates the comparison between a crystallisation and milling process to that of a SCF process for a pharmaceutical drug production.

(a) Crystallisation and milling

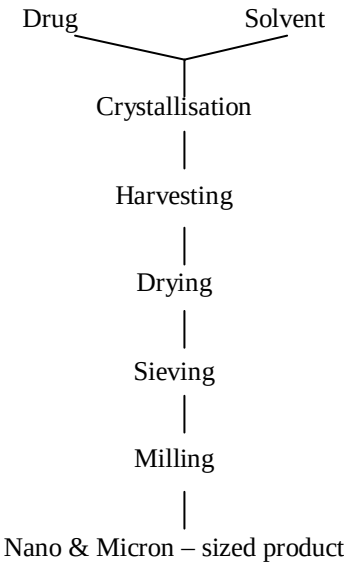

(b) Supercritical fluid processing

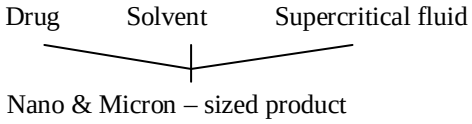

Figure 2.7 Illustration of reduced complexity of supercritical fluid processing for nano and microparticle formation [York (1999)].

2.3.2 Particle production techniques using supercritical carbon dioxide ($scCO_2$)

Jung and Perrut [Jung & Perrut (2001)] have described in detail a number of techniques for the production of particles using SCFs. These techniques include the Rapid Expansion of a Supercritical Solution (RESS), Supercritical Anti-Solvent (SAS), Gas Anti-Solvent (GAS), Solution Enhanced Dispersion of Supercritical fluid (SEDS) and Particles from Gas-Saturated Solutions (PGSS). Fages et al. (2004) have described particle generation for pharmaceutical applications using SCF technology, which include antibiotics, ibuprofen, cyclodextrins, naproxen, poly-lactic acid (PLA) and poly-ethylene-glycol (PEG) polymers. Meanwhile, Reverchon and Adami (2006) have described in detail the production of nanomaterials by SCFs processing. The categories of nanomaterials mentioned were nanofibres, nanowires, nanotubes, nanofilms and nanocomposite materials. Tang et al. (2006 & 2007) have described in detailed on the production of catalysts particles (e.g., titanium dioxide and cerium oxide) using supercritical carbon dioxide ($scCO_2$).

2.3.2.1 Particles prepared by RESS and PGSS

2.3.2.1.1 RESS (Rapid Expansion of a Supercritical Solution)

This technique is the oldest of all the supercritical fluid (SCF) particle production techniques to be reported, with the basic concept of RESS first described by the pioneers Hannay and Hogarth [Hannay & Hogarth (1879)]. Then, in 1984, Krukonis [Krukonis (1984)] demonstrated this technique after years of development. In 1996, Mishima et al. (1996) claimed the formation of polymeric microcapsules by a process called rapid expansion from supercritical solution with a non solvent (n-RESS). A polymer dissolved in the supercritical fluid containing a co-solvent is sprayed at atmospheric pressure. The co-solvent has to be chosen in order to increase the polymer solubility into the supercritical fluid but must be a non solvent of the polymer at atmospheric pressure to avoid particle agglomeration.

Microcapsule formation is claimed by making a suspension of active in the supercritical solution of polymer. In this technique, the SCF is used as a solvent in the crystallisation processes, in fact, with RESS the solute is first dissolved in a SCF, and then the solutions rapidly expanded (decompressed) by passing through a heated nozzle at supersonic velocity. During the rapid expansion of the supercritical solution, the density and solvent power decrease dramatically, leading to a supersaturation of the solution and subsequent precipitation of solute particles. This is different to other particle production techniques where supersaturation is controlled only by temperature and stirring rate or mixing rate. A schematic diagram of RESS equipment is shown in Figure 2.8.

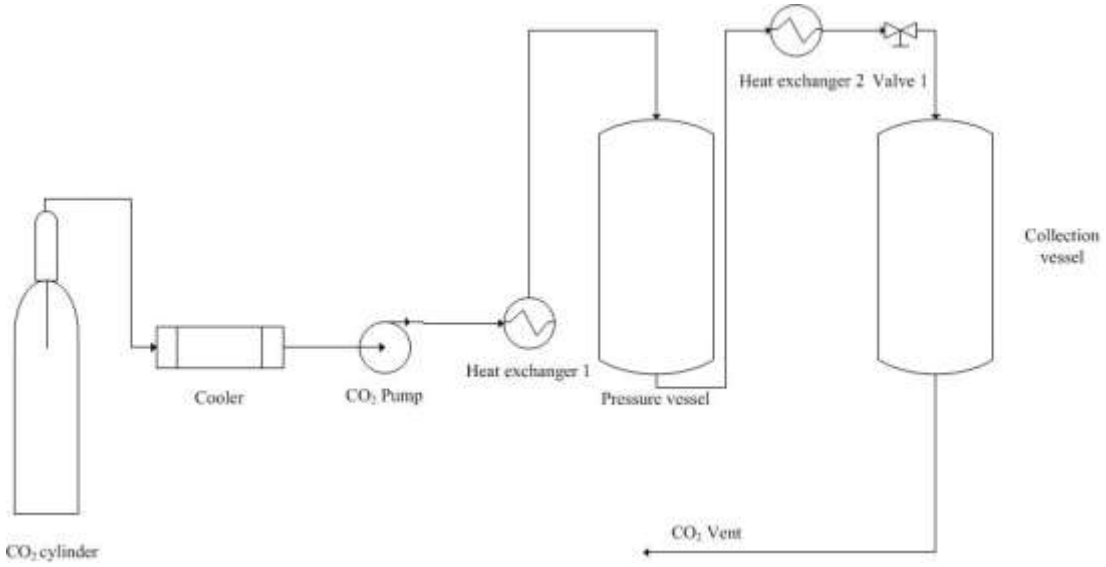

Figure 2.8 Schematic diagram of RESS equipment.

Several groups have studied the RESS process for substances, which have applications in various fields, such as pharmacy, electronic industry, cosmetics and food industry [Knez (2001)]. Recent work on this technique include the formation of retinyl palmitate-loaded poly($_L$-lactide) nanoparticles for multipurpose delivery applications [Sane & Limtrakul (2009)], precipitation of polydisperse poly(lactic acid) for medical and pharmaceutical applications [Imran ul-haq et al. (2010)] and formation of cephalexin particles, a semisynthetic cephalosporin antibiotic intended for oral administration [Hezave & Esmaelzadeh (2010)].

2.3.2.1.2 PGSS (Particles from Gas-Saturated Solutions)

PGSS is a process where a supercritical fluid is dissolved in a melted substrate, or a solution of the substrate in an organic solvent, or a suspension of the substrate in an organic solvent, followed by a rapid expansion of the saturated solution through a nozzle. A schematic diagram of PGSS equipment is shown in Figure 2.9.

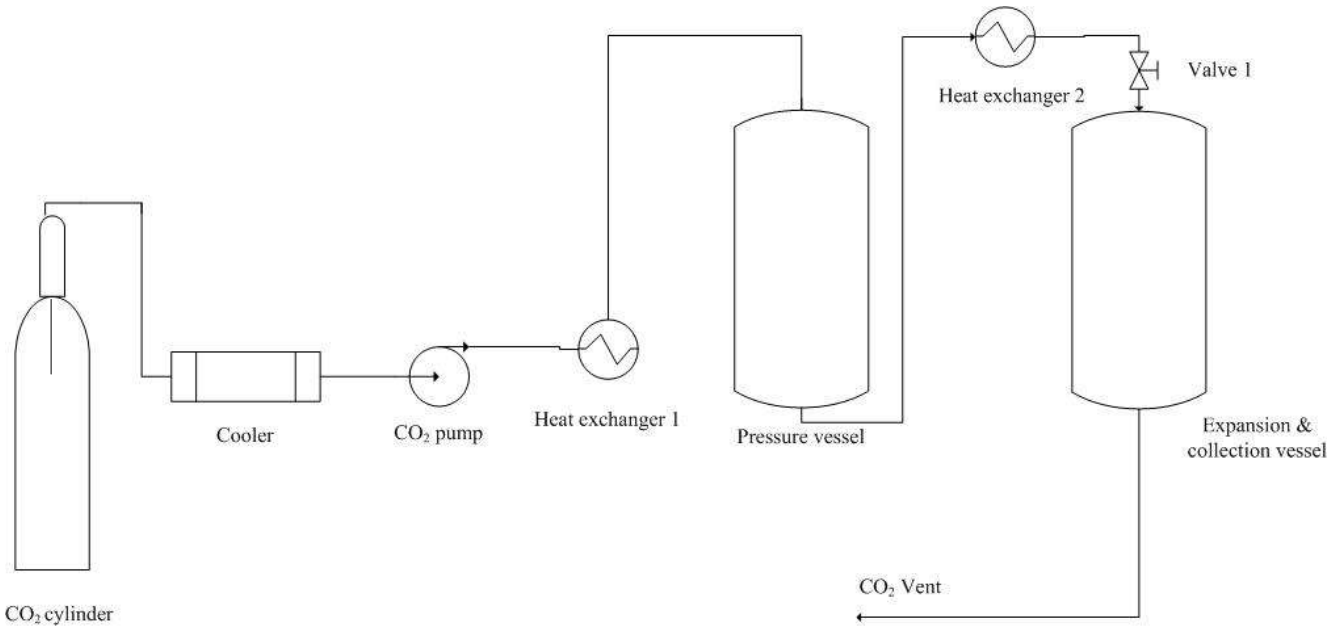

Figure 2.9 Schematic diagram of PGSS equipment.

Supercritical CO_2 is dissolved in an autoclave into a liquid, which can be either a solution of the crystallised compound (sometimes a suspension) or a melted solid. A gas-saturated solution is obtained, which after some time is then expanded through a nozzle in an expansion chamber. Generation of solid particles (or liquid droplets) is induced in expansion chamber which are then collected after completion of the process.

In 1979, Best et al. (1979) described a procedure for preparing very finely divided carotenoids using supercritical gases. Crystalline substrates were dissolved in a mixture of supercritical gas and entrainer. The solution was then dispersed in a colloidal matrix before being decompressed resulting in active precipitation into the matrix. PGSS has been mainly used for polymers [Jung & Perrut (2001)] in which high amounts of CO_2 can be dissolved. In addition, the properties of the polymer, such as its glass transition and melting temperature or density, can be modified. If a third component is previously dissolved or suspended in the polymer, the final depressurisation may lead to polymer microspheres with an embedded substance. Particle sizes of 0.3 to 400 µm can be obtained with the PGSS process, depending on the substrates to be atomised [Jung & Perrut (2001)].

Recent work based on PGSS include the production of polyethylene glycol (PEG) [Martin et al. (2010)], encapsulation of biopesticide *Cydia pomonella* granulovirus [Pemsel et al. (2010)] and formulation of lavadin essential oil with biopolymers [Varona et al. (2010)].

2.3.2.2 Particles prepared by antisolvent techniques, GAS, SAS and SEDS

2.3.2.2.1 GAS (Gas Anti-Solvent)

Francis (1954) did pioneering work on binary and ternary systems involving carbon dioxide which led to the GAS concept as far back as 1954. Generally, in the GAS technique, the target active substance is dissolved in a suitable organic solvent. The vessel is partially filled with the solution then CO_2 is pumped in until the final pressure is reached; CO_2 may also be added once the pressure is reached. The organic solvent is progressively removed by the CO_2, leading to the precipitation of the active. Adding $scCO_2$ as an antisolvent expands the organic solution causing a reduction of the organic solvent power towards the active, which leads to supersaturation of the solution. The active nucleates and particles are formed as the active looses its affinity in the organic solvent. The SCF is preferably introduced through the bottom of the vessel to achieve a better mixing of solvent and antisolvent [Hanna (1995)]. The particles produced from GAS process using CO_2 are relatively free from solvent residue, as they are often cleaned using fresh CO_2. The process allows both the original solvent and the CO_2 to be recycled if required. A schematic diagram of GAS equipment is shown in Figure 2.10.

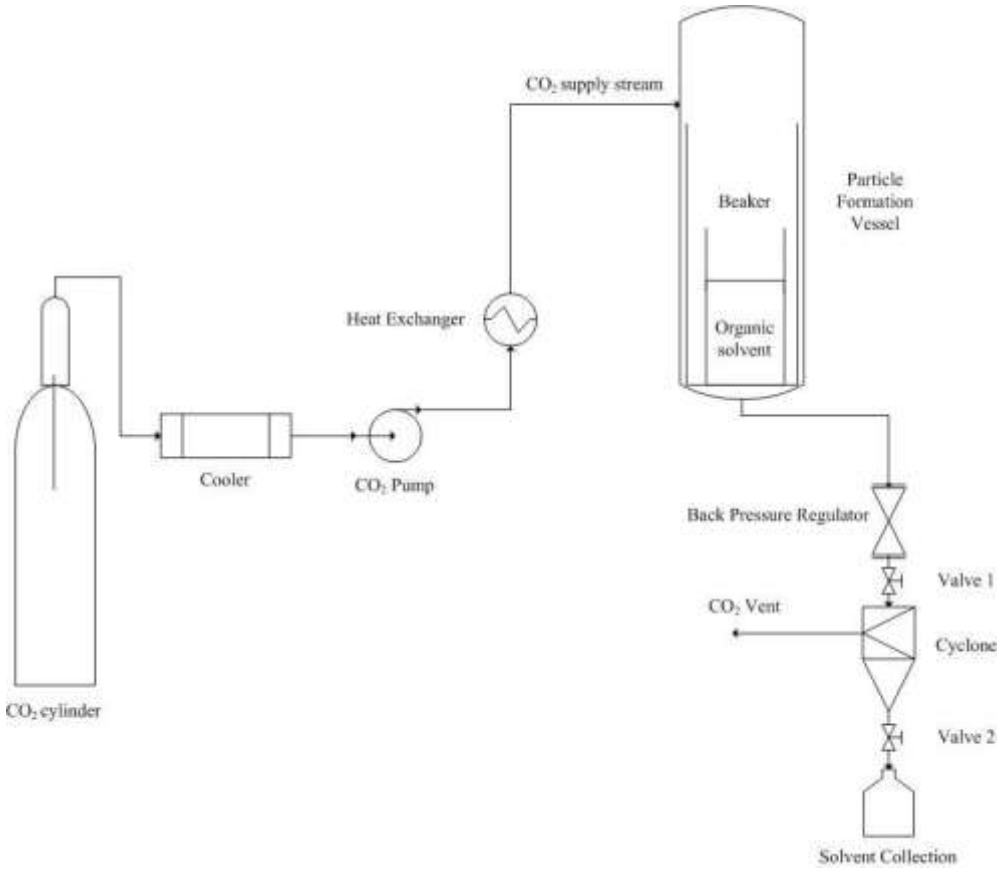

Figure 2.10 Schematic diagram of GAS equipment.

GAS has been used extensively for working with explosive substances, nitroguanidine & cyclotrimethylenetrinitramine (RDX) [Gallagher et al. (1989 & 1992)] as well as pharmaceutical compounds, such as insulin [Thiering (2000)] and even some polymer products [Dillow (1997)]. More recent attempts of GAS include the precipitation of β-carotene nanoparticles for use as natural colorants and antioxidants [Mattea et al. (2009)], the precipitation of an acrylate-methacrylate copolymer for drug delivery systems [Garay et al. (2010)] and the precipitation of γ-Indomethacin (IMC) as non-steroidal anti-inflammatory drug (NSAID) [Varughese et. al. (2010)]. Like RESS, GAS is inherently a batch process as the particles are retained in the pressure vessel during the process. The cost of pressure vessels with large volume limits scale-up.

2.3.2.2.2 SAS (Supercritical Anti-Solvent)

This technique is also known as the aerosol solvent extraction system (ASES) or the precipitation with a compressed antisolvent (PCA) process. A liquid solution contains the solute to be micronized. At the process conditions the supercritical fluid should be completely miscible with the liquid solvent, whereas, the solute should be insoluble in the SCF. Therefore, contacting the liquid solution with SCF either by coaxial nozzles, impinging jet nozzles or triaxial nozzles induces the formation of a solution, producing supersaturation and precipitation of the solute. The formation of this liquid mixture is very fast due to the enhanced mass transfer rates in the jet as well as those that characterise supercritical fluids and, as a result, nanoparticles can be produced. A schematic diagram of SAS equipment is shown in Figure 2.11.

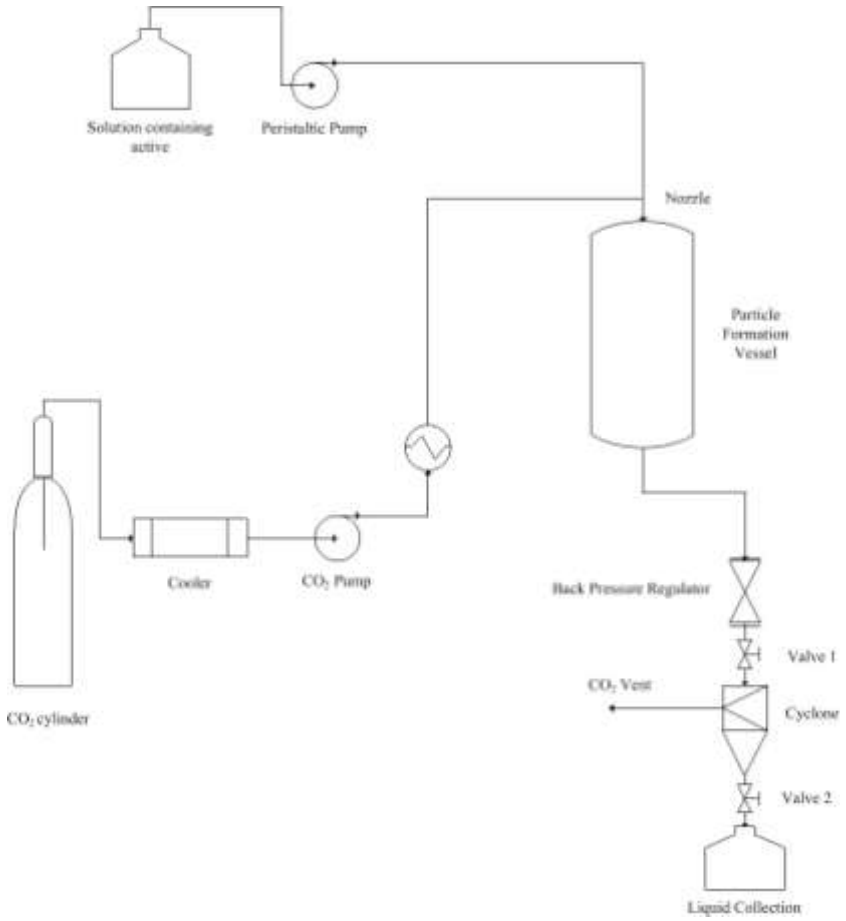

Figure 2.11 Schematic diagram of SAS equipment.

The formation of a single supercritical phase is the key step for the successful production of nanoparticles by this technique. The washing step with pure supercritical antisolvent at the end of the precipitation process is also fundamental to avoid the condensation of the liquid phase that otherwise rains on the precipitate, modifying its characteristics.

In this process, the mass transfer and the nucleation occur at the surface of solution droplets in a continuous flow of anti-solvent. There is a competition between two phenomena that occur simultaneously:

- The anti-solvent effect, *i.e.* the dissolution of the anti-solvent into the solution. The consequence is the swelling of the solution droplets;
- The evaporation of the solvent into the anti-solvent. The consequence is the shrinking of the solution droplets. This leads to supersaturation and nucleation, thus the formation of particles.

Bradford Particle Design patented particle formation of lipophilic substances and low polarity materials with this technique [Hanna et al. (1999)]. Recent application of the SAS technique include the precipitation of amoxicilin, an Active Pharmaceutical Ingredient (API) [Montes et al. (2010)], the precipitation of cellulose acetate filaments as matrix for adsorbent beads and membranes [de Marco & Reverchon (2010)] and the recrystallisation of erlotinib hydrochloride and fulvestrant, two anti-cancer APIs have also been reported [Tien at al. (2010)]. Particle sizes of 0.01 to 500 µm can be obtained with the SAS process, depending on the substrates to be processed [Jung & Perrut (2001)].

2.3.2.2.3 SEDS (Solution Enhanced Dispersion of Supercritical Fluids)

In this technique, the solute solution and the supercritical fluid are introduced simultaneously into the particle formation vessel (where temperature and pressure are controlled) through a co-axial nozzle with a mixing chamber (Figure 2.12). The high velocity of the SCF allows the production of droplets of very small size, while the good mixing of the solvent with the SCF inside the mixing chamber leads to an increase of mass transfer of SCF into the solvent and vice versa. The particle formation is determined by the mass transfer of the SCF into the sprayed droplet and by the rate of solvent transfer into the supercritical phase. In particular, a high mass transfer allows a faster nucleation and a smaller particle size with less agglomeration. Supersaturation takes place inside the mixing chamber as shown in the figure below.

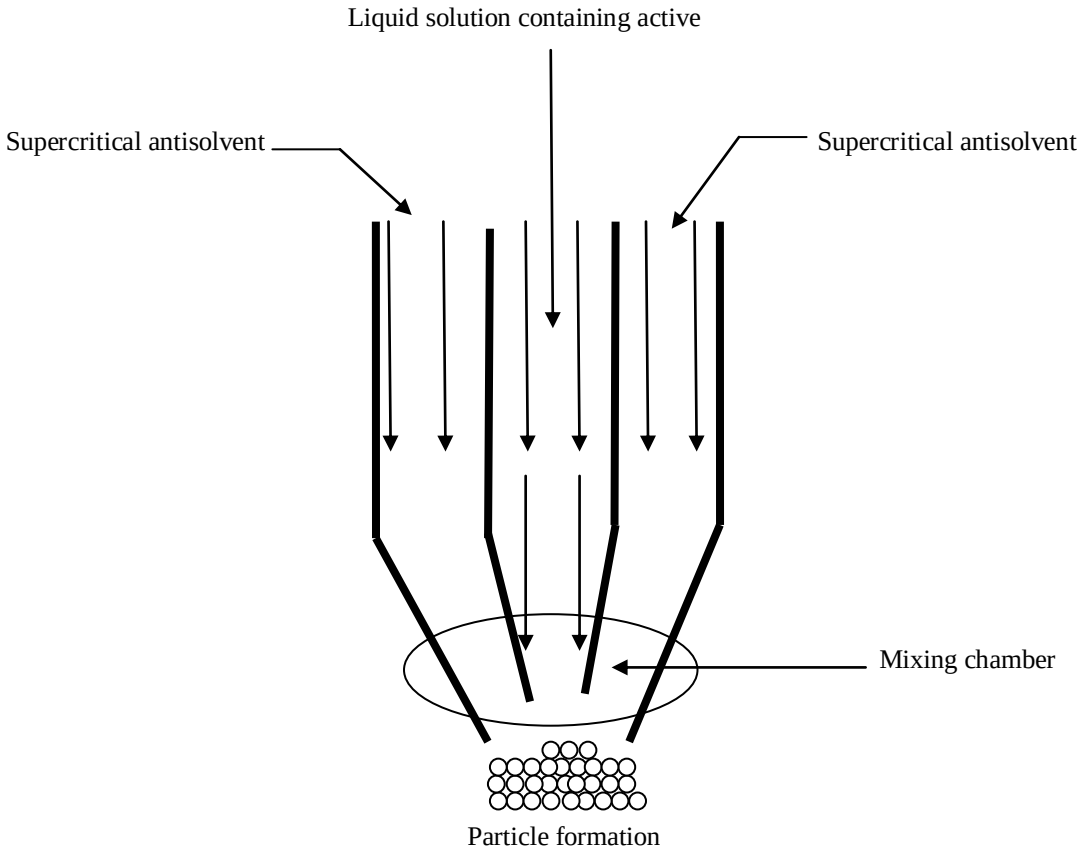

Figure 2.12 A typical SEDS coaxial nozzle diagram.

SEDS has been further developed to process water-soluble compounds (*e.g.* peptides and proteins) by introducing the organic solvent, the SCF, and the aqueous solution as separate streams into a co-axial three-component nozzle [Hanna (1995)]. This arrangement helps to overcome the problems associated with the limited solubility of water in supercritical CO_2.

All these characteristics (efficient mixing of solution and antisolvent & fast supersaturation) make SEDS a highly controlled, reproducible technique compared to other antisolvent-based SCF processes. The SEDS process is suitable for scaling-up and manufacturing according to GMP requirements. A schematic diagram of SEDS equipment is shown in Figure 2.13.

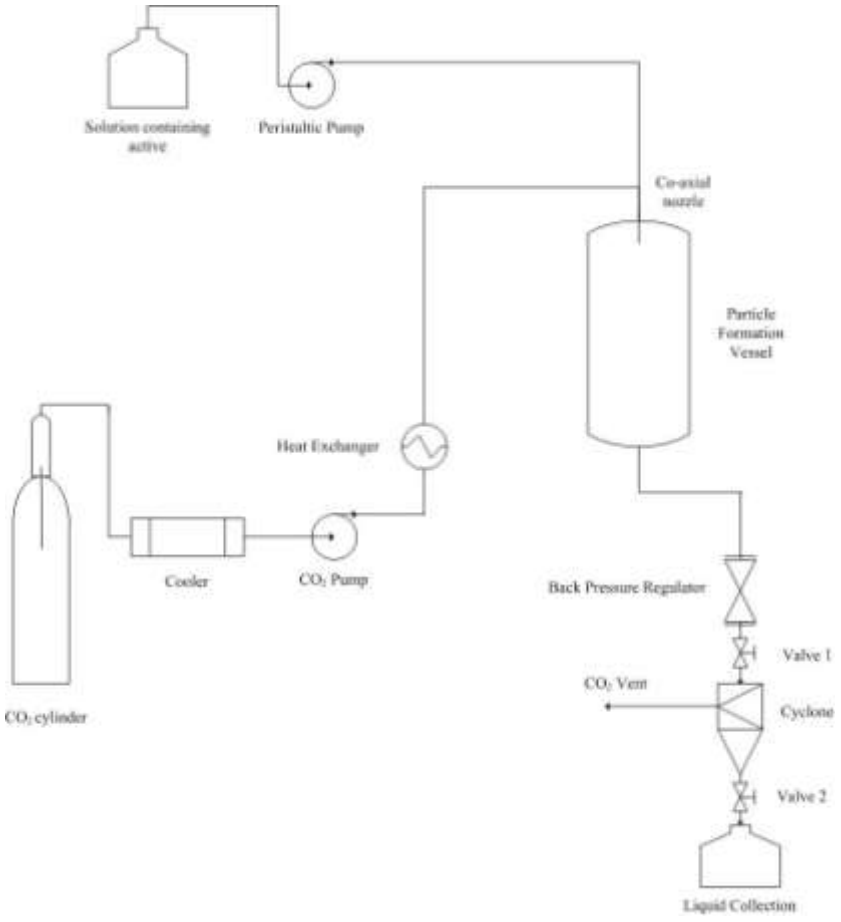

Figure 2.13 Schematic diagram of SEDS equipment.

The chief developers of SEDS^{TM}, Bradford Particle Design, have successfully applied the process to numerous situations, including processing of dyes [Hanna (1994)], polystyrene [Hanna (1998)] and lactose [Hanna (1995)]. Other workers have successfully manufactured proteins of a smaller and more uniform nature than conventional techniques [Sloan et al. (1998)]. The major success of SEDS^{TM} is in the production of intrapulmonary delivery systems [Okamoto & Danjo (2008)], where the particle size needs to be small (<5 μm) but the distribution needs to be very tight.

Recent developments on the SEDS based application include the precipitation of β-carotene microparticles for use in food industry [Franceschi et al. (2009) & Priamo et al. (2010)] and the precipitation of Astaxanthin to be used as a natural colorants [Hong et al. (2009)]. As a summary, Knez reviewed the CO_2 assisted micronisation techniques as follows in Table 2.6 [Knez (2000)]:

	RESS	**GAS**	**PGSS**	**SEDS**
Establishing equilibrium	Discontinuous	Semi discontinuous	Continuous	Continous
Gas demand	High	Medium	Low	Low
Pressure	High	Low to medium	Low to medium	Low to medium
Solvent	None	Yes	None	None
Volume of equipment	Large*	Medium to large	Small	Small
Gas/solid separation	Can be difficult	Easy	Easy	Easy
Gas/solvent separation	N/A	Difficult	N/A	N/A

* can be small if in-line mixer is used.

Table 2.6 Comparison of various SCF particle processes [Knez (2000)].

SCF assisted methods for manufacture and processing of materials have been successfully demonstrated up to pilot scale and have great potential for the production of particulate materials of high purity, small size and narrow size distribution for use in industries as diverse as pharmaceuticals to industrial plastics manufacture.

The GAS and SEDS techniques are used in this work as suitable basis for the production of CaP particles for drug delivery.

2.4 Layout of this Thesis

Chapter 3 of this thesis discusses the production of hydroxyapatite (HAp) particles by a wet chemistry method (sol-gel) and evaluating the effects of reaction temperature, stirring rate and addition of Mg^{2+} on the particle size. Chapter 4 discusses the recrystallisation of HAp using two supercritical antisolvent techniques, which are Gas Anti-Solvent (GAS) and Solution Enhanced Dispersion of Supercritical Fluids (SEDS). The effects of process temperature, pressure and supercritical fluid to solvent molar ratio on particle size are evaluated. Particles produced in both chapters were characterised for their physical properties by X-ray diffraction, XRD (phase analysis), Fourier Transform InfraRed spectroscopy, FTIR (functional groups analysis), Dynamic Light Scattering, DLS (particle size analysis), Scanning electron microscopy, SEM (morphology & particle size analysis) and Transmission electron microscopy, TEM (morphology & particle size analysis).

In Chapter 5, an investigation of calcium phosphate (CaP) precipitation processes, both by wet chemistry and SEDS technique is discussed. Here, a systematic study on the formation of CaP based on calcium to phosphorus ratio is reported. Chapter 6 discusses the co-precipitation of the calcium phosphate based particles with plasmid DNA (pDNA). The binding efficiencies between HAp and the CaP materials produced by the wet chemistry method, GAS and SEDS techniques are evaluated. Also in this chapter, a transfection study using CaP-pDNA complexes is discussed. This was undertaken in order to evaluate the potential of these complexes as a gene vector in gene therapy.

2.5 References:

Becker, P. 1989. Phosphates and phosphoric acid: raw materials technology and economics of the wet process. 2nd Ed. In Fertilizer Science and Technology series. Marcel Decker: New York, USA, 760.

Berche, B. Henkel, M. Kenna, R. 2009. Critical Phenomena: 150 Years since Cagniard de la Tour. Journal of Physical Studies 13: 3201.

Bermudez, O. Boltong, M. G. Driessens, F. C. M. Planell, J. A. 1994. Optimization of a calcium orthophosphate cement formulation occurring in the combination of monocalcium phosphate monohydrate with calcium oxide. J. Mater. Sci. Mater. Med. 5: 67 – 71.

Bermudez, O. Boltong, M. G. Driessens, F. C. M. Planell, J. A. 1994. Development of some calcium phosphate cements from combinations of α-TCP, MCPM and CaO. J. Mater. Sci. Mater. Med. 160-163.

Bermudez, O. Boltong, G. M. Driessens, F. C. M. Planell, J. A. 1994. Development of an octacalcium phosphate cement. J. Mater. Sci. Mater. Med. 5: 144 – 146.

Bertoni, E. Bigi, A. Cojazzi, G. Gandolfi, M. Panzavolta, S. Roveri, N. 1998. Nanocrystals of magnesium and fluoride substitute hydroxyapatite. J. Inorg. Biochem. 72: 29 – 35.

Best, W. Muller, F. J. Schmieder, K. Frank, R. Paust, J. 1979. German Patent 2 943 267 (BASF AG).

Bose, J. Saha, S. K. 2003. Synthesis and characterization of hydroxyapatite. Nanopowders by emulsion technique. Chem. Mater. 15: 4464 – 4469.

Boistelle, R. Astier, J. P. 1988. Crystallisation mechanisms in solution. J. Cryst. Growth. 90: 14 – 30.

Briak-Ben, E. Abdeslam, H. Ginebra, M. P. Vert, M. Boudeville, P. 2008. Wet or dry mechanochemical content on DCPD-CaO reaction kinetics. Acta Biomaterials 4: 378 – 386.

Brown, W. E. Chow, L. C. 1986. Cements Research Progress. American Ceramic Society, 352 – 379.

Budavari, S. O'Neil, M. J. Smith, A. Heckelman, P. E. Kinneary, J. F. 1996. The Merck Index: an encyclopedia of chemicals, drugs and biological. Chapman & Hall, USA, 12th Ed. 1741.

Burton, W. K. Cabrera, N. Frank, F. C. 1951. Phi. Trans. Roy. Soc. Lond. 234A: 299 – 358.

Chai, C. S. Ben-Nissan, B. 1999. Bioactive nanocrystalline sol-gel hydroxyapatite coatings. J. Mater. Sci. Mater. Med. 10: 465 – 469.

Chernyshev, A. P. 2009. Effect of nanoparticle size on the onset tempearature of surface melting. Materials Letters. 63:17, 1525 – 1527.

Crall, J. J. Bjerga, J. M. 1987. Effects of DCPD/APF application and prolonged exposure to fluoride on caries-like lesion formation *in vitro*. J. Oral Pathol. Med. 16: 488 – 491.

De Marco, I. Reverchon, E. 2010. Nanostructured cellulose acetate filaments produced by supercritical antisolvent precipitation. J. of Supercritical Fluids. 55:3, 1095 – 1103.

Dogua J. Simon, B. Crystallisation of sodium perborate from aqueous solution. J. Cryst. Growth. 44: 265 – 279.

Dorozhkin, S. V. 2007. Calcium orthophosphates. J. Mater. Sc. 42: 1061-1095.

Dorozhkin, S. V. 2009. Nanodimensional and Nanocrystalline Apatites and Other Calcium Orthophosphates in Biomedical Engineering, Biology and Medicine. J. Mater. Sc. 2: 1975 – 2045.

Elliott, J.C. 1994. Studies in Inorganic Chemistry, Vol. 18. Structure and Chemistry of the apatite and other calcium orthophosphates. Elsevier Science, Amsterdam.

Feng, W. Mu-Sen, L. Yu-peng, L. Yong-xin, Q. 2005. A simple sol-gel technique for preparing hydroxyapatite nanopowders. Materials Letters 59: 916 – 919.

Ferraz, M. P. Monteiro, F. J. Manuel, C. M. 2004. Hydroxyapatite nanoparticles. A review of preparation methodologies. J. Appl. Biomater. & Biomech. 2: 74 – 80.

Florence, A. T. Attwood, D. 1998. Physicochemical Principles of Pharmacy. Basingstoke, UK. Macmillan Press Ltd.

Franceschi, E. De Cesaro, A. M. Ferreira, S. R. S. Oliviera, J. V. 2009. Precipitation of β-carotene microparticles from SEDS technique using supercritical CO_2. Journal of Food Engineering 95: 656 – 663.

Francis, A. W. 1954. Jornal of Physics. 58, 1099.

Gallagher, P. M. Coffey, M. P. Krukonis, V. J. Klasutis, N. 1989. In Supercritical Fluid science and Technology. Johnston, K. P. Penniger, J. M. L. Eds. ACS Symposium Series 406, American Chemical Society, Washington DC.

Gallagher, P. M. Coffey, M. P. Krukonis, V. J. 1992. Gas Anti-Solvent Recrystallisation of a Difficult to Comminute Explosive. J. of Supercritical Fluids 5: 130 – 142.

Garay, I. Pocheville, A. Madariaga, L. 2010. Polymeric microparticles prepared by supercritical antisolvent precipitation. Powder Technology 197: 211 – 217.

Garside, J. Davey, R. J. 2000. From molecules to crystallizers – An introduction to Crystallization, Oxford University Press, New York.

Ginebra, M. P. Fernandez, E. De Maeyer, E. A. P. Veerbeck, R. M. H. Boltong, M. G. Ginebra, F. Driessens, F. C. M. Planell, J. A. 1997. Setting reaction and hardening of an apatitic calcium phosphate cement. J. Dent. Res. 76: 905 – 912.

Hanna, M. York, P. Hanna, M. H. 1999. Patent WO 9959710.

Hannay, J. B. Hogarth, J. 1879. On the solubility of solids in gases. Proc. Roy. Sec. (London), 29: 324.

Hench, L. L. Wilson, J. 1993. An introduction to bioceramics. World Scientific Singapore. pp 1 – 24.

Hezave, A. Z. Esmaelzadeh, F. 2010. Investigation of rapid expansion of supercritical solution parameters effects on size and morphology of cephalexin particles. J. of Aerosol Science 41: 1090 – 1112.

Hofmann, M. P. 2003. Physikalische Charakterisierung von Calciumphosphat-Pulvern zur Einstellung von Prozessparametern für dieHerstellung von Knochenzement. PhD thesis, University of Wüerzburg.

Hong, H. L. Suo, Q. L. Han, L. M. Li, C. P. 2009. Study on Precipitation of Astaxanthin in Supercritical Fluid. Powder Technology 191 (3): 294 – 298.

Imran ul-haq, M. Acosta-Ramirez, A. Mehrkhodavandi, P. Signorell, R. 2010. Influence of polydispersity of poly(lactic acid) on particle formation by rapid expansion of supercritical CO_2 solutions. J. of Supercritical Fluids 51: 376 – 383.

Kano, J. Zhang, Q. Saito, F. Baron, M. Nzihou, A. 2006. Synthesis of hydroxyapatite with the mechanochemical treatment products of PVC and CaO. Process Safety and Environmental Protection 84: 309 – 312.

Knez, Z. 2000. Micronisation of pharmaceuticals using supercritical fluids. Antibes (France) vol. 1, ISASF International Society for Advancement of Supercritical Fluids, Nancy, France, 21 -26.

Knez, W. E. 2001. Precipitation of solids with dense gases. In: Bertucco, A. Vetter, G. editors. High pressure process technology: fundamentals and applications. Amsterdam, London: Elsevier, pp. 587 – 611.

Layrolle, P. Ito, A. Tateishi, T. 1998. Sol-gel synthesis of amorphous calcium phosphate and sintering into microporous hydroxyapatite bioceramics. J. Amer. Ceram. Soc. 81: 1421 – 1428.

Lee, D. D. Tofighi, A. Aiolova, M. Chakravarthy, P. Catalano, A. Majahad, A. Knaack, D. 1999. A biomimetic bone substitute and drug delivery vehicle, Clin. Orthop. Suppl. 367.

LeGeros, R. Z. 1985. Preparation of octacalcium phosphate (OCP): a direct fast method. Calcif. Tissue Int. 37: 194 – 197.

LeGeros, R. Z. 1991. Calcium Phosphates in Oral Biology and Medicine. Karger, Basel, H. M. Myers, ed. 110 – 118.

LeGeros, R. Z. 1991. Calcium Phosphates in Oral Biology and Medicine. Karger, Basel, H. M. Myers, ed. 154 – 157.

LeGeros, R. Z. LeGeros, J. P. 1993. Dense hydroxyapatite. In An introduction to bioceramics, Hench, L. L. Wilson, J. Eds. World Scientrific: London, UK. pp 134 – 180.

Lehr, J. R. Brown, E. H. Frazier, A. W. Smith, J. P. Thrasher, R. D. 1963. Crystallographic properties of fertilizer compounds. Chemical Engineering Bulletin No 6. Muscle Shoals, Tennessee Valley Authority.

Lim, G. K. Wang, J. Ng, S. C. Gan, L. M. 1999. Formation of nanocrystalline hydroxyapatite in nonionic surfactant emulsion. Langmuir 15: 7472 – 7477.

Lim, G. K. Wang, J. Ng, S. C. Gan, L. M. 1999. Nanosized hydroxyapatite powders from microemulsions and emulsions stabilised by a biodegradable surfactant. J. Mater. Chem. 9: 1635.

Lu, T. Blackburn, S. Dickinson, C. Rosseinsky, M. J. Hutchings, G. Axon, S. Leeke, G. A. 2009. Production of titania nanoparticles by a green process route. Powder Technology 188:3 264 – 271.

Lynn, A. K. Bonfield, W. 2005. A novel method for the simultaneous, titrant-free control of pH and calcium phosphate mass yield. Acc. Chem. Res. 38: 202 – 207.

Mackellar, A. J. Buckton, G. Newton, J. M. Chowdhry, B. Z. Orr, C. A. 1994. The controlled crystallization of a model power. I. The effects of altering the stirring rate and the supersaturation profile and the incorporation of a surfactant (Poloxamer 188). Int. J. Pharm. 112: 56 – 78.

Matsuya, Y. Matsuya, S. Antonacci, J. M. Takagi, S. Chow, L.C. Akamine, A. 1999. Effect of powder grinding on hysdroxyapatite formation in a polymeric calcium phosphate cement prepared from tetracalcium phosphate and poly(methyl vinyl ether maleic-acid). Biomaterials 20: 691 – 697.

Mattea, F. Martin, A. Matias-gago, A. Cocero, M. J. 2009. Supercritical antisolvent precipitation from an emulsion: β-carotene nanoparticle formation. J. of Supercritical Fluids 51: 238 – 247.

Martin, A. Pham, H. M. Kilzer, A. Kareth, S. Weidner, E. 2010. Micronization of polyethylene glycol by PGSS (Particles from Gas Saturated Solutions)-drying of aqueous solutions. Chemical Engineering and Processing 49: 1259 – 1266.

Mejdoubi, E. Lacout, J. L. Heughebaert, J. C. Michaud, P. 1994. Optimization of a hydraulic calcium phosphate cement. Adv. Mater. Res. 163 – 171.

Miao, X. Hu, Y. Liu, J. Wong, A. P. 2004. Porous calcium phosphate ceramics prepared by coating polyurethane foams with calcium phosphate cements. Materials Letters 58: 397 – 402
Mishima, K. Yamaguchi, S. Umemoto, H. 1996. Patent JP 8-104830.

Montes, A. Tenorio, A. Gordillo, M. D. Pereyra, C. Martinez dela Ossa, E. J. 2010. Screening design of experiment applied to supercritical antisolvent precipitation of amoxicillin: Exploring new miscible conditions. J. of Supercritical Fluids 51: 399 – 403.

Mullin, J. W. 1964. Crystallisation, Butterworth & Co., London.

Mullin, J. W. 2000. Crystallisation. Oxford, UK: Butterworth-Heinemann.

Myerson, A. S. Ginde, R. 1993. Crystals, crystal growth and nucleation. Handbook of Industrial Crystallisation. St. Louis, Butterworth-Heinemann, 33 – 63.

Okamoto, H. Danjo, K. 2008. Application of supercritical fluid to preparation of powders of high-molecular weight drugs for inhalation. Advanced Drug Delivery Reviews 60: 433 – 446.

Oliveira, C. Rocha, F. Ferreira, A. 2007 Dicalcium phosphate dehydrate precipitation, Characterisation and crystal growth, Trans IChemE, Part A, 1655 – 1661.

Paital, S. R. Danotre, N. B. 2008. Review of laser based biomimetic and bioactive Ca-P coatings. Mater. Sci. and Tech. 24: 1144 – 1161.

Pemsel, M. Schwab, S. Scheurer, A. Freitag, D. Schatz, R. Schlucker, E. 2010. Advanced PGSS process for the encapsulation of the biopesticide Cydia pomonella granulovirus. J. of Supercritical Fluids 53: 174 – 178.

Priamo, W. L. De Cezaro, A. M. Ferreira, S. R. S. Oliviera, J. V. 2010. Precipitation and encapsulation of β-carotene in PHBV using carbon dioxide as anti-solvent. J. of Supercritical Fluids 54: 103 – 109.

Rodriquez-Clemente, R. Lopez-Macipe, A. Gomez-Morales, J. Torrent-Burgues, J. Castano, V. M. 1998. Hydroxyapatite precipitation: A case of nucleation-aggregation-agglomeration-growth mechanishm. J. Eur. Ceram. Soc. 18: 1351 – 1356.

Rhee, S-H. 2002. Synthesis of hydroxyapatite via mechanochemical treatment. Biomaterials 23: 1147 – 1152.

Sane, A. Limtrakul, J. 2009. Formation of retinyl palmitate-loaded poly(L-lactide) nanoparticles using rapid expansion of supercritical solutions into liquid solvents (RESOLV). J. of Supercritical Fluids 51: 230 – 237.

Sangwal, K. 1998. Prog. Cryst. Growth and Charact. 36: 163 - 167.

Seoudi, R. Shabaka, A. Eisha, W. H. Anies, B. Farage, N. M. 2010. Effect of the prepared temperature on the size of CdS and ZnS nanoparticle. Physica B: Condensed Matter, 405:3, 919 – 924.

Shelton, R. M. Liu, Y. Cooper, P. R. Gbureck, U. German, M. J. Barralet, J. E. 2006. Bone marrow cell gene expression and tissue construct assembly using octacalcium phosphate microscaffolds. Biomaterials 27: 2874 – 2881.

Shi, D. 2004. Biomaterials and tissue engineering. Springer, New York. pp 1 – 26.

Shirkhanzadeh, M. 1998. Direct formation of nanophase hydroxyapatite on cathodically polarized electrode. J. Mater. Sci. Mater. Med. 9: 67 – 72.

Skrtic, D. Antonucci, J. M. Eanes, E. D. Eidelman, N. 2004. Dental composites based on hybrid and surface-modified amorphous calcium phosphates. Biomaterials 25: 1141 – 1150.

Sonoda, K. Furuzono, T. Walsh, D. Sato, K. Tanaka, J. 2002. Influence of emulsion on crystal growth of hydroxyapatite solid state ionics 151: 321 – 327.

Suchanek, W. L. Byrappa, K. Shuk, P. Riman, R. E. Janas, V. F. TenHuisen, K. S. 2004. Mechanochemical-hydrothermal synthesis of calcium phosphate powders with coupled magnesium and carbonate substitution. J. Solid State Chem. 177: 793 – 799.

Sun, L. Berndt, C. C. Kucuk, A. Gross, K. A. 2001. Material fundamentals and clinical performance of plasma sprayed hydroxyapatite coatings – Review Appl. Biomat. 58 (5): 570 – 592.

St. Pierre, P. D. S. 1955. The preparation of dicalcium phosphate dehydrate and calcium pyrophosphate. J. Am. Chem. Soc. 77: 2197-2198.

Takagi, S. Chow, L. C. Ishikawa, K. 1998. Formation of hydroxyapatite in new calcium phosphate cements. Biomaterials 19: 1593 – 1599.

Tang, Z-R. Bartley, J. K. Taylor, S. H. Hutchings, G. J. 2006. Preparation of TiO_2 using supercritical CO_2 antisolvent precipitation (SAS): A support for high activity gold catalysts. Studies in Surface Science and Catalysts 162, 219 – 226.

Tang, Z-R. Edwards, J. K. Bartley, J. K. Taylor, S. H. Carley, A. F. Herzing, A. A. Kiely, C. J. Hutchings, G. J. 2007. Nanocrystalline cerium oxide produced by supercritical antisolvent precipitation as support for high-activity gold catalysts. Journal of catalysts 29:2 208 – 219.

Tas, A. C. 2000. Combustion synthesis of calcium phosphate bioceramic powders. J. Eur. Ceram. Soc. 20: 2389.

Tas, A. C. 2000. Synthesis of biomimetic Ca-hydroxyapatite powders at 37 ^{o}C in synthetic body fluids. Biomaterials 21: 1429 – 1438.

Tien, Y. C. Su, C. S. Lien, L. H. Chen, Y. P. 2010. Recrystallisation of erlontinib hydrochloride and fulvestrant using supercritical antisolvent process. J. of Supercritical Fluids 55 (1): 292 – 299.

Tung, M. Eichmiller, F. Gibson, H. Ly, A. Skrtic, D. Schumacher G. 1997. Dentin Desensitization by *in situ* Formulation of Calcium Phosphate. J. Dent. Res. 76: 2985.

Varona, S. Kareth, S. Martin, A. Cocero, M. J. 2010 Formulation of lavadin essential oil with biopolymers by PGSS for application as biocide in ecological agriculture. J. of Supercritical Fluids 54: 369 – 377.

Varughese, P. Li, J. Wang, W. Winstead, D. 2010. Supercritical antisolvent processing of γ-Indomethacin: Effects of solvent, concentration, pressure and temperature on SAS processed Indomethacin. Powder Technology 201: 64 – 69.

Weng, W. J. Baptista, J. L. 1997. A new synthesis of hydroxyapatite. J. Eur. Ceram. Soc. 17: 1151-1156.

Yang, Y-Z. Kim, K-H. Ong, J. L. 2005. A review on calcium phosphate coatings produced using a sputtering process as an alternative to plasma spraying. Biomaterials 26: 327 – 337.

Yin, X. Stott, M. J. Rubio, A. α- and β-tricalcium phosphate: a density functional study. Phys. Rev. B 68: 205.

Yoshmura, M. Suda, H. Okmoto, K. Loku, K. 1994. Hydrothermal synthesis of biocompatible whiskers. J. Mater. Sci. 29: 3399.

Zhang, H. Wang, Y. Yan, Y. Li, S. 2003. Precipitation of biocomp[atible hydroxyapatite whiskers from moderately acid solution. Ceramics International 29: 413 – 418.

Zipp, G. L. Rodríguez-Hornedo N. 1993. The mechanism of phenytoin crystal growth. Int. J. Pharm. 98: 189 – 201.

Zou, C. Weng, W. Deng, X. Cheng, K. Liu, X. Du, P. Shen, G. Han, G. 2005. Preparation andcharacterization of porous β-tricalcium phosphate/collagen composites with an integrated structure. Biomaterials 26: 5276 – 5284.

3.0 Hydroxyapatite (HAp) prepared by Sol-gel method

3.1 Introduction

Hydroxyapatite ($Ca_{10}(PO_4)_6(OH)_2$) nanoparticles have a range of applications in a number of fields, such as drug delivery [Feng et al. (2010)], gene therapy [Ichiro et al. (2004)], bone cements [Ni et al. (2006)], dental applications [Balamurugan et al. (2008)], chromatography [Deppert & Lukacin (1999)] and waste water remediation [Molle et al. (2005)]. Depending on the application, there is often a need for the nanoparticles to be in a particular size range. There are various techniques reported in the literature for the production of nanosized hydroxyapaptite (HAp) particles, but none report the effects of processing parameters on particle size and morphology. These techniques include mechano-chemical synthesis [Kano et al. (2006)], combustion preparation [Tas (2000)], and various wet chemistry techniques, such as direct precipitation from aqueous solutions [Rodriquez-Clemente (1998)], sol-gel procedures [Weng & Baptista (1997)], hydrothermal preparation [Yoshmura et al. (1994)] and emulsion synthesis routes [Lim et al. (1999)]. The sol-gel technique has advantages over other techniques as it does not require pH control, high temperature and long hydrolysis times, which contribute to it being one of the most commonly used processing methods for nanomaterials [Feng et al. (2005)]. In the sol-gel method there has been little attempt to investigate the effect of processing conditions on HAp particle size. The only processing variable reported is the effect of calcination temperature on particle size [Feng et al. (2005), Fathi et al. (2007 & 2008)].

Mg^{2+} intercalation into the hydroxyapatite structure has been reported to influence HAp particle size [Chowdhury et al. (2004)], and consequently, this effect was also investigated at different magnesium concentrations and agitation rates. In this chapter, hydroxyapatite nanoparticles were prepared by the sol-gel technique as reported by Feng et al. (2005) and Fathi et al. (2008). A systematic study on the effects of processing temperature, agitator selection and agitation rate on particle size and morphology was undertaken for HAp and intercalated HAp-Mg particles. In all tests, particles were sized by the following techniques: dynamic light scattering (DLS), SEM, TEM and by Scherrer's formula (using X-ray diffraction data).

The work in this chapter formed part of a paper submitted to the Journal of Powder Technology (see Appendix for Chapter 3, Appendix 3 A).

3.2 Experimental

3.2.1 Materials and methods

Calcium nitrate tetrahydrate ($Ca(NO_3)_2.4H_2O$) [CAS No: 13477-34-4], phosphorus pentoxide (P_2O_5) [1314-56-3], calcium chloride [10043-52-4], magnesium chloride [7786-30-3], sodium chloride [7647-14-5], potassium chloride [7447-40-7], sodium phosphate ($Na_2HPO_4.2H_2O$) [10028-24-7], sodium pyrophosphate ($Na_4P_2O_7.10H_2O$) [13472-36-1], absolute ethanol [64-17-5] and HEPES buffered solution [7365-45-9**,** which contains 140 mM NaCl, 5 mM KCl, 25 mM HEPES pH 7.05 containing 75 mM $Na_2HPO_4.2H_2O$] were obtained from Sigma-Aldrich UK and were used without further purification.

3.2.1.1 Preparation of Hydroxyapatite particles

Stoichiometric amounts of calcium nitrate tetrahydrate and phosphorus pentoxide were dissolved in two separate ethanol solutions at room temperature. The concentrations of these precursors were fixed at 100 mM $Ca(NO_3)_2.4H_2O$ and 30 mM P_2O_5, which when mixed to give a Ca salt/P salt molar ratio of 10:3; the ratio observed in stoichiometric hydroxyapatite [Fathi et al. (2008)]. HAp particle synthesis was carried out by adding the precursors (100 ml) at a fixed flowrate of 20 ml/min into a 500 ml beaker and agitating for 30 minutes [Fathi et al. (2008)]. The agitation rates were varied from 200 rpm, 400 rpm, 600 rpm, 800 rpm, 1000 rpm, 1200 rpm, 1400 rpm, 1600 rpm, 1800 rpm, 2000 rpm and 2200 rpm, using an overhead stirrer (Heildolph Co., Type RZR1) fitted with a Ruston turbine impeller. Higher agitation rates of 3000 rpm, 4000 rpm, 5000 rpm, 6000 rpm and 7000 rpm were also investigated using a mechanical blade-type homogeniser (Verso Laboratory Mixer Emulsifier, Silverson Machines Ltd.). The experiments were carried out at 20 ^oC and 40 ^oC. Higher temperatures could not be used due to solvent evaporation. After agitation at the desired temperature the beaker and contents were transferred to a magnetic stirrer plate and the agitation rate was fixed at 200 rpm at 20 ^oC. The solution slowly transforms into a gel under continuous stirring at the respective temperatures after 24 hours. The as-formed gel was aged for a further 24 hours at room temperature and then dried for 24 hours in an air oven at 80 ^oC. The dried gel was then sintered at a temperature of 600 ^oC with a heating rate of 5 °C/min in a muffle furnace (Carbolite Co.) and was placed in air for cooling to ambient temperature. Finally, the sintered product was ground using an agate mortar and pestle for 20 minutes.

3.2.1.2 Preparation of Hydroxyapatite particles with Mg^{2+} (HAp-Mg)

The method described is similar to that used for the preparation of hydroxyapatite particles with some modifications. Particles were prepared by adding 50 ml 125 mM calcium chloride ethanolic solution at 20 ml/min to an agitated solution of 50 ml magnesium chloride ethanolic solution and 100 ml HEPES buffer at 20 ^{o}C. The mixture was agitated at either 200 rpm, 1200 rpm, 2200 rpm, 3000 rpm or 7000 rpm for 30 minutes. The concentration of magnesium chloride in the ethanol solution was varied from 0 mM, 20 mM, 40 mM, 60 mM, 80 mM, 100 mM, 120 mM and 140 mM. The mixture was then agitated at 200 rpm, 20 ^{o}C for 24 hours, aged for a further 24 hours and air dried for another 24 hours. The product was sintered at 600 ^{o}C and ground into powder form (as described for the hydroxyapatite particles in section 3.2.1.1).

3.3 Particle characterisation techniques

3.3.1 Fourier Transform Infrared Spectroscopy (FTIR)

FTIR was conducted using a Nicolet 380 instrument (Thermo Electron Corporation). 3 mg of particles was placed onto an ATR sample holder and pressed down to ensure contact. All of the spectra were collected in the 400 to 4000 cm^{-1} wavenumber range region with 2 cm^{-1} resolution and 64 scans.

3.3.2 X-ray Diffraction (XRD)

The phase analysis was undertaken using a Bruker D8 Advance Diffractometer with a monochromatic Cu Kα source operated at 40 kV and 30 mA. The analysis was recorded over the 2θ range of 20 to 80^{o} at a scan rate of 0.02^{o}/min. The peak broadening of XRD reflection was used to estimate the crystallite size in a direction perpendicular to the crystallographic plane based on Scherrer's formula as follows [Jenkins & Synder (1996)]:

$$X_S = \frac{0.9\lambda}{FWHM\cos\theta} \qquad \textbf{Equation 3.1}$$

where X_s is the crystallite size (nm), λ is the wavelength of x-ray beam (λ = 0.15406 nm for Cu Kα radiation), FWHM is the full width at half maximum for the diffraction peak under consideration (rad), and θ is the diffraction angle (^{o}). The diffraction peak at 26 ^{o} [Fathi et al. (2008)] was chosen for calculation of the crystallite size since it was sharper and isolated from the others.

The fraction of the crystalline phase (X_c) in the hydroxyapatite powders can be evaluated by [Landi et al. (2000)]:

$$X_c = 1 - \frac{V_{112/300}}{I_{300}} \qquad \textbf{Equation 3.2}$$

where I_{300} is the intensity of (300) diffraction peak and $V_{112/300}$ is the intensity of the hollow between (112) and (300) diffraction peaks of hydroxyapatite, which completely disappears in non-crystal samples.

3.3.3 Scanning Electron Microscopy (SEM)

SEM was performed using a Philips XL30 FEG SEM instrument operating at 20 kV on gold coated powder samples. The particles were gold coated using a SC500 Sputter (Emscope) for 3 minutes to give a thickness of approximately 10 nm.

3.3.4 Transmission Electron Microscope (TEM)

TEM was undertaken using a Philips Tecnai F20 TEM. A small amount of particles were dispersed in ethanol before one drop was place on a carbon film and analysed by TEM. The morphology and mean diameter of the particles were obtained from the SEM and TEM images. The number of particles counted was in agreement with the criteria used to constitute the minimal set to be analysed to get basic information on size and shape of powders [Pons et al. (2002)]: a minimum of 500 particles were counted.

3.3.5 Dynamic Light Scattering (DLS)

DLS particle size measurements for both HAp and intercalated HAp-Mg particles were carried out using a High Performance Particle Sizer (Malvern Instruments) to obtain mean intensity particle sizes and polydispersity indices. One mg of particles was transferred into a 250 ml glass bottle, which contained 100 ml of distilled water (solubility of HAp in water is 6 mg/L [Epple & Sokolova (2008)]) and sodium pyrophosphate as a surfactant (10 ml). Before the DLS measurements were carried out, the solution was sonicated for one hour in order to disperse the particles within the solution. Then, 2 ml of the sonicated solution was transferred into a plastic disposable cuvette and placed inside the sample holder. The DLS measurements were repeated three times for each sample and three samples were analysed.

3.4 Results and discussion

Several authors have reported the influence of sintering duration and sintering temperature on HAp particle size [Feng et al. (2005), Fathi et al. (2007 & 2008)], however, the work in this chapter is the first to study the effect of agitation rate, agitator selection and process temperature on HAp particle size and morphology. These parameters are important as HAp nanoparticles have uses in a number of fields where the required particle size distribution and morphology can be application specific.

3.4.1 Fourier Transform Infrared Spectroscopy (FTIR)

Phosphate and hydroxide absorption peaks for hydroxyapatite were seen in the FTIR spectra. FTIR data for some HAp samples prepared at various agitation rates at 20 ^{o}C and 40 ^{o}C are shown in Figures 3.1 and 3.2, respectively.

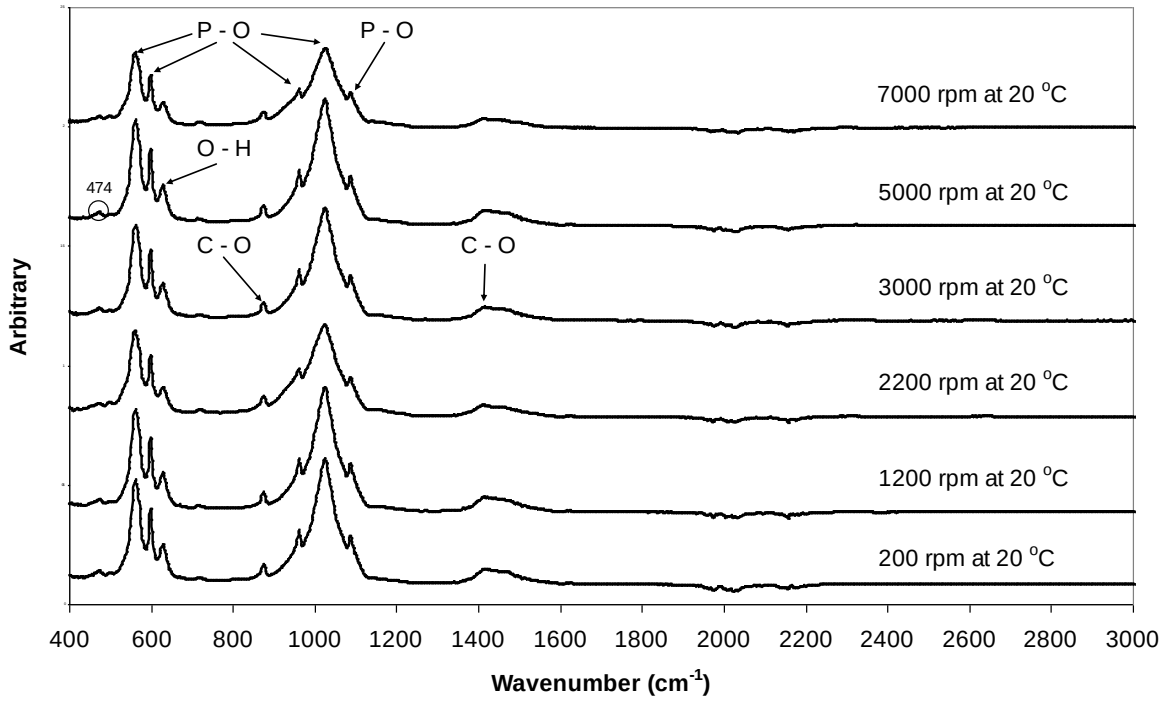

Figure 3.1 FTIR spectra for some of HAp samples produced at 20 ^{o}C.

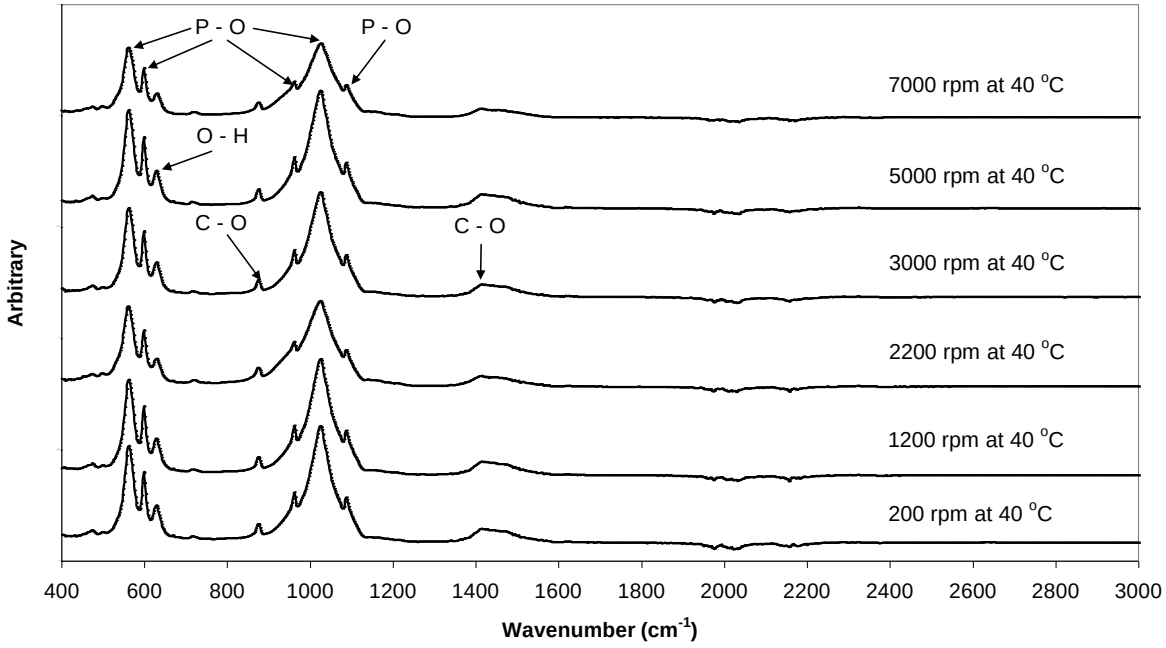

Figure 3.2 FTIR spectra for some of HAp samples produced at 40 °C.

The formation of hydroxyapatite was denoted by the broad phosphate band centered from about 1000 to 1100 cm^{-1} [Varma & Babu (2005)] with bands at 960 to 965 cm^{-1} and 565 to 601 cm^{-1}, which corresponded to the PO_4^{3-} ion [Kawata et al. (2004), Miyaji et al. (2005)]. Major peaks for the phosphate group were between 1100 cm^{-1} to 960 cm^{-1} and 601 cm^{-1} to 567 cm^{-1}.

The bands assigned to the stretching modes of hydroxyl groups in hydroxyapatite were seen at 1800 cm^{-1}, 632 cm^{-1} and 474 cm^{-1} [Varma & Babu (2005), Kawata et al. (2004)]. The stretching modes of the carbonyl from the carbonate groups have been reported to be at 1550 cm^{-1}, 1457 cm^{-1} and 880 cm^{-1} for type A substitution, and 1462 cm^{-1}, 1418 cm^{-1} and 876 cm^{-1} for type B substitution [Krajewski et al. (2005)]. The hydroxyapatite formed in this study was type B substitution, whereby carbonate ions substituted some of the phosphate ions in the

apatitic structure. The source of carbonate would have originated from CO_2 in the atmosphere. The presence of type B carbonate in the apatite lattice has been shown to cause an increase in solubility both *in vitro* and *in vivo* tests [Krajewski et al. (2005)]. The FTIR spectra obtained for all of the HAp samples showed that they are all the same, whereby processing conditions does not effect on particle composition.

FTIR analysis of HAp-Mg intercalated particles showed the presence of hydroxyapatite with the occurrence of phosphate (PO_4^{3-}) and hydroxide peaks. Note, there are no FT-IR bands which correspond to Mg vibrational and stretching modes in the wavenumber range. When the concentration of $MgCl_2$ was increased from 20 to 140 mM, there was a decrease in the intensity of the O-H vibrational modes at 630, 2000 and 3570 cm^{-1} and also a broadening of the PO_4^{3-} bands with respect to the HAp sample without the addition of $MgCl_2$ [Fadeev et al. (2003), Suchanek et al. (2004)]. These observations are typical for synthesised Mg-substituted hydroxyapatites and can be explained by the increased lattice disorder due to HPO_4^{2-} and PO_4^{3-} substitutions, the latter usually increased with the Mg^{2+} content [Suchanek et al. (2004), Bigi et al. (1993), Kannan et al. (2005)]. FT-IR data for some HAp-Mg samples prepared at 60 and 140 mM are shown in Figures 3.3 and 3.4, respectively. Figure 3.3 exhibits a peak at 600 cm^{-1} which is not seen on Figure 3.4 and corresponds to the PO_4^{3-} (this peak was also observed for the 20 mM and 40 mM $MgCl_2$ concentrations). The 140 mM $MgCl_2$ concentration does not show this peak because the produced partcles is in the OCP phase.

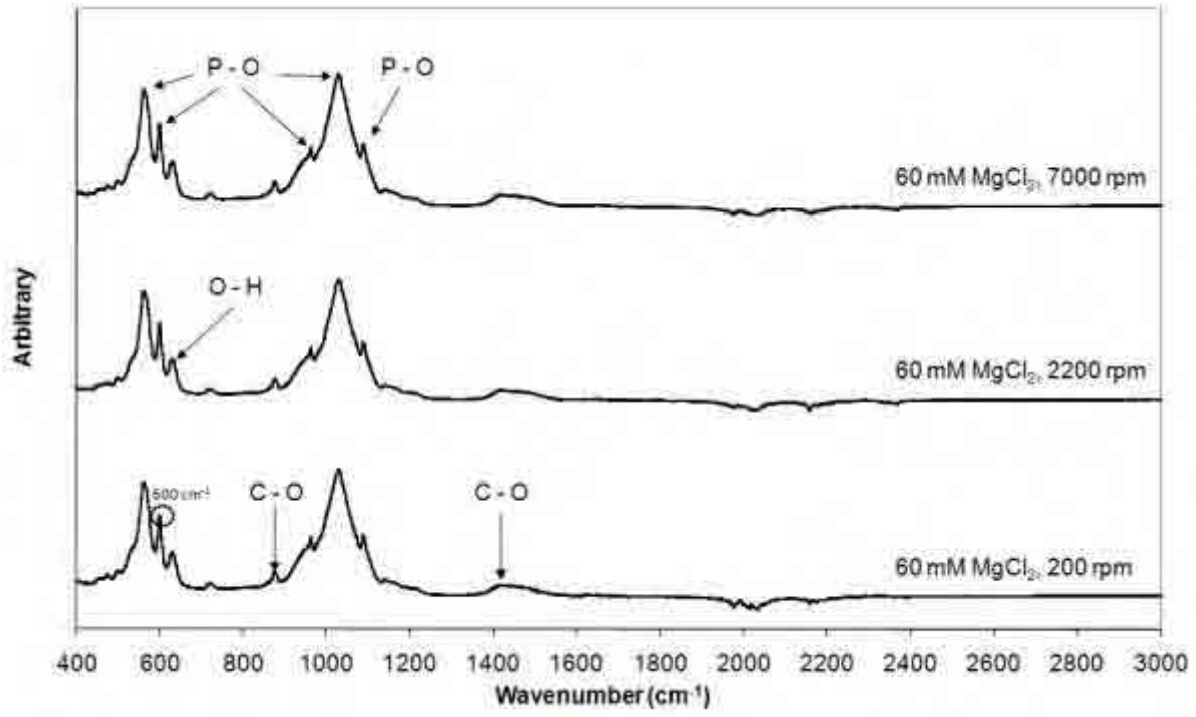

Figure 3.3 FTIR spectra for 60 mM $MgCl_2$ at 200, 2200 and 7000 rpm.

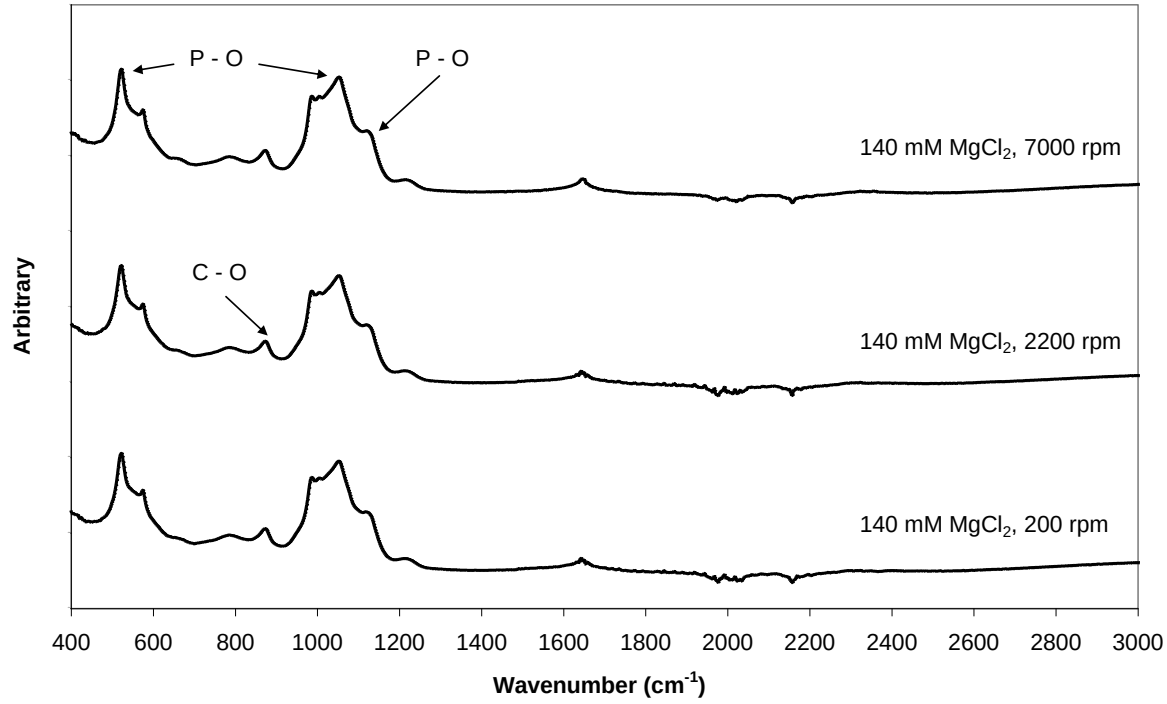

Figure 3.4 FTIR spectra for 140 mM $MgCl_2$ at 200, 2200 and 7000 rpm.

3.4.2 X-ray Diffraction (XRD)

3.4.2.1 Hydroxyapatite - sintered

The formation of hydroxyapatite was indicated by the characteristic peak occurring at 2θ = 31.8^{o} which appeared on all of the HAp samples [Shimbayashi et al. (2000)] and was verified by the pattern for HAp from the JCPDS catalogue. The narrow peaks in the XRD spectra indicate a high degree of crystallinity in the hydroxyapatite particles (an average of 63 % calculated by equation 2). After sintering at 600 ^{o}C, no other phase besides hydroxyapatite was identified. The XRD patterns obtained for all of the HAp samples showed that they are all the same, whereby processing conditions does not effect on the resultant phase. XRD data for some HAp samples prepared at various agitation rates at 20 ^{o}C and 40 ^{o}C are shown in Figures 3.5 and 3.6, respectively.

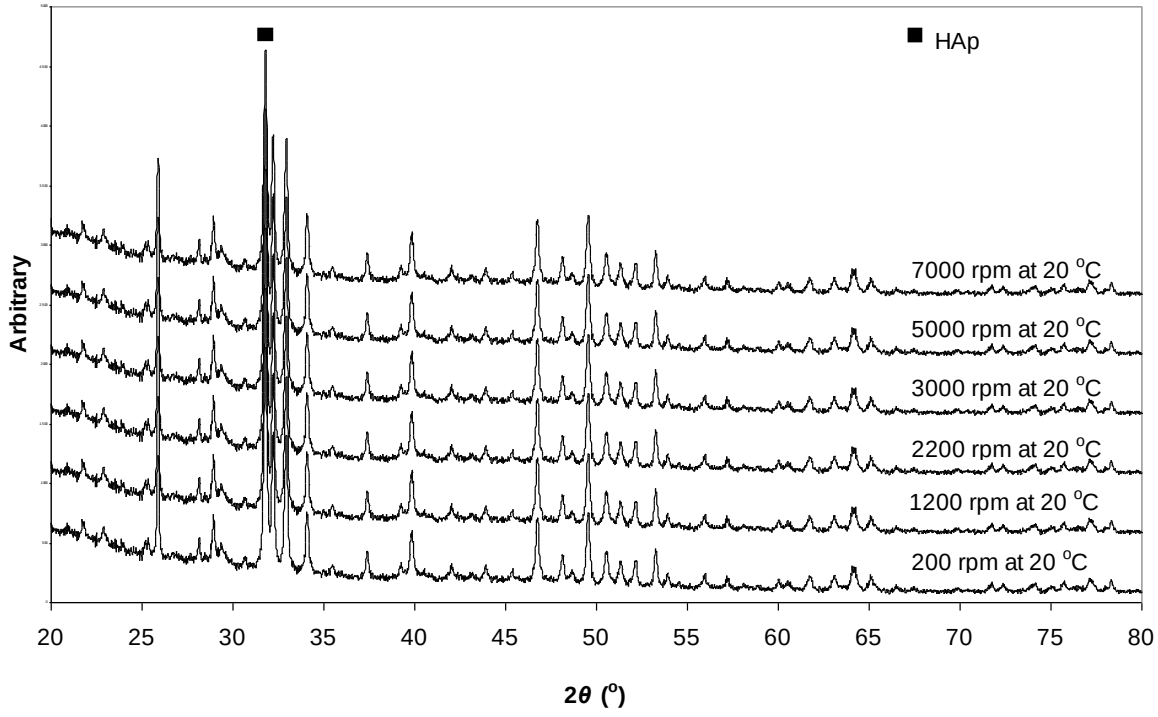

Figure 3.5 XRD patterns for some of HAp samples produced at 20 ^{o}C.

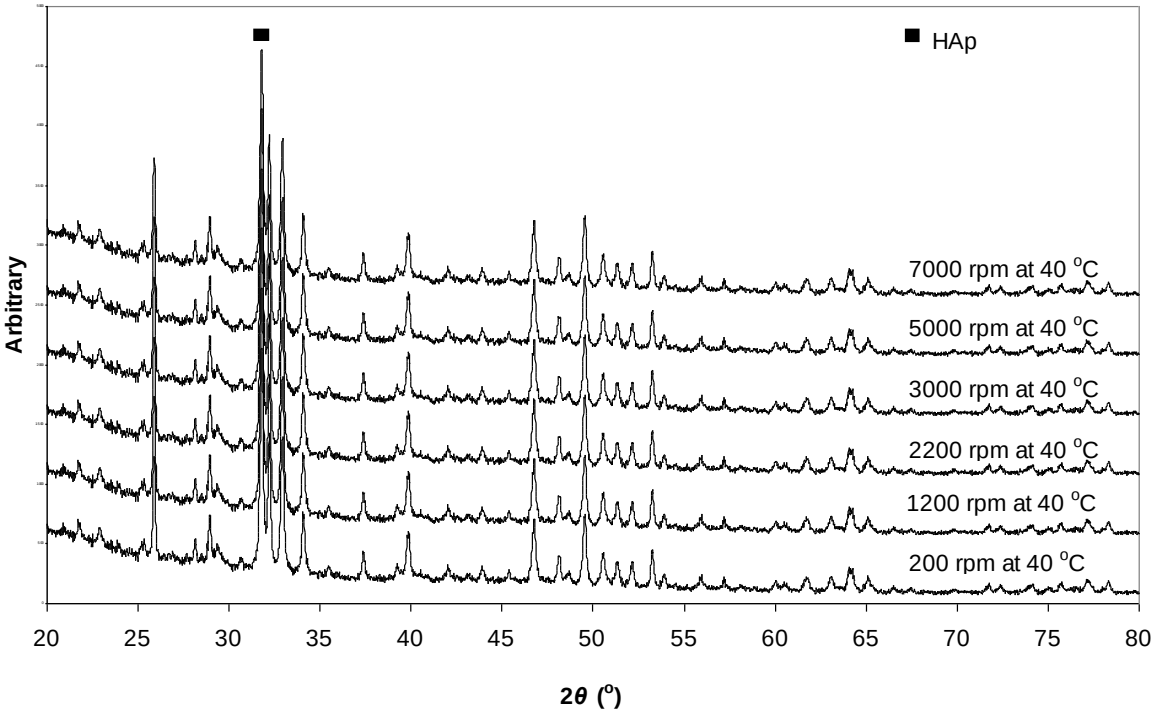

Figure 3.6 XRD patterns for some of HAp samples produced at 40 °C.

3.4.2.2 Mg intercalated calcium phosphate - sintered

XRD analysis of HAp-Mg intercalated particles did not show any detectable evidence of Mg for the 20 to 40 mM concentrations. It has been reported that the addition of $MgCl_2$ at these concentrations will not change significantly the Ca/P ratio of the hydroxyapatite composition; the Ca:P ratio is equal to 1.64 for 20 mM and 1.57 for 40 mM [Chowdhury et al. (2004)]. Only when 60 mM $MgCl_2$ was added the Ca/P ratio changed to 1.29 and showed the characteristic peak for octacalcium phosphate (OCP) [Ca_{4-x}-$Mg_x(PO_4)_3$] at 21°. At 140 mM $MgCl_2$ addition hydroxyapatite is transformed to OCP as evidenced by the intensity of the 21° peak, with a Ca/P ratio of 1.17. XRD data of some of the HAp-Mg samples are shown in Figure 3.7.

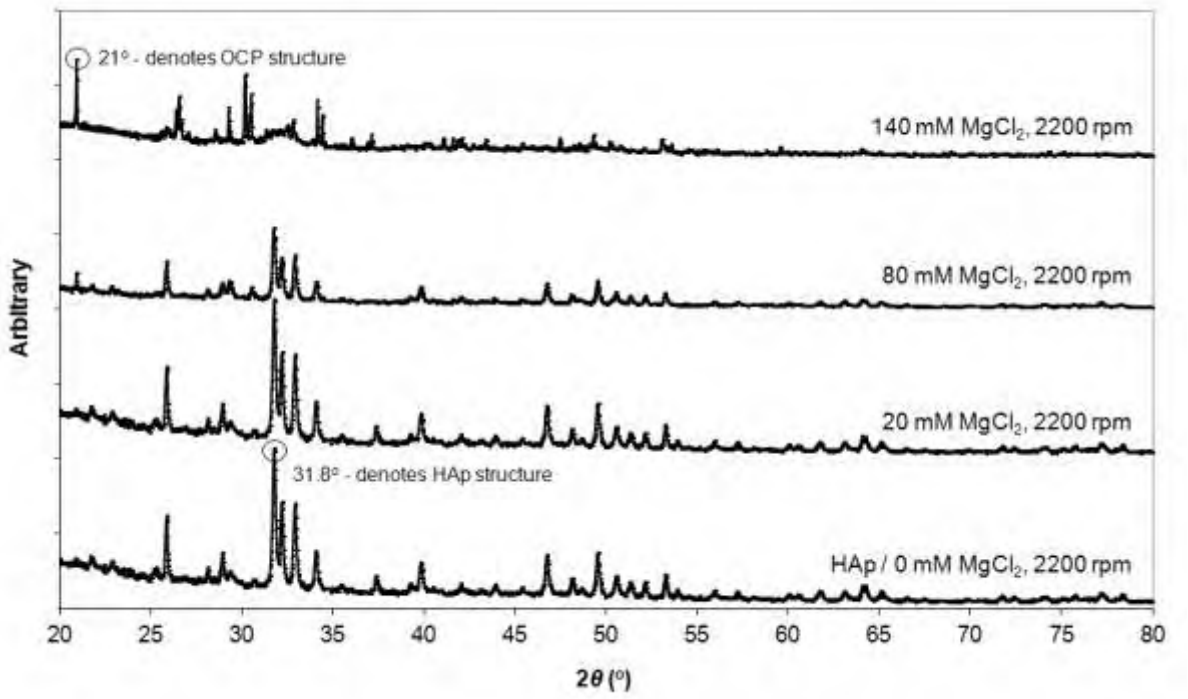

Figure 3.7 XRD patterns of hydroxyapatite samples prepared with 0 mM, 20 mM, 80 mM and 140 mM MgCl2 at 2200 rpm and 20 ^{o}C.

3.4.2.3 Hydroxyapatite- pre-sintered

XRD analysis of pre-sintered HAp particles shows that the Ca/P formed was calcium nitrate before being reverted to hydroxyapatite upon sintering. XRD data of a pre-sintered HAp sample are shown in Figure 3.8.

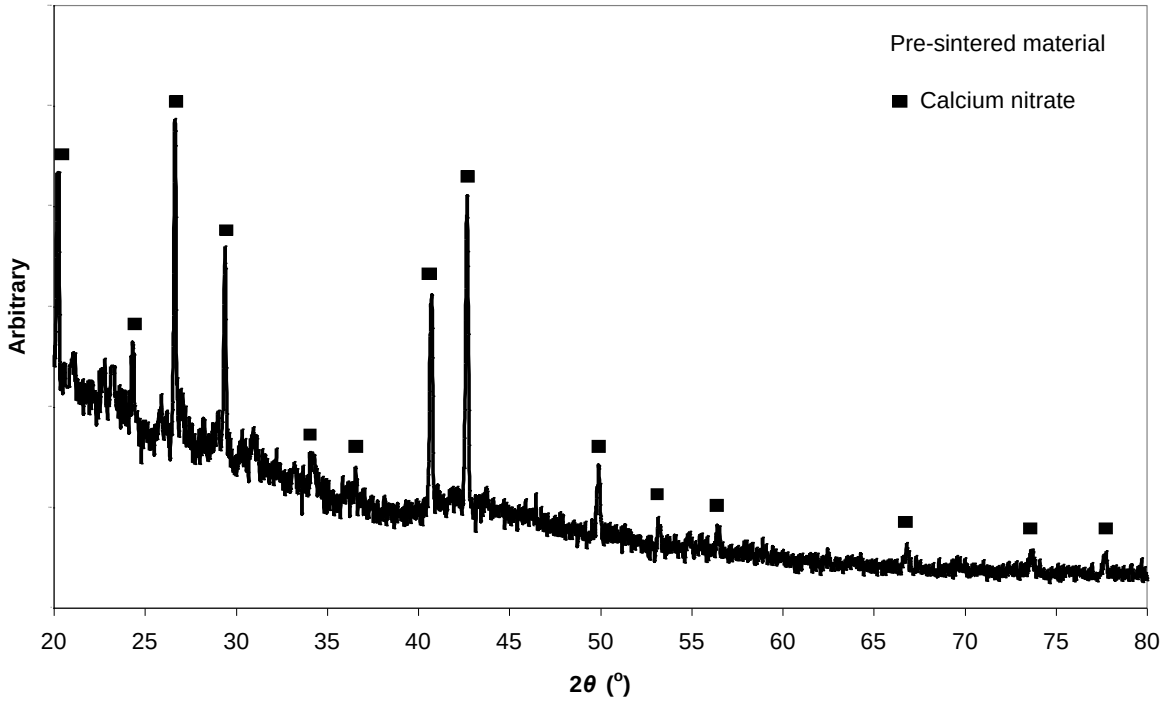

Figure 3.8 XRD spectra of a pre-sintered HAp sample produced at 1200 rpm and 20 ^{o}C.

3.4.3 Scanning Electron Microscopy (SEM)

Prior to sintering HAp shows a plate-like morphology approximately 50 x 20 µm as seen in Figure 3.9. Fathi *et al.* [Fathi et al. (2008)] reported 200 µm agglomerated particles sizes before sintering, but the lack of process agitation rate details makes it difficult to make a comparison. Meanwhile, prior to sintering HAp-Mg shows a flower-like morphology as seen in Figure 3.10.

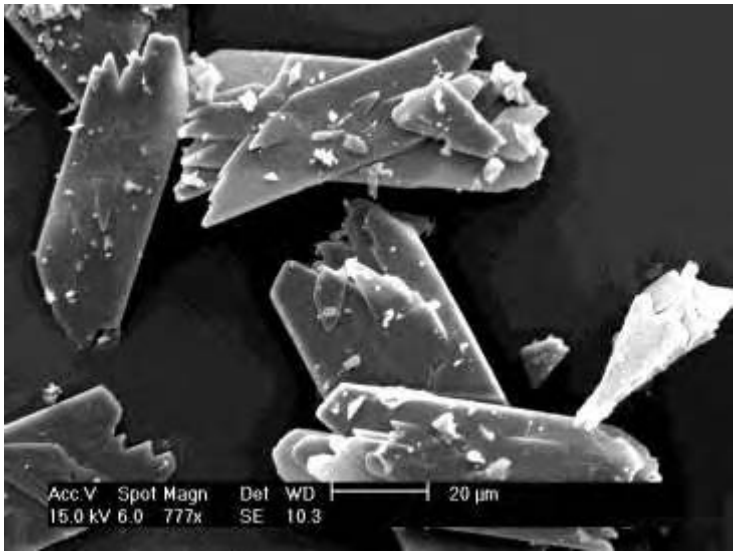

Figure 3.9 SEM of pre-sintered HAp particles produced at 2200 rpm and 20 ^{o}C.

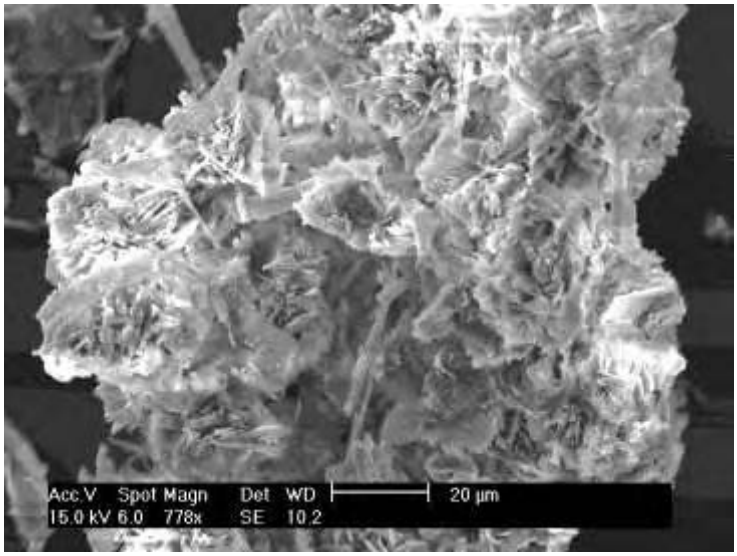

Figure 3.10 SEM of pre-sintered intercalated HAp-Mg particles produced using 140 mM $MgCl_2$. The crystallinity decreased slightly from 63% without $MgCl_2$ to 58% (as calculated from Equation 3.2) when 140 mM was added.

Typical SEMs of post-sintered HAp nanoparticles are shown in Figure 3.11. It can be seen that the fully processed particles form agglomerates of approximately <1 to 5 µm with no obvious difference in morphologies.

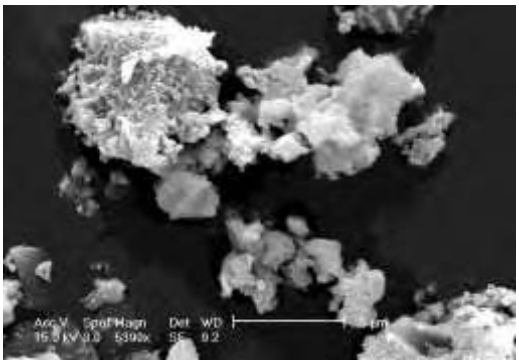

(a) 200 rpm 20 ^{o}C

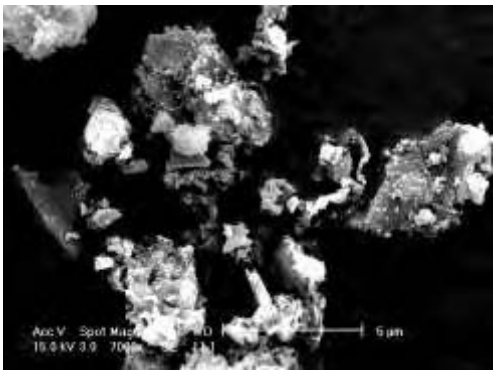

(b) 200 rpm 40 ^{o}C

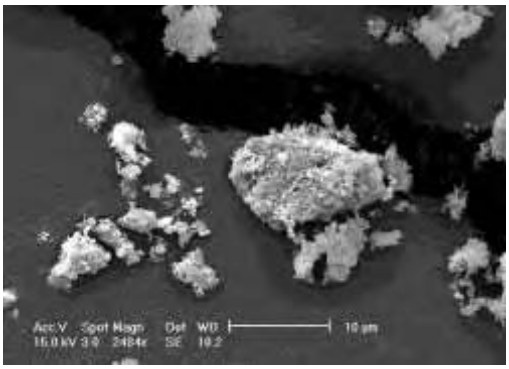

(c) 1200 rpm 20 ^{o}C

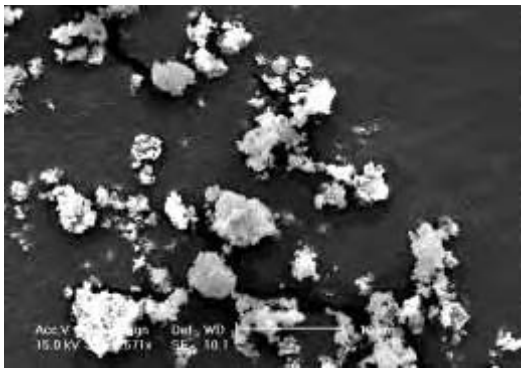

(d) 1200 rpm 20 ^{o}C

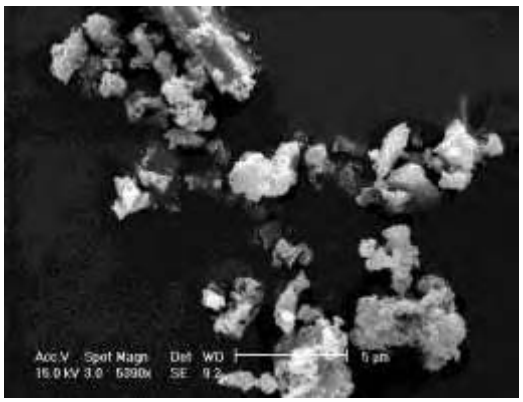

(e) 2200 rpm 20 ^{o}C

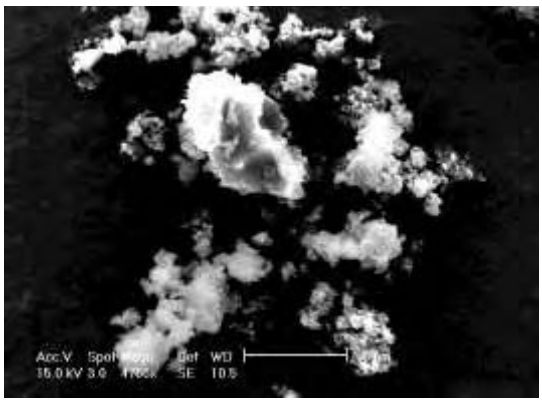

(f) 2200 rpm 40 ^{o}C

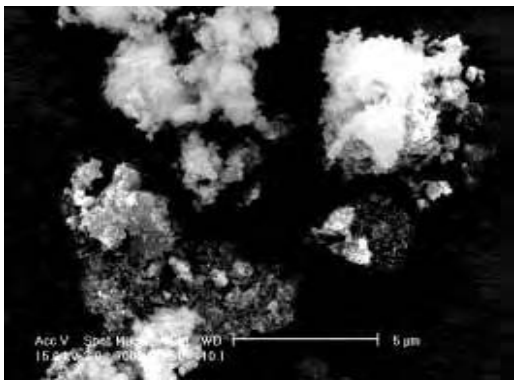

(g) 3000 rpm 20 ^{o}C

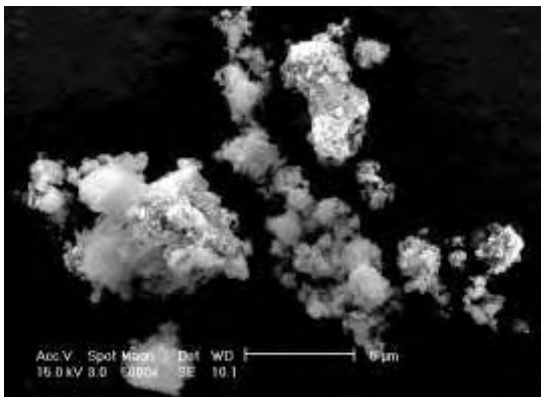

(h) 3000 rpm 40 ^{o}C

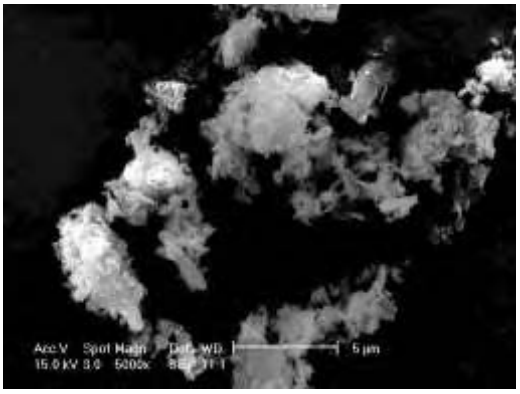

(i) 7000 rpm 20 ^{o}C

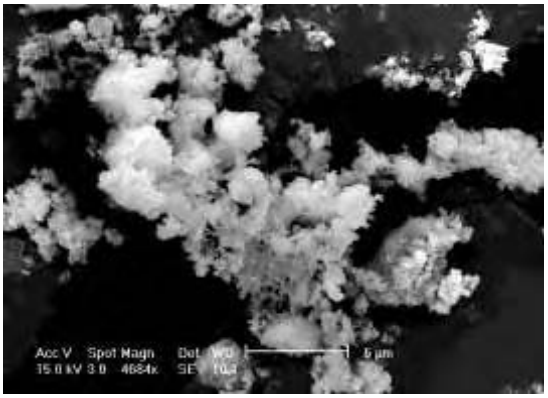

(j) 7000 rpm 40 ^{o}C

Figure 3.11 SEM images of HAp after processing at different agitation rates and temperatures.

3.4.4 Transmission Electron Microscope (TEM)

Table 3.1 and 3.2 shows TEMs of post-sintered HAp particles obtained from processing with the overhead stirrer and homogeniser, respectively. The mean size range of the particles obtained is between 43 and 68 nm. The particles are generally cuboid-like at lower rpm with the overhead stirrer (images in Table 3.1; while particles with an elongated ellipse-like morphology were obtained at higher rpm with the homogeniser (images in Table 3.2). (Note, the equivalent particle diameter was used for the non-uniform particles obtained at higher agitation rates). This behaviour can be explained by the shear produced by the agitation equipment. The overhead stirrer and homogeniser operate on similar concepts in that they both induce shear into the fluid. The homogeniser is a mechanical blade-type and at high rpm would have induced high shear in the mixing zone, creating a vortex which built up aggressive flow behaviour within the system. The Rushton turbine impeller attached to the overhead stirrer would have also produced shear but at a lower level as a result of less energy

input at the lower rpm. At high rpm, the high energy dissipation would lead to increased nucleation rates, which would lead to smaller particles, and at the same time affect mechanism of crystal growth and the subsequent morphology [Ding et al. (2008)].

Feng et al. (2005) used TEM images to report average HAp particle diameters between 10 to 15 nm with an ellipse-like morphology. Fathi et al. (2007 & 2008) also reported an ellipse-like morphology with particle sizes between 20 to 35 nm that were dependent on the aging duration and sintering temperature. Particle sizing was also carried out from XRD analyses in conjunction with Scherrer's formula and the sizes are also reported in Table 3.1 and 3.2. Fathi et al. (2007 & 2008) used this method to estimate the primary size of particles and then corroborated their calculations with TEM images. However, neither Feng nor Fathi's paper mentioned the type of agitator and the agitation rate used. In a similar light, Krajewski et al. (2005) produced carbonated hydroxyapatite particles, however they have not shown TEM images of their particles to enable a comparison to be made. The particle sizes of 43 to 68 nm seen in the TEM images above compare well with those of Fathi et al. (2007) and signify the grain particle size.

Stirring Temp.	200 rpm		800 rpm		1200 rpm		1800 rpm		2200 rpm	
20 °C	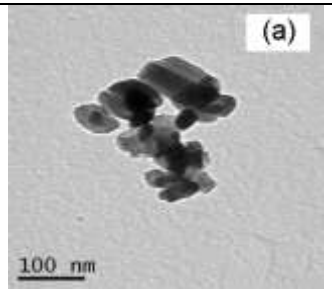		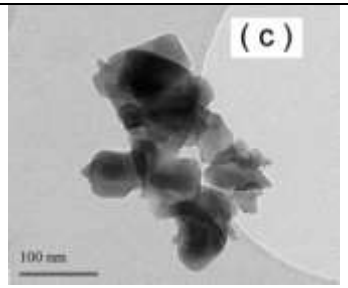		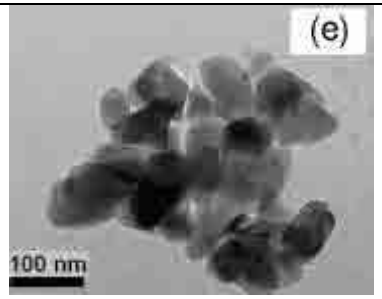		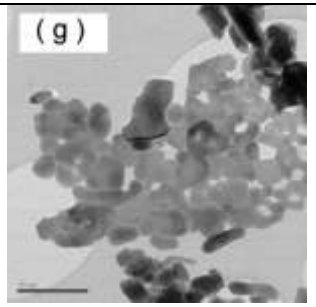		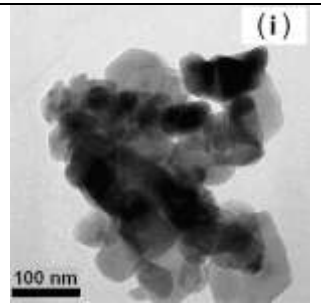	
Particle Size	TEM 64 ± 8 nm	Scherrer's 56 nm	TEM 61 ± 7 nm	Scherrer's 53 nm	TEM 60 ± 9 nm	Scherrer's 49 nm	TEM 57 ± 5 nm	Scherrer's 48 nm	TEM 54 ± 6 nm	Scherrer's 45 nm
40 °C	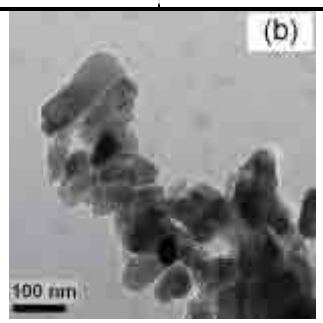		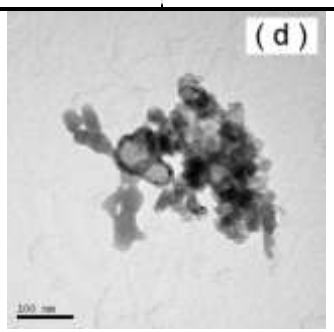		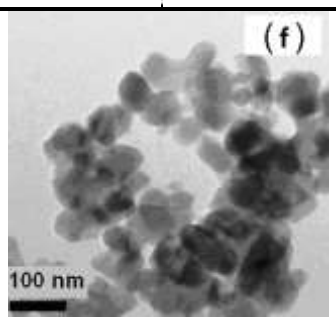		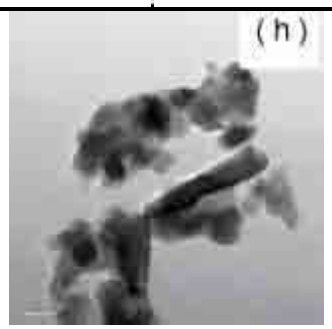		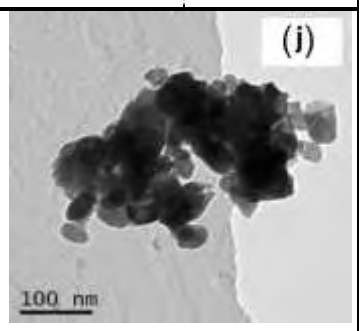	
Particle Size	TEM 68 ± 9 nm	Scherrer's 54 nm	TEM 63 ± 6 nm	Scherrer's 53 nm	TEM 61 ± 8 nm	Scherrer's 50 nm	TEM 57 ± 8 nm	Scherrer's 48 nm	TEM 56 ± 8 nm	Scherrer's 46 nm

Table 3.1 TEM images and particle size estimations based upon the images and Scherrer's formula (Eqn. 1) for HAp samples produced with the overhead stirrer.

Stirring Temp.	3000 rpm		4000 rpm		5000 rpm		6000 rpm		7000 rpm	
20 °C	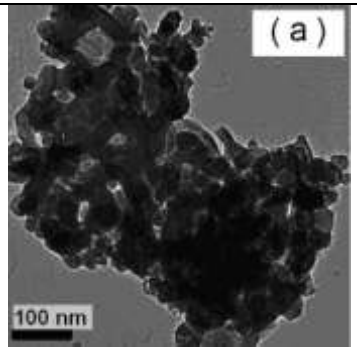		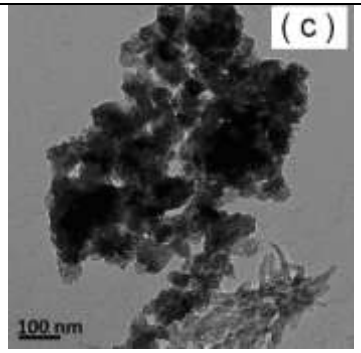		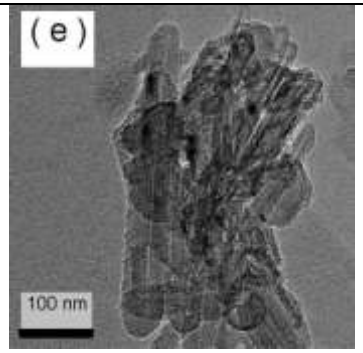		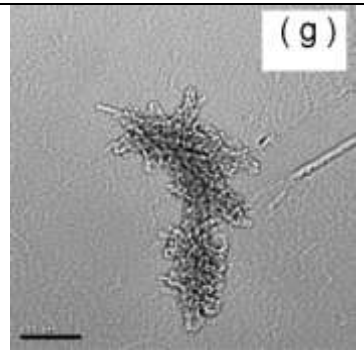		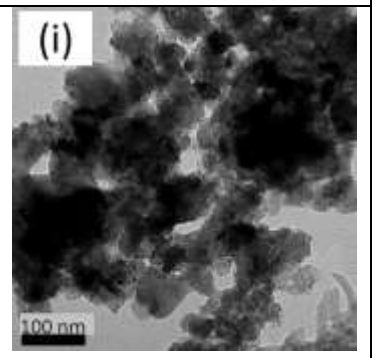	
Particle Size	TEM	Scherrer's	TEM	Scherrer's	TEM	Scherrer's	TEM	Scherrer's	TEM	Scherrer's
	47 ± 5 nm	41 nm	60 ± 9 nm	50 nm	54 ± 6 nm	45 nm	47 ± 5nm	41 nm	43 ± 4 nm	38 nm
40 °C	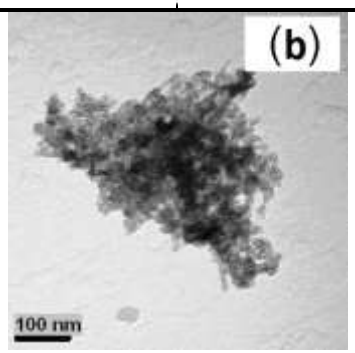		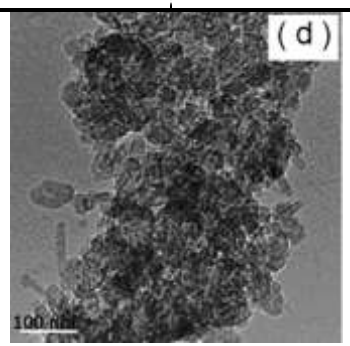		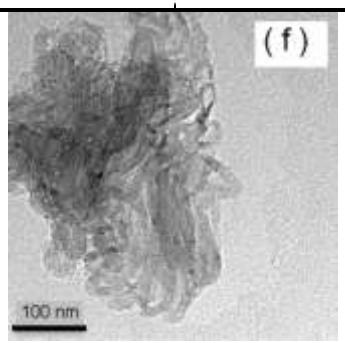		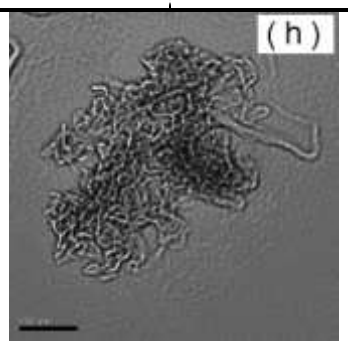		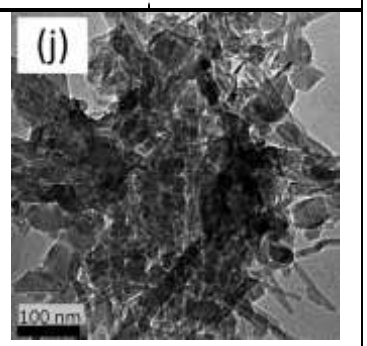	
Particle Size	TEM	Scherrer's	TEM	Scherrer's	TEM	Scherrer's	TEM	Scherrer's	TEM	Scherrer's
	52 ± 6 nm	45 nm	61± 8 nm	49 nm	56 ± 8 nm	46 nm	52 ± 6nm	45 nm	45 ± 5 nm	39 nm

Table 3.2 TEM images and particle size estimations based upon the images and Scherrer's formula (Eqn. 1) for HAp samples produced with the homogenizer.

3.4.5 Dynamic Light Scattering (DLS)

Particle sizing measurements by DLS was undertaken for all HAp samples for both reaction temperatures and are shown in Table 3.3 (unfiltered) and Table 3.4 (filtered). Generally it can be observed that a lower agitation rate led to larger sized agglomerates. Samples were sonicated for one hour to disperse the particles prior to DLS measurements. Sonication is a commonly used technique to disperse agglomerates, as it can pull the liquid apart to form evacuated cavities. The formation and destruction of these cavities can impose a shear force on agglomerates, capable of overcoming the van der Waals force holding them together. Simultaneously, cavity formation and destruction can also enhance agglomeration in the liquid by promoting interactions and contact of particles by kinetic coagulation. The DLS measurements showed a disparity in the particle size compared to the sizes seen in the SEM images (Figure 3.10). Average values between 145 to 219 nm ($P<0.05$) were obtained and indicated that kinetic coagulation had occurred as the particle size could not be further reduced by sonication. The polydispersity indice (PDI) values for the filtered samples (0.108 to 0.167) indicate that the particles formed as agglomerates and that a single species is not present, which reflected in the microscopic images. A near-monodisperse system would have a PDI value of 0.1 or lower, which the filtered samples are close to this value. In the unfiltered samples, the particles aggregated to form agglomerates. The filtered samples resulted in smaller particles but the PDI values still implied that aggregation of the primary particles had occurred but to less extent. Filtering removes larger agglomerates and this leads to small size fraction of the HAp particles.

Stirring rate (rpm)	Temperature (^{o}C)	Particle Size by DLS *(nm)	PDI
200	20	372 ± 18	0.249
	40	405 ± 13	0.269
400	20	531 ± 14	0.276
	40	473 ± 15	0.256
800	20	384 ± 17	0.253
	40	427 ± 16	0.233
1000	20	533 ± 16	0.245
	40	386 ± 15	0.232
1200	20	352 ± 22	0.251
	40	426 ± 16	0.231
1400	20	502 ± 20	0.254
	40	465 ± 15	0.243
1800	20	512 ± 16	0.234
	40	467 ± 18	0.265
2000	20	431 ± 15	0.253
	40	535 ± 16	0.231
2200	20	496 ± 12	0.235
	40	465 ± 17	0.256
3000	20	376 ± 19	0.238
	40	432 ± 16	0.245
4000	20	408 ± 13	0.250
	40	503 ± 16	0.217
6000	20	390 ± 16	0.245
	40	453 ± 18	0.256
7000	20	465 ± 13	0.275
	40	488 ± 17	0.265

*standard deviation of the mean for 3 batches with 3 replicates for each batch

Table 3.3 Particle size measurement by DLS (unfiltered).

Stirring rate (rpm)	Temperature (^{o}C)	Particle Size by DLS *(nm)	PDI
200	20	211 ± 12	0.128
	40	219 ± 7	0.125
400	20	203 ± 8	0.136
	40	206 ± 5	0.146
800	20	184 ± 5	0.143
	40	182 ± 3	0.155
1000	20	182 ± 6	0.156
	40	178 ± 5	0.164
1200	20	162 ± 7	0.114
	40	166 ± 7	0.108
1400	20	164 ± 3	0.156
	40	166 ± 5	0.167
1800	20	160 ± 4	0.167
	40	156 ± 6	0.138
2000	20	154 ± 5	0.159
	40	153 ± 6	0.147
2200	20	148 ± 1	0.126
	40	154 ± 4	0.118
3000	20	150 ± 6	0.130
	40	151 ± 2	0.132
4000	20	151 ± 3	0.126
	40	152 ± 2	0.142
6000	20	146 ± 5	0.136
	40	147 ± 6	0.155
7000	20	145 ± 1	0.133
	40	145 ± 3	0.120

*standard deviation of the mean for 3 batches with 3 replicates for each batch

Table 3.4 Particle size measurement by DLS (filtered).

The particle size estimations by Scherrer's formula are much more comparable to those observed in the TEM images, whereas the DLS measurements gave the sizes of agglomerated particles and not of the primary nanoparticles.

3.4.6 Effect of agitation rate on particle size

The Power number (*Np*) is a useful parameter to determine the power required for agitation, whereas the Reynolds number (*Re*) is used to characterise the flow regimes in a stirred tank, which are either laminar (Re < 2000), turbulent (Re > 10,000) or transitional flow (Re 2000 – 10,000) [Ding et al. (2008)]. Both the Power number and Reynolds number vary with agitation rate. The Power number is given by:

$$\text{Power Number} = Np = \frac{P}{\rho n^3 D^5} \qquad \textbf{Equation 3.3}$$

where, P is power (W), ρ is ethanol density (kg m^{-3}), n is rotational speed (rpm 60^{-1}) and D is the diameter of the impeller (0.05 m for the overhead stirrer and 0.019 m for the homogeniser). The values of *Np* were obtained from power curve correlations given in references by Ding et al. (2008) and Sinnott for the two agitators based on the respective Re numbers. 0.4 was used for the Rushton turbine and 4.5 for the homogenizer.

The impeller Reynolds number is given by:

$$\text{Re} = \frac{\rho N D^2}{\mu} \qquad \textbf{Equation 3.4}$$

where ρ is ethanol density (kg m^{-3}), N is rotational speed (rpm 60^{-1}), D is the diameter of impeller (dimensions as Equation 3) and μ is ethanol viscosity (kg $m^{-1}s^{-1}$). The densities and viscosities of ethanol at the temperature conditions were obtained from the literature [Paul et al. (2004)]. The relationship between power and particle size and Re number and particle size

for the two particle sizing methods (TEM and DLS) at 20 ^{o}C and 40 ^{o}C are shown in Figures 3.12 and 3.13, respectively.

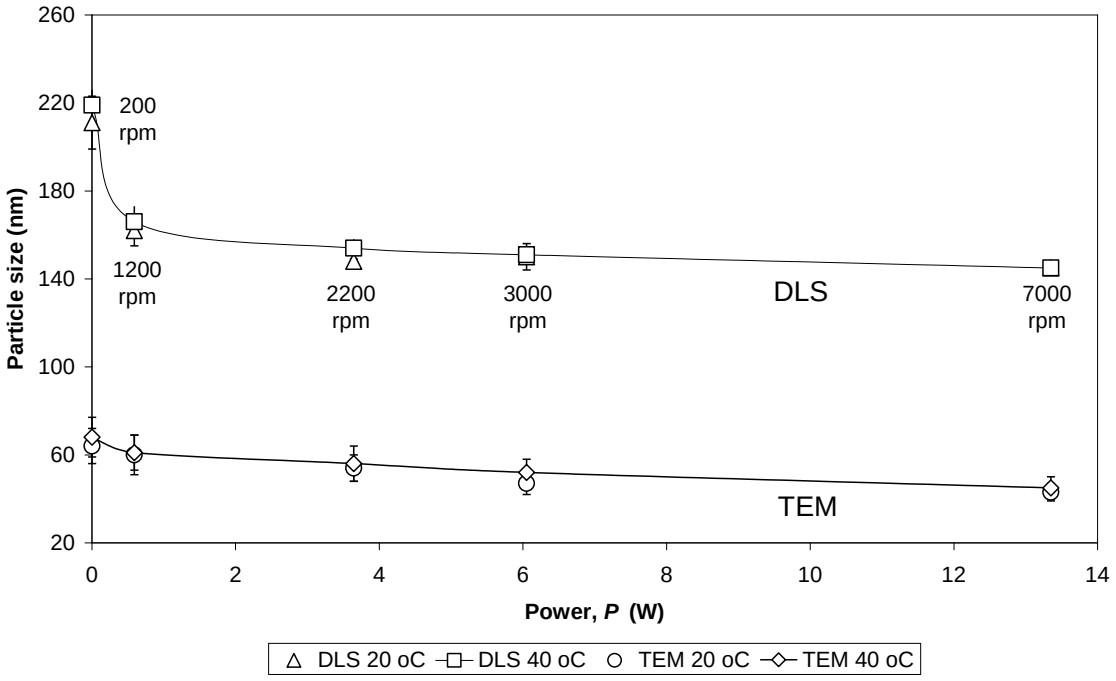

Figure 3.12 Effect of Power on Particle size (nm) at 20 ^{o}C and 40 ^{o}C.

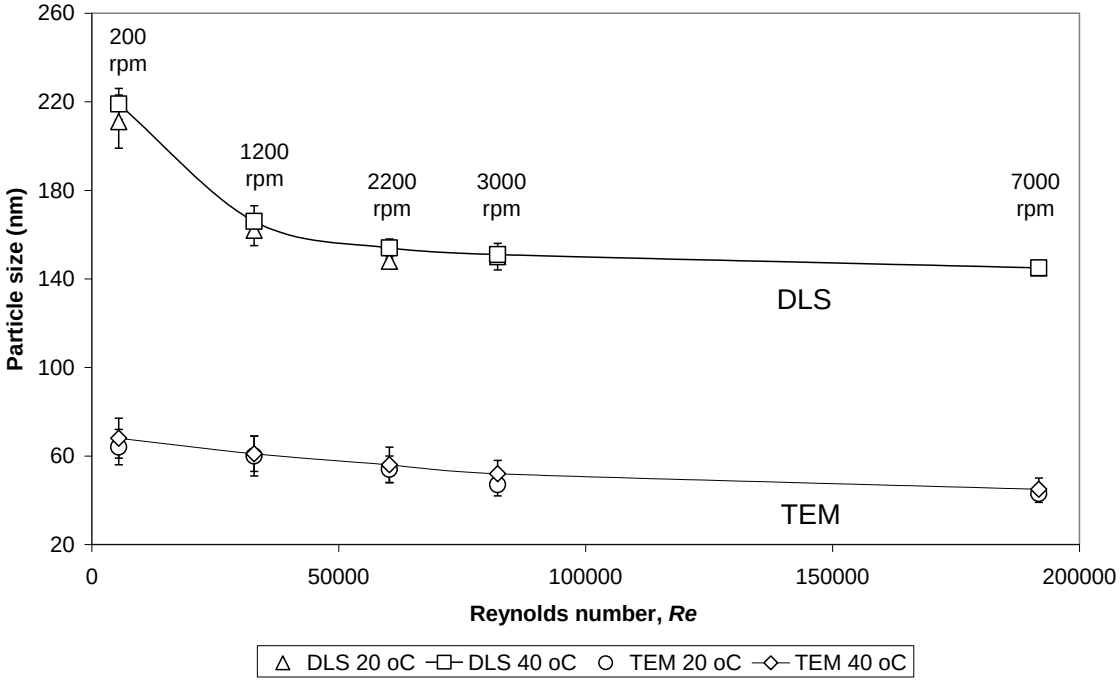

Figure 3.13 Influence of Re Numbers on Particle size (nm) at 20 ^{o}C and 40 ^{o}C.

It can be seen that for all particle sizing methods higher power resulted in smaller particle sizes. A similar trend is seen for the effect of Re number on particle size. As the power increases the energy introduced into the system would affect the kinetics of nuclei aggregation leading to the formation of smaller particles. At lower Re values, there is less inertia force accumulating in the system. At higher Re numbers there is high energy dissipation and turbulence in the mixing zone, which would lead to increased nucleation rate and also the break-up of larger aggregates into smaller secondary aggregates as evidenced by the decreased sizes for the respective TEM and DLS data [Lange (1967)]. It can be seen from Figure 3.13 and Table 3.4 that the agitation rate has an influence upon the filtered agglomerate size obtained by DLS until higher agitation rates (>2200 rpm) and Re numbers (turbulence) are reached. Around this rpm it can be inferred that kinetic coagulation occurred, which led to the formation of stable aggregates and therefore particle size tends to become less dependent on agitation rate.

The effect of agitation rate on primary particle size can be seen by comparing the TEM sizing results at 200 rpm and 7000 rpm for both temperatures (see Table 3.1 and 3.2 and Figure 3.13). It can be seen that the primary particle size decreased steadily with an increase in agitation rate. While gentle agitation causes nucleation in solutions that are otherwise stable, increased agitation creates an even greater tendency to form secondary nuclei [Pacek et al. (2007)] and would explain the reduction in the primary particle size over the agitation rates studied.

3.4.7 Effect of temperature

Lower temperatures are known to influence the rate of growth and size of crystals through its effect on supersaturation [Mullin (1960 & 2000), Myerson & Ginde (1993), Jones & Mullin (1974)]. In this work, both TEM and DLS data (see Tables 3.1, 3.2 and 3.4) show very small differences for both the agglomerated and primary particle sizes obtained at 20 and 40 ^{o}C, with slightly larger sizes being obtained at higher temperature. On one hand, higher temperature would lead to a decrease in solution viscosity which would accelerate the collision rate of nuclei and therefore lead to smaller particles, however at 40 ^{o}C a higher collision rate may have also led to increased probability of coalescence and the observed small increase in particle size [Cheng & Li (2009)]. The temperature has less effect on the agglomerate sizes obtained by DLS at higher rpm. This can be attributed to the formation of stable aggregates in the mixing zone.

3.4.8 Effect of Mg^{2+} on HAp particle size

The effect of incorporating Mg^{2+} ions into the HAp nanoparticles has been reported to transform larger particles (2500 to 500 nm) to more smaller particles of 100 to 500 nm as a result of varying the concentration of the Mg^{2+} and precipitation rate [Chowdhury et al. (2004)]. Chowdhury et al. (2004) have produced Ca-Mg hydroxyapatite particles approximately between 100 to 500 nm depending on the Mg fraction. In a similar light, Miyaji et al. (2005) have produced zinc-substituted calcium hydroxyapatite between approximately 200 to 1100 nm depending on the Zn fraction, and Krajewski et al. (2005) have reported carbonated hydroxyapatites, though particle sizes were not given. In this chapter a series of experiments were undertaken to study the effects of agitation rate and

magnesium concentrations on particle size using the sol gel technique at 20 ^{o}C and therefore extended the work of Chowdhury et al. (2004).

Post sintering the primary particles exhibited similar morphologies to those of HAp particles over the range of agitation rates. TEM and filtered DLS particle size data obtained at different agitation rates and magnesium concentrations are shown in Figure 3.14. As for HAp particles, an increase in agitation rate also led to a decrease in the primary particle and agglomerate sizes for the reasons discussed earlier. In general, the primary particle and agglomerate sizes decreased with higher concentrations of $MgCl_2$. The inhibitory effect of Mg^{2+} on particle growth creates a distorted atomic structure within the hydroxyapatite due to the replacement of Ca^{2+} with Mg^{2+}, which subsequently slows the growth of the particles [Miyaji et al. (2005)] and results in the smaller particle sizes. The relatively smaller ionic radius of the Mg^{2+} ions (0.65 Å) compared to the Ca^{2+} ions (0.99 Å) [Blumenthal (1989)], could further contribute to the effect on the HAp particle size. At higher $MgCl_2$ concentrations (60 to 140 mM) the particle size became less dependent on concentration for agitation rates above 2200 rpm due to the stronger influence of agitation rate over concentration.

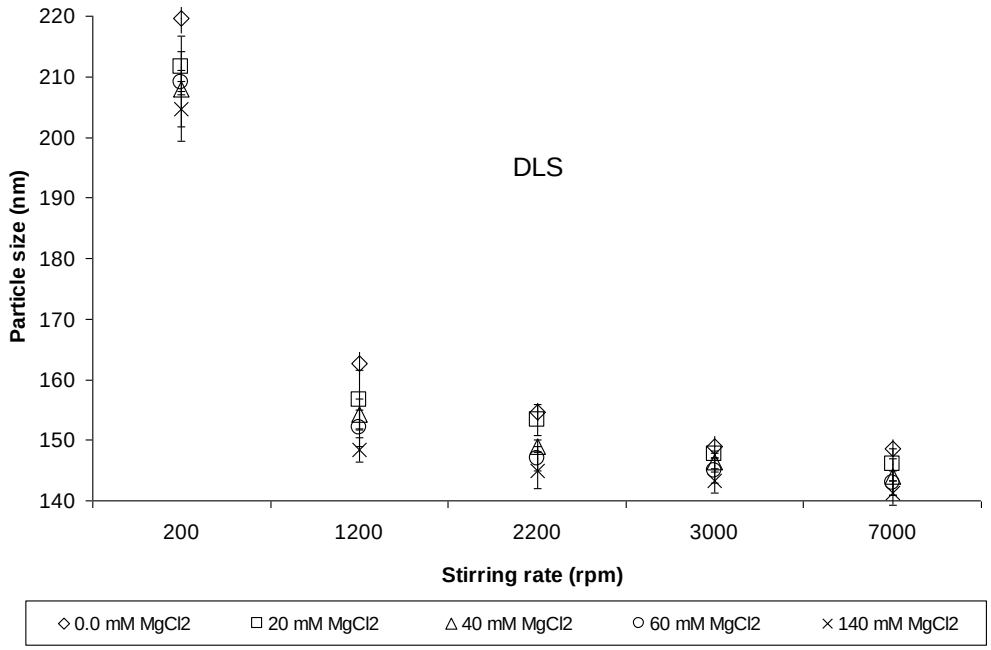

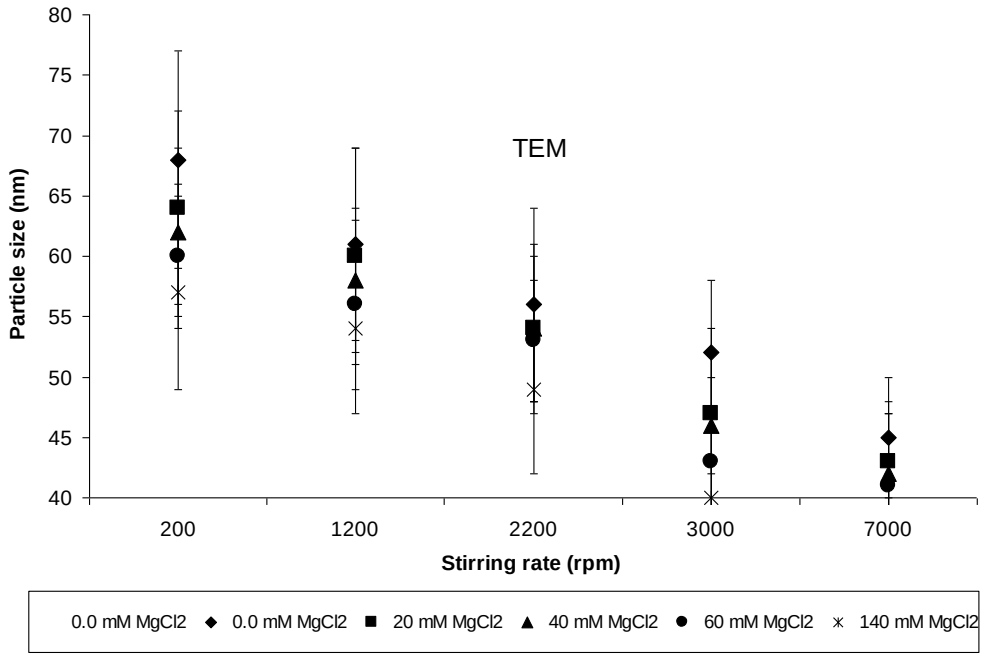

Figure 3.14 Effect of Mg^{2+} intercalation on HAp particle size for different $MgCl_2$ concentrations and agitation rates at 20 ^{o}C.

3.5 Conclusions

The effect of process conditions on the particle size of HAp and intercalated HAp-Mg particles are reported. It can be concluded that the primary particle size for both HAp and HAp-Mg particles decreased with higher agitation rates and can be explained in terms of the power input and turbulence within the mixing zone influencing the nucleation rate. At higher agitation rates the filtered DLS data showed the formation of stable agglomerates above 2200 rpm as the agitation rate did not significantly affect the particle size. An increase in temperature from 20 to 40 ^{o}C had a slight effect on particle size. The intercalation of Mg into the HAp structure led to a decrease in particle size with increased $MgCl_2$ concentration and increased agitation rate, although this became less significant at agitation rates above 2200 rpm. Different particle morphologies can be obtained at different agitation rates, which are dependant on equipment selection. Cuboid-like particles were obtained at lower agitation rates with the overhead stirrer while elongated particles can be obtained at higher agitation rate using the homogeniser.

3.6 References:

Balamurugan, A. Rebelo, A. H. S. Lemos, A. F. Rocha, J. H. G. Ventura, J. M. G. Ferreira, J. M. F. 2008. Suitability evaluation of sol-gel derived Si-substituted hydroxyapatite for dental and maxillofacial applications through *in vitro* osteoblasts response. Dental Materials 24: 1374 – 1380.

Bigi, A. Falini, G. Foresti, E. Gazzano, M. Ripamonti, A. Roveri, N. 1993. Magnesium influence on hydroxyapatite crystallization, J. Inorg. Biochem 49: 69 – 78.

Blumenthal, N. C. 1989. Mechanisms of inhibition of calcification. Clin. Orthop. 247: 279 – 289.

Cheng, W. Li, Z. 2009. Precipitation of nesquehonite from homogeneous supersaturated solutions. Cryst. Res. Technol., 44: 937 – 947.

Chowdhury, E. H. Kunou, M. Nagaoka, M. Kundu, A. K. Hoshiba, T. Akaike, T. 2004. High-efficiency gene delivery for expression in mammalian cells by nanoprecipitates of Ca-Mg phosphate. Gene 341: 77 – 82.

Deppert, W. R. Lukacin, R. 1999. Chapter 5 Hydroxyapatite Chromatography. Protein Liquid Chromatography 271 – 299.

Ding, P. Pacek, A. W. 2008. De-agglomeration of goethite nano-particles using ultrasonic comminution device. Powder Technology, 187: 1 -10.

Epple, M. Sokolova, V. 2008. Inorganic Nanoparticles as Carriers of Nucleic Acids into Cells. Angew. Chem. Int. Ed. 47: 1382 – 1395.

Fadeev, I. V. Shvorneva, L. I. Barinov, S. M. Orlovskii, V. P. 2003. Synthesis and structure of magnesium-substituted hydroxyapatite, Inorg. Mater., 39 (9): 947 – 950.

Fathi, M. H. Hanifi, A. 2007. Evaluation and characterization of nanostructure hydroxyapatite powder prepared by simple sol-gel method. Materials Letters 61: 3978 – 3983.

Fathi, M. H. Hanifi, A. Mortazavi, V. 2008. Preparation and bioactivity evaluation of bone-like hydroxyapatite nanopowder. Journal of Materials Processing Technology 202: 536 – 542.

Feng, W. Mu-sen, L. Yu-peng, L. Yong-xin, Q. 2005. A simple sol-gel technique for preparing hydroxyapatite nanopowders, Materials Letters 59: 916 – 919.

Feng, Y. Haifeng, G. Haijiao, Z. Xiulan, H. 2010. Polymeric micelle-templated synthesis of hydroxyapatite hollow nanoparticles for a drug delivery system. Acta Biomaterialia 6: 2212 – 2218.

Hannay, J. B. Hogarth, J. 1879. On the solubility of solids in gases. Proc. Roy. Sec. (London) 29: 324.

Ichiro, O. Toshiharu, Y. Hai-Ying, J. Yoshinori, I. Hirobumi, H. Yoshikiyo, A. Masanori, N. Tetsunori, O. Kowichi, J. 2004. Combination of porous hydroxyapatite and cationic liposomes as a vector for BMP-2 gene therapy. Biomaterials 25: 4709 – 4718.

Jenkins, R. Synder, R. L. 1996. Introduction to X-ray Powder Diffractometry. John Wiley and Sons: New York.

Jones, A. G. Mullin, J. W. 1974. Programmed cooling crystallization of potassium sulphate solutions. Chem. Eng. Sci. 29: 105 – 118.

Kannan, S. Lemos, I. A. F. Rocha, J. H. G. Ferreira, J. M. F. 2005. Synthesis and characterisation of magnesium substituted biphasic mixtures of controlled hydroxyapatite/β-tricalcium phosphate ratios. J. Solid State Chem. 178: 3190 – 3196.

Kano, J. Zhang, Q. Saito, F. Baron, M. Nzihou, A. 2006. Synthesis of hydroxyapatite with the mechanochemical treatment products of PVC and CaO. Process Safety and Environmental Protection 84: 309 – 312.

Kawata, M. Uchida, H. Itatani, K. Okada, I. Koda, S. Aizawa, M. 2004. Development of porous ceramics with well-controlled porosites and pore sizes from apatite fibers and their evaluations. J. Mater. Sci. Mater. Med. 817 – 823.

Krajewski, A. Mazzocchi, M. Buldini, P. L. Ravaglioli, A. Tinti, A. Taddei, P. Fagnano, C. 2005. Synthesis of carbonated hydroxyapatites: efficiency of the substitution and critical evaluation of analytical methods. Journal of Molecular Structure, 744 – 747: 221 – 228.

Landi, E. Tampieri, A. Celotti, G. Sprio, S. 2000. Densification behaviour and mechanisms of synthetic hydroxyapatites. J. Eur. Ceram. Soc. 20: 2377 – 2387.

Lange's Handbook of Chemistry 1967. 10th Ed. McGraw-Hill, New York.

Lim, G. K. Wang, J. Ng, S. C. Gan, L. M. 1999. Nanosized hydroxyapatite powders from microemulsions and emulsions stabilised by a biodegradable surfactant. J. Mater. Chem. 9: 1635.

Miyaji, F. Kono, Y. Suyama, Y. 2005. Formation and structure of zinc-substituted calcium hydroxyapatite. Mater. Res. Bull. 40: 209 – 213.

Molle, P. Lienard, A. Gramsik, A. 2005. Apatite as an interesting seed to remove phosphorus from waste-water in constructed wetlands. Water Sci. Technol. 51:193 – 203.

Mullin, J. W. Raven, K. D. 1960. Nucleation in agitated solutions. Nature, 190:251.

Mullin, J. W. 2000. Crystallization. Oxford, UK: Butterworth-Heinemann.

Myerson, A. S. Ginde, R. 1993. Crystals, crystal growth and nucleation. In: Handbook of Industrial Crystallization. St. Louis, MO: Butterworth-Heinemann; 33 – 63.

Ni, G. X. Lu, W. W. Xu, B. Chiu, K. Y. Yang, C. Li, Z. Y. Lam, W. M. Luk, K. D. K. 2006. Interfacial behaviour of strontium-containing hydroxyapatite cement with cancellous and cortical bone. Biomaterials 27:5127 – 5133.

Pacek, A. W. Ding, P. Utomo, A. T. 2007. Effect of energy density, pH and temperature on de-aggregation in nano-particles/water suspensions in high shear mixer. Powder Technology 173: 203 – 210.

Paul, E. L. Atiemo-Obeng, V. A. Kresta, S. M. 2004. Handbook of Industrial Mixing. Wiley-Interscience.

Pons, M-N. Vivier, H. Delcour, V. Authelin, J-R. Paillères-Hubert, L. 2002. Morphological analysis of pharmaceutical powders. Powder Tech. 128: 276-286.

Rodriquez-Clemente, R. Lopez-Macipe, A. Gomez-Morales, J. Torrent-Burgues, J. Castano, V. M. 1998. Hydroxyapatite precipitation: A case of nucleation-aggregation-agglomeration-growth mechanishm. J. Eur. Ceram. Soc. 18: 1351 – 1356.

Shimbayashi, S. Hashimoto, N. Kawamura, H. Uno, T. Mineral Scale Formation and Inhibition. In: Amjad, Z (Ed.), Plenum Press: New York, 14 – 15.

Sinnott, R. K. Coulson & Richardson's Chemical Engineering. Volume 6: Chemical Engineering Design, 4th ed. (Butterworth – Heinemann), 473 – 474.

Suchanek, W. L. Byrappa, K. Shuk, P. Riman, R. E. Janas, V. F. TenHuisen, K. S. 2004. Preparation of magnesium-substituted hydroxyapatite powders by the mechanochemical-hydrothermal method. Biomaterials 25: 4647 – 4657.

Tas, A. C. 2000. Combustion synthesis of calcium phosphate bioceramic powders. J. Eur. Ceram. Soc. 20: 2389.

Varma, H. Babu, S. S. 2005. Synthesis of calcium phosphate bioceramics by citrate gel pyrolysis method. Ceram. Int. 31: 109 – 114.

Weng, W. J. Baptista, J. L. 1997. A new synthesis of hydroxyapatite. J. Eur. Ceram. Soc. 17: 1151-1156.

Yoshmura, M. Suda, H. Okmoto, K. Loku, K. 1994. Hydrothermal synthesis of biocompatible whiskers. J. Mater. Sci. 29: 3399.

4.0 Hydroxyapatite (HAp) prepared by Anti-solvent processing

4.1 Introduction

Supercritical fluid (SCF) technology has found its place in many industrial applications, such as nanoparticle fabrication, food processing (decaffeination of coffee beans as an example), chemical manufacturing, extraction, dry cleaning, polymer processing, waste treatment and particle coating [Palakodaty et al. (2002), Adschiri & Arai (2002), Hay & Khan (2002)]. It is chosen as an alternative processing method, as it can avoid the use of harsh and toxic organic solvent. SCF technology, specifically supercritical carbon dioxide ($scCO_2$) is considered a 'green technology', as CO_2 is benign, environmentally friendly, a GRAS solvent, easily available and recyclable [DeSimone (2002)].

SCF technology can be applied to the manufacture of nanoparticles for advanced drug delivery and drug formulations systems. The particles once formed need not undergo further processing or treatment and this feature makes SCF technology amenable to process biomolecules and other sensitive compounds in their native pure state [Chattopadhyay & Gupta (2002)]. There are many routes to produce particles by $scCO_2$; these include for example, Rapid Expansion of Supercritical Solutions (RESS), Gas Anti-Solvent precipitation (GAS), Precipitation from Compressed Antisolvent (PCA), Supercritical Antisolvent process (SAS), and Solution Enhanced Dispersion by Supercritical fluids (SEDS), the process selection depends on the solubility of the active compound in $scCO_2$ [Byrappa et al. (2008)]. In this section, HAp formed from the wet chemistry method is recrystallised by SCF processing using GAS and SEDS methods in order to evaluate the potential of SCF in producing HAp particles. The selection of the GAS method is based on the simplest method of all of the SCF methods, while for the SEDS method has been selected in order to evaluate

the effect of rapid supersaturation and solvent removal on particle formation. The recrystallised particles produced were then characterised by Fourier Transform Infrared Spectroscopy (FTIR), X-ray Diffraction (XRD), High Performance Particle Sizer (HPPS), Scanning Electron Microscopy (SEM) and Transmission Electron Microscopy (TEM).

4.1.1 SCF methods selection

4.1.1.1 Gas Anti-Solvent (GAS) method

Gallagher [Gallagher et al. (1989 & 1992)] first reported using this technique in the recrystallisation of explosive substances of nitroguanidine & cyclotrimethylenetrinitramine (RDX). Generally, in the GAS method, the target active is dissolved in a suitable organic solvent. Adding $scCO_2$ as an antisolvent expands the organic solution causing a reduction of the organic solvent power which leads to the supersaturation of the solution. The particles of the active solute are formed as the active losses its affinity in the organic solvent. The solvent expanded with the $scCO_2$ antisolvent is purged, and the produced particles are washed with additional $scCO_2$ to remove remaining organic solvent. The principle of the antisolvent process is based on a rapid decrease in the solubilisation power of a solvent by addition of a second fluid as antisolvent. Particle size distribution can be controlled by adjusting the values of temperature, pressure and composition [Mishima (2008)]. The main disadvantage of the GAS precipitation process is the difficulty to remove the remaining solvent completely because the process is carried out in a batch process. An additional wash-out treatment with $scCO_2$ may be required for the production of a pharmaceutical product on an industrial scale. The schematic diagram of the GAS rig is shown in Figure 4.1. The method of this technique is given in detail in section 4.2.1.1.

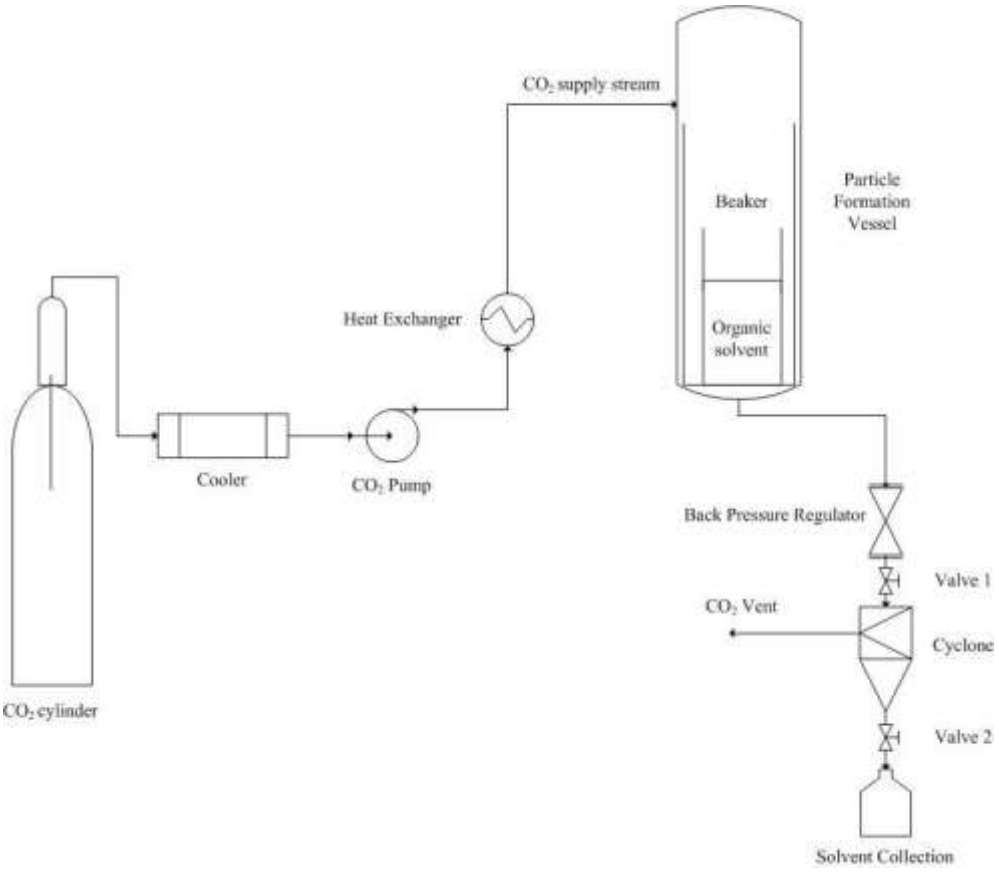

Figure 4.1 Schematic diagram of the GAS rig.

4.1.1.2 Solution Enhanced Dispersion by Supercritical fluids (SEDS) method

The chief developers of SEDS^{TM}, Bradford University, have successfully applied the process to numerous situations, including processing of dyes [Hanna (1994)], lactose [Hanna (1995)] and polystyrene [Hanna (1998)]. Other workers have successfully manufactured proteins of a smaller and more uniform nature than conventional techniques [Sloan et al. (1998)]. The major success of SEDS^{TM} is in the production of intrapulmonary delivery systems, where the particle size needs to be small (<5 μm) but the distribution needs to be very tight. In the SEDS method, particle formation is initiated by the mass transfer of the supercritical fluid into the sprayed droplet and by the rate of solvent transfer into the supercritical phase. In particular, a high mass transfer allows a faster nucleation and a smaller particle size with less agglomeration [Palakodaty et al. (1998)]. The schematic diagram of the SEDS rig and its coaxial nozzle diagram are shown in Figure 4.2 and 4.3 respectively. The method of this technique is given in detail in section 4.2.1.2.

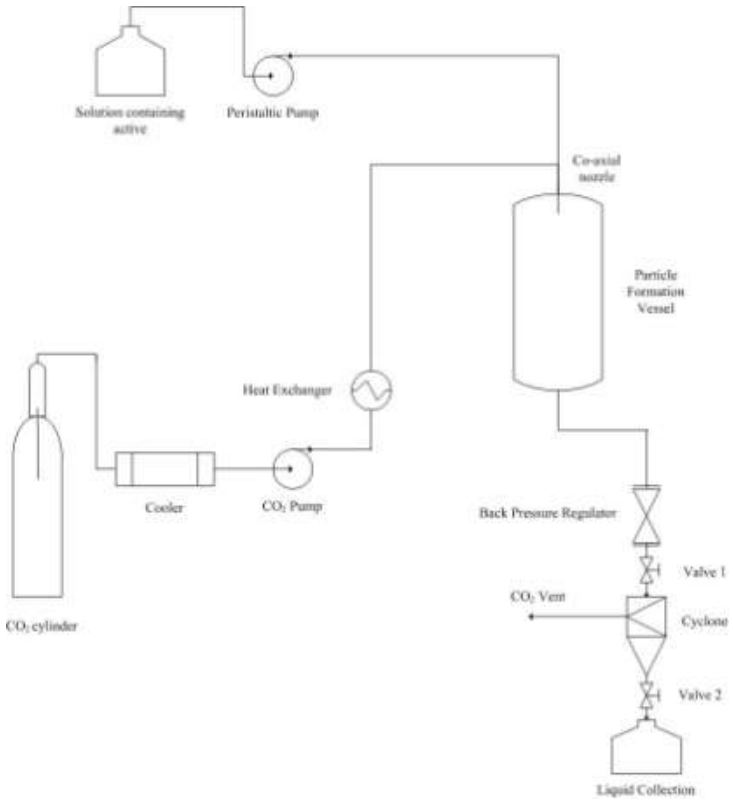

Figure 4.2 Schematic diagram of the SEDS rig.

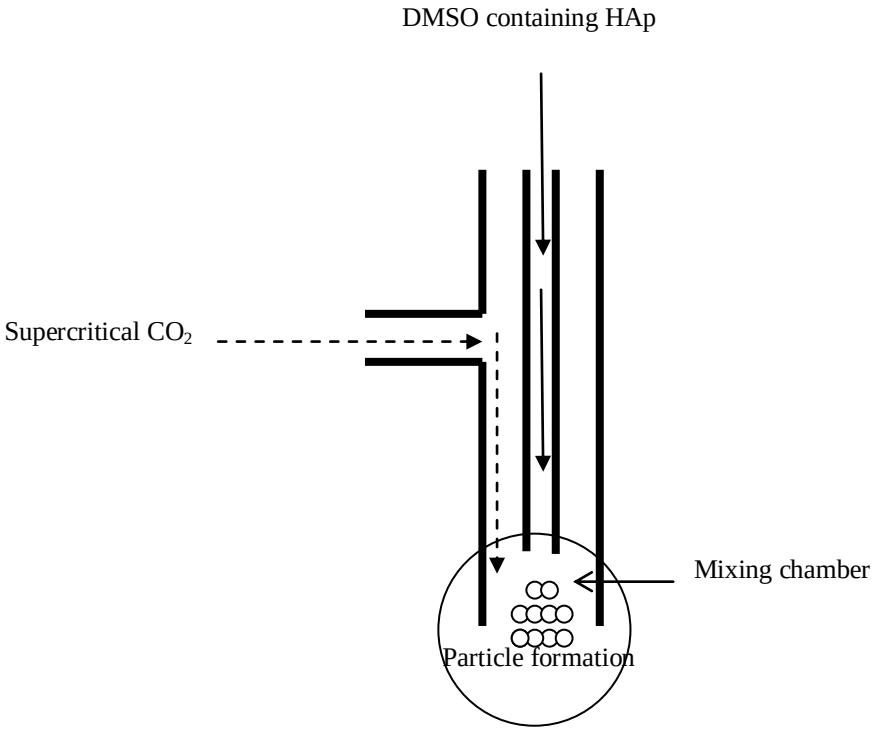

Figure 4.3 The SEDS coaxial nozzle diagram used in this work.

4.1.2 Solvent selection

4.1.2.1 Classes of solvents

Solvents and solutes can be broadly classified into polar (hydrophilic) and non-polar (hydrophobic). The polarity can be measured as the relative permittivity or the dipole moment of a compound. The polarity of a solvent determines the type of compounds it is able to dissolve and with which other solvents or liquid compounds it is miscible. As a rule of thumb, polar solvents best dissolve polar compounds and non-polar solvents best dissolve non-polar compounds, *i.e.* 'like dissolves like'. The Hildebrand solubility parameter is a useful approach for evaluating the solubility of a compound in another [Goodarzi et al. (2010)]. The solubility parameter is a numerical value that indicates the relative solvency of a specific solvent. It is derived from the cohesive energy density of the solvent, which in turn is derived from the heat of vaporisation. Polar solvents can be classified into two categories, which are the polar aprotic solvents (cannot donate hydrogen bonds, but have high dielectric constants and high polarity) and the polar protic solvents (can participate in hydrogen bonding and contains dissociable H^+).

4.1.2.2 Solvent screening

Solvent screening was done in this study as to select a solvent which not only dissolves HAp but is also compatible with supercritical CO_2. In total, 26 solvents were screened. The non-polar solvents tested were benzene, chloroform, cyclohexane, dichloromethane, diethyl ether, ethyl acetate, heptane, hexane and methyl cyclohexane. The polar aprotic solvents tested were 1,4 – dioxane, acetone, acetonitrile, dimethyl formamide (DMF), dimethyl sulfoxide (DMSO), ethyl acetate, isopropyl acetate, methyl ethyl ketone (MEK), N-methyl 2-

pyrrolidone (NMP) and tetrahydrofuran (THF). The polar protic solvents tested were n-butanol, ethanol, isopropanol, methanol, n-propanol, octanol and water.

Solvent screening in this study is based on the solubility of phosphate determined by spectrophotometry. The phosphate dissolved in a solvent was complexed with molybdate-vanadate reagent and its quantity calculated photometrically at 400 nm. The obtained absorbance was then compared with a standard phosphate calibration curve with known amount of phosphate. An amount of 0.1 mg, 0.5 mg, 1.0 mg, 1.5 mg and 2.0 mg of HAp were dissolved in 100 ml of respective solvent that was tested. The solution was then filtered and complexed with molybdate-vanadate until the colour of the solution turned yellow. The calculation of HAp solubility is shown in Chapter 4 Appendix (Appendix 4 A).

HAp is an inorganic and ionic compound. Therefore, it will not dissolve in non-polar solvents, as these solvents do not provide the polarity for the interactions of ions between the solvent and the solute. This was further proven by the insolubilities of any amount of HAp in the non-polar solvents. HAp can easily be dissolved in acidic solution such as acetic acid and formic acid, but the use of these acids is not suitable for the supercritical processing due to their extremely low solubilities in the CO_2 antisolvent. Furthermore, these acids will damage some parts of the supercritical rig which consisted of plastic parts such as the pump tubing, pipings and 'o' ring seals. For the polar aprotic solvents, only DMF and DMSO showed that HAp can be soluble with an amount of 2 mg/l and 3 mg/l respectively. However, due to the toxicity of DMF, this solvent was omitted. Lastly, for the polar protic solvents, an amount of 6 mg/l of HAp can be solubilised in water. Due to the low solubility of water in supercritical CO_2, water will not be used as a solvent in the supercritical processings.

4.1.2.3 Dimethyl sulfoxide (DMSO)

Dimethyl sulfoxide (DMSO) is a chemical compound with the formula of $(CH_3)_2SO$. It is a colourless liquid and is a polar aprotic solvent. It is readily miscible in a wide range of organic solvents as well as water. It is less toxic than other members of this class, such as dimethyl formamide, dimethyl acetamide, *N*-methyl-2-pyrrolidone and HMPA [Kenneth & Artie (2003)]. DMSO is frequently used as a solvent for chemical reactions.

DMSO has been selected as the solvent to dissolve HAp. It showed that it can dissolve 3mg of HAp per litre of DMSO. Furthermore, DMSO has a mutual solubility with CO_2 and has an appreciable volume expansion when used in supercritical processing. This is important for the removal of DMSO by scCO_2 antisolvent. A solubility of 0.49 mole fraction of CO_2 (x_1) and a volume expansion of 135 % (E %) were reported at the processing condition of 8 MPa and 45 ^{o}C [Lucien et al. (2004)]. The solubility data for CO_2 in DMSO are shown in Table 4.1 and Figure 4.4 on the next page:

P (bar)	x_1 (mole fraction)	*E* (%)
T = 298.2 K		
10.3	0.0666	4.5
20.0	0.1358	13.9
30.1	0.2311	27.5
40.2	0.3282	51.3
50.1	0.4775	98.3
55.1	0.5906	150
T = 308.2 K		
10.4	0.0524	8.5
30.0	0.1633	28.1
50.1	0.3128	64.1
60.1	0.4134	102
65.1	0.4919	134
70.4	0.5571	205
T = 318.2 K		
10.1	0.0439	9.6
50.0	0.2507	46.2
60.1	0.3196	65.0
70.4	0.3937	94.0
85.2	0.5411	181
90.4	0.6004	472

Table 4.1 Solubility (x_1) of CO_2 (1) in DMSO (2) at various temperatures [Lucien et al. 2004].

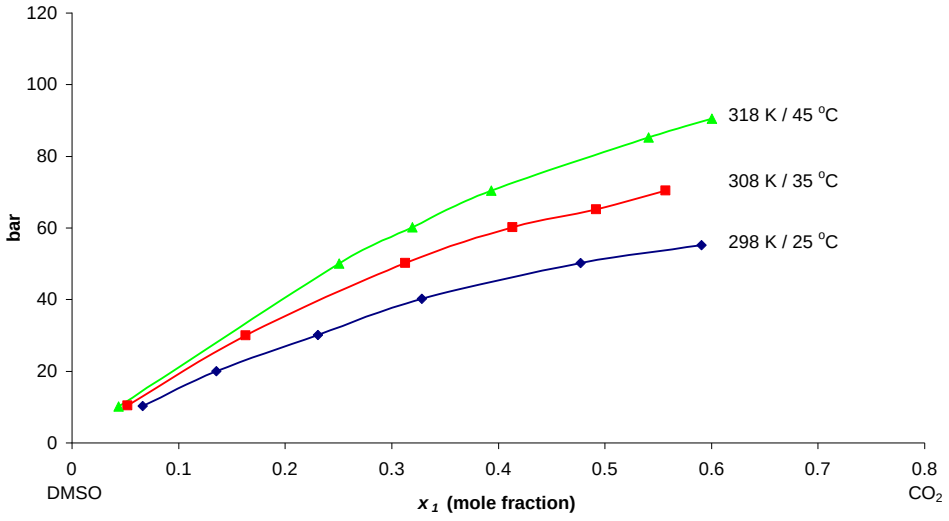

Comparison of $P - x_1$ data for the CO_2-DMSO binary system.

Figure 4.4 Data of CO_2 interaction with DMSO [Lucien et al. (2004)].

The data shows that at 100 bar and 318 K (45 °C), CO_2 and DMSO are miscible which is advantageous for SCF anti-solvent processings (CO_2 solubility is 0.61 mole fraction).

According to the GAS Law (Henry's Law), the solubility of a gas in a solvent is directly proportional to the partial pressure of that gas above the solvent, thus at these conditions (100 bar and 318K/45 ^{o}C), higher solubility of CO_2 in DMSO is observed.

4.2 Experimental

4.2.1 Materials and methods

4.2.1.1 Preparation of HAp particles by GAS method.

A GAS (Gas Anti-Solvent) experiment was carried out by first preparing a HAp solution. A HAp solution with a concentration of 3 mg/L in DMSO (Sigma Aldrich, UK, CAS number 67-68-5, 99.5% purity and 400 ppm residual water) was prepared and stirred for 3 hours at 600 rpm prior to supercritical processing. For each of the GAS batches, a HAp solution of 50 ml was used. The experimental work was carried out by varying a number of parameters; temperature (40 ^{o}C, 50 ^{o}C or 60^{o}C) and pressure (100 bar, 150 bar or 200 bar). The CO_2 (BOC UK, CAS number 124-38-9) flowrate into the vessel was set at 40 g/min for all of the experiments.

Temperature	Pressure
40 ^{o}C	100 bar
	150 bar
	200 bar
50 ^{o}C	100 bar
	150 bar
	200 bar
60 ^{o}C	100 bar
	150 bar
	200 bar

Table 4.2 GAS experimental conditions.

The GAS processing rig consisted of a 500 ml pressure vessel (Parr, Moline, USA) in which a beaker containing the HAp solution was placed. The CO_2 flowrate was set by the CO_2 pump, using integral software (Thar Instrument Process Suite, version 2.05). Prior to GAS processing, the rig was heated to the desired operating temperature (to within ± 1 ^oC), also by the integral software. CO_2 was then introduced into the system to reach the respective set pressure. A back pressure regulator was used to maintain the pressure within the system (to within ± 1 bar). After 6 hours the CO_2 supply was stopped and the supercritical processing rig was depressurised and cooled down. During the process, the CO_2 had stripped the DMSO which led to supersaturation and the formation of HAp particles. The particles produced were retained inside the beaker and were removed for analysis. The waste DMSO solvent was collected by opening the cyclone valve and was disposed in a safe manner. Before disposal, the DMSO was analysed for any HAp content. Each GAS experimental condition was repeated 6 times. The results were reproducible and the experimental data is presented in Appendix 4B.

4.2.1.2 Preparation of HAp particles by SEDS method.

HAp powder used in the SEDS processing was prepared *via* the wet chemistry method as mentioned in Chapter 3. The HAp solution was prepared by dissolving 3 mg of HAp in a litre of dimethyl sulfoxide (DMSO), (Sigma Aldrich, UK, CAS number 67-68-5) acted as the solvent. The solution was stirred at 600 rpm for 3 hours prior to supercritical processing. For each SEDS experiment, a HAp solution of 500 ml was used. The experimental work was carried out by varying a number of parameters: solvent flowrate (1 ml/min and 2 ml/min), CO_2 flowrate (20 g/min, 40 g/min and 60 g/min) and temperature (40 ^oC and 50 ^oC), as shown in Table 4.3. The operating pressure was set at 150 bar for all of the experimental

work. The nozzle diameter was 125 µm. Each SEDS experimental condition was repeated 6 times.

Temperature & Pressure	Solvent flowrate (ml/min)	$scCO_2$ flowrate (g/min)
40 °C, 150 bar	1.0	20
		40
		60
	2.0	20
		40
		60
50 °C, 150 bar	1.0	20
		40
		60
	2.0	20
		40
		60

Table 4.3 SEDS experimental conditions.

The SEDS processing rig consisted of a 500 ml vessel (Parr, Moline, USA) which was fitted with a coaxial nozzle in the head through which the HAp solution and CO_2 was introduced (refer to Fig. 4.2). CO_2 (BOC UK, CAS number 124-38-9) flowrate was regulated by the CO_2 pump using the integral software (Thar Instrument Process Suite, version 2.05). Prior to SEDS processing, the rig was heated to the desired operating temperature using the integral software. Next CO_2 was introduced to reach the fixed operating pressure of 150 bar and an automated back pressure regulator was used to maintain the pressure within the system. The CO_2 supply was kept flowing at steady state conditions through the vessel for 10 minutes

(ensuring constant and stable pressure within the system) before the HAp solution was introduced into the supercritical vessel. When the HAp solution was finished, CO_2 was kept flowing for 30 minutes in order to purge any residual solvent that might remain in the vessel. The CO_2 supply was then stopped and the supercritical processing rig was depressurised and cooled down. The particles produced were collected at the bottom of the vessel on a steel mesh filter. The waste DMSO solvent was collected by opening the cyclone valve and was disposed in a safe manner. Before disposal, the DMSO was analysed for any HAp content.

4.3 Particle characterisation techniques

The particle characterisation techniques are the same as mentioned in Chapter 3, section 3.3.

4.4 Results and discussion

This study was carried out to evaluate the potential of supercritical fluid (SCF) processing, specifically by the GAS Anti-Solvent (GAS) and Solution Enhanced Dispersion by Supercritical Fluids (SEDS) methods in producing nanoparticles of hydroxyapatite (HAp). This work is the first report in the production of HAp by SCF methods. The only other work that utilises SCF and HAp is the work of Barry [Barry et al. (2008)] who published an *in vitro* study of hydroxyapatite based photocurable polymer composites prepared by laser stereolithography and SCF extraction. The work in this thesis was carried out in order to compare HAp particles produced from the sol-gel (wet chemistry) technique and SCF methods and assessing any advantages and disadvantages among these two procedures. In addition, the potential of using the SCF technique to produce a non-viral gene vector was also evaluated. SEDS method has been shown to achieve better mixing through turbulent flow which can lead to a change in particle size when compared to those produced by GAS [Palakodaty et al. (1998)]. The particles produced from the GAS method were compared to those from the SEDS method. The characterisations undertaken were to determine the functional groups (FTIR), phase analysis (XRD), morphology (SEM) and the particle size estimations (TEM & HPPS) of the as prepared SCF processed HAp.

The FTIR analysis showed the occurrence of absorption peaks for HAp for both SCF methods, which consisted of peaks representing the phosphate groups (PO_4^{3-}) and hydroxide groups (OH^-) for all the particle samples obtained. The FTIR spectra of some of the particle samples obtained from both methods are combined in Figure 4.5 below:

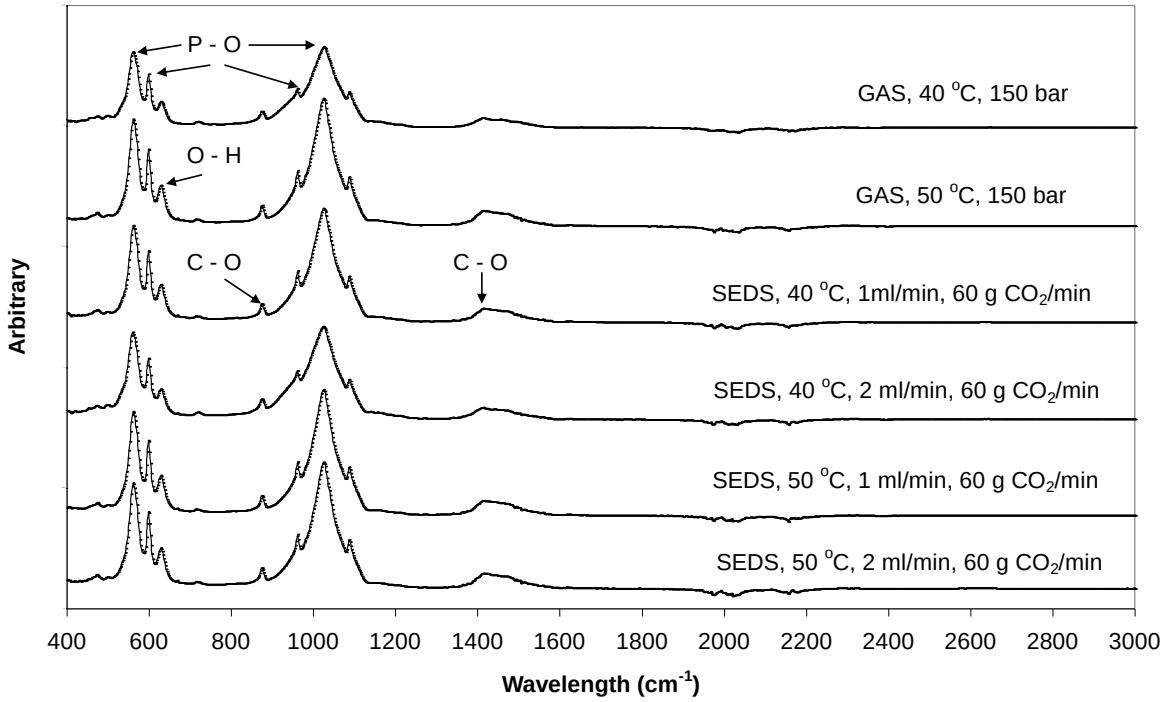

Figure 4.5 FTIR spectra of some GAS & SEDS processed HAp samples.

FTIR results indicated the presence of HAp by the bands for the P-O stretching vibration at 565 – 601 cm^{-1} and 960 – 965 cm^{-1} which corresponded to the phosphate (PO_4^{3-}) ions [Kawata et al. (2004) & Miyaji et al. (2005)]. The peaks assigned to the stretching modes of hydroxyl groups (OH^-) in hydroxyapatite were at 632 cm^{-1} and 3571 cm^{-1} [Miyaji et al. (2005), Varma & Babu (2005)]. The HAp formed by both approaches in this study is still shown to be of type B substitution (whereby carbonate ions, CO_3^{2-} have substituted some of the PO_4^{3-} ions in the apatitic structure) by the C-O peaks observed at 1418 $cm^{-1}$and 1462 cm^{-1} [Varma & Babu (2005)] as previously observed by the wet chemistry technique (refer to Fig. 4.5). The presence of type B carbonate in the apatite lattice has been shown to cause an increase in its solubility both *in vitro* and *in vivo* tests [Krajewski et al. (2005)].

In terms of the XRD analysis, the formation of hydroxyapatite is indicated by the characteristic peak occurred at $2\theta = 31.8^{o}$ as shown on Figure 4.6 [Shimbayashi et al. (1996)]. The narrow peaks on the XRD spectra indicated a high degree of crystallinity (averages of 68 %) of the hydroxyapatite crystals formed.

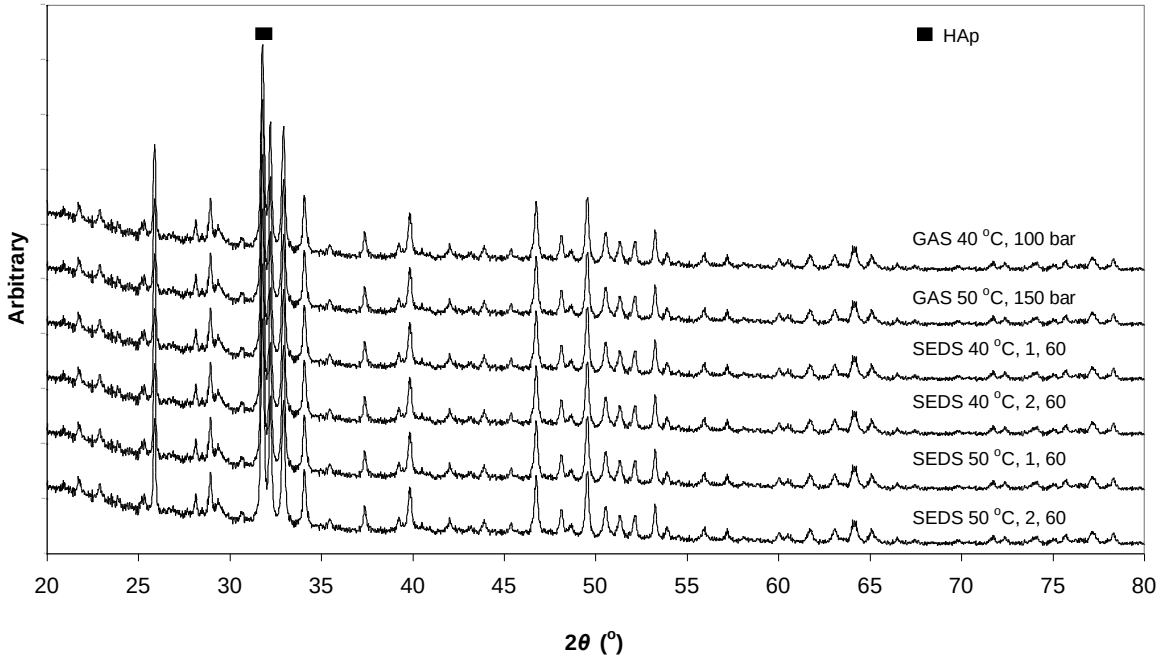

Figure 4.6 XRD patterns of some GAS & SEDS HAp samples.

In the DLS analyses, the HAp produced by the GAS technique, showed that the particle size decreased slightly at a lower temperature and also at higher pressure. As an example, for HAp produced by GAS technique at operating temperature of 50 ^{o}C and a pressure of 100 bar, particles with an average size of 177 nm were obtained. Meanwhile, at an operating temperature of 50 ^{o}C and pressure of 150 bar, particles with an average size of 173 nm were produced. Particles produced at 60 ^{o}C had an average size of 186 nm. This can be explained by the interactions between the $scCO_2$ and DMSO at specific temperatures and pressures. At lower operating temperatures for a given pressure, there is a higher solubility of CO_2 in

DMSO and expansion of DMSO will occur as reported by Lucien [Lucien et al. (2004)]. This is due to the increase in the density of CO_2 and the corresponding increase in the solubility of CO_2 in the liquid phase. Higher amount of CO_2 leads to smaller particles induced by higher supersaturation. The DLS data for the GAS technique is shown in Table 4.4.

GAS sample (Temperature ^oC, pressure, bar)	Particle size by DLS, filtered (nm)
40, 150	168 ± 5
50, 150	173 ± 3
60, 150	186 ± 4
50, 100	177 ± 5
50, 200	163 ± 6

Table 4.4 Particle sizing for HAp produced by GAS technique.

For the SEDS samples, the particle size decreased with temperature and antisolvent to solvent ratio. In respect of operating temperature, at a given solvent flowrate (1 ml/min) and antisolvent flowrate (60 g/min), the HAp particles produced at 40 ^oC have average particle sizes of 131 nm. For the same given solvent and antisolvent flowrate but at temperature of 50 ^oC, the average particle size is 141 nm. In term of antisolvent to solvent ratio, the particle size decreased with higher ratio of antisolvent to solvent. The HAp sample produced at operating conditions of temperature at 40 ^oC, with 1 ml/min of solvent flowrate and 60 g/min of antisolvent (antisolvent to solvent ratio of 60) gave particle size of 131 nm. In contrast, the HAp sample produced at operating conditions of temperature at 40 ^oC, with 2 ml/min of solvent flowrate and 60 g/min of antisolvent (antisolvent to solvent ratio of 30) gave particle size of 153 nm. This could be explained by the better mixing of the $scCO_2$ with the solvent, thus increasing the solvent extraction. More CO_2 anti-solvent within the system, leads to

faster supersaturation that forms smaller nuclei. The DLS data for the SEDS technique is shown in Table 4.5.

SEDS sample (Temperature, solvent flowrate, CO_2 flowrate)	CO_2 / solvent ratio flowrate	Particle size by DLS filtered (nm)
40, 1, 20	20	152 ± 3
40, 1, 40	40	144 ± 3
40, 1, 60	60	131 ± 4
40, 2, 20	10	167 ± 6
40, 2, 40	20	154 ± 5
40, 2, 60	30	153 ± 4
50, 1, 20	20	166 ± 5
50, 1, 40	40	149 ± 4
50, 1, 60	60	141 ± 5
50, 2, 20	10	185 ± 3
50, 2, 40	20	164 ± 4
50, 2, 60	30	159 ± 3

Table 4.5 Particle sizing for HAp produced by SEDS technique.

The DLS data showed that the particle size produced by the SEDS technique gave smaller particle size as compared to the GAS technique. As an example, the SEDS processed HAp at 40 ^{o}C and scCO_2 for a solvent ratio flowrate of 60 produced an average particle size of 131 nm, whereas the GAS technique at 40 ^{o}C, 150 bar and scCO_2 of 40 g/min, gave an average particle size of 168 nm. This would be due to the faster and better mixing of antisolvent to solvent in the SEDS technique as compared to the GAS technique which is slower.

SEM images reveal the morphology of the produced particles, which exhibit a circular appearance. The images show that the particles consist of smaller units which agglomerate into larger units when contacted with each other. Some of the SEM images for the GAS and SEDS processed HAp are shown in Figure 4.7.

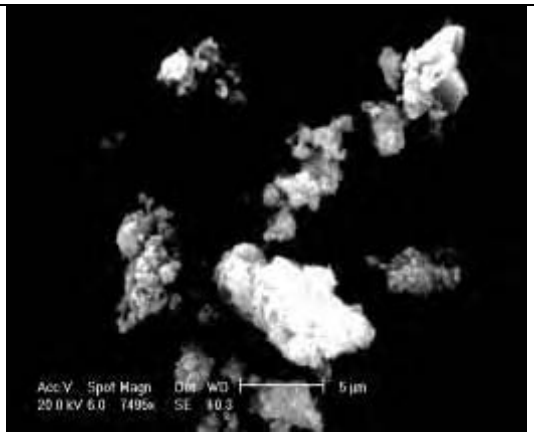

a) GAS at 40 °C and 150 bar

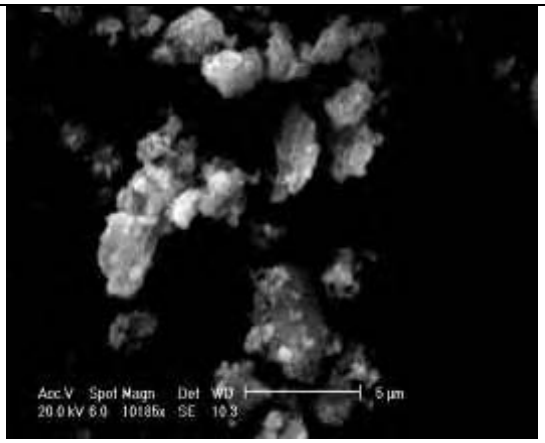

b) GAS at 50 °C and 150 bar

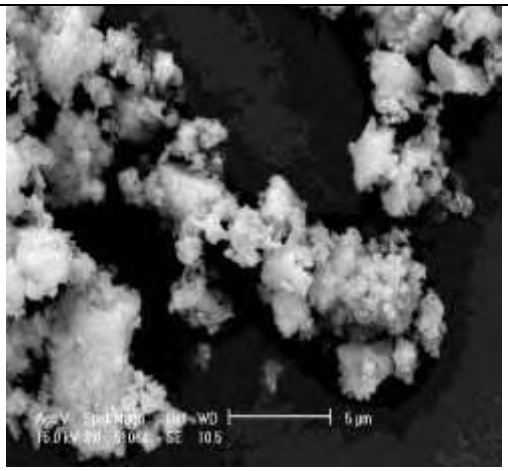

c) SEDS at 40 °C, 1 ml/min, 60 gCO_2/min

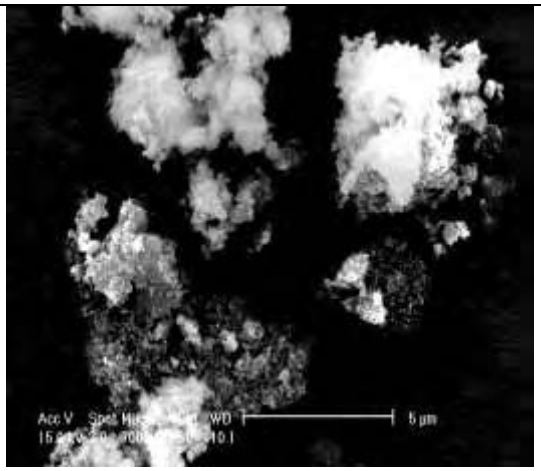

d) SEDS at 50 °C, 1 ml/min, 60 gCO_2/min

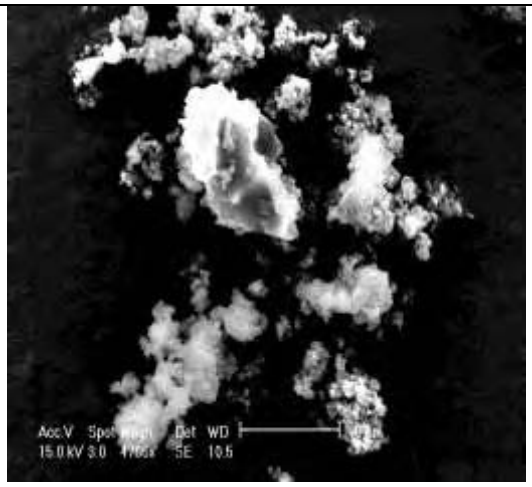

e) SEDS at 40 °C, 2 ml/min, 60 gCO_2/min

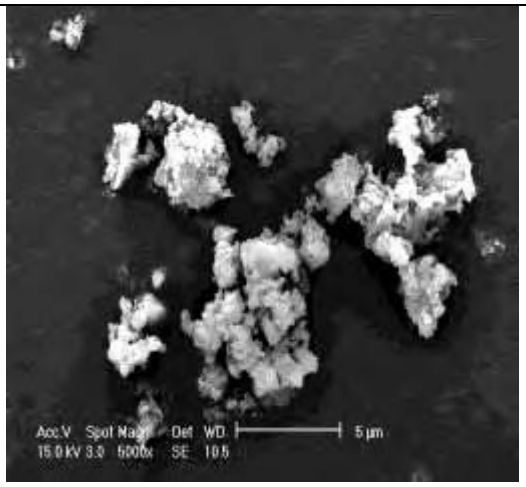

f) SEDS at 50 °C, 2 ml/min, 60 gCO_2/min

Figure 4.7 SEM images of some of the GAS and SEDS samples.

TEM is a very useful tool in estimating the particle size of nanomaterials [Ma & Liu (2009)]. From the SEDS processing, it was shown that the particle size decreased with higher ratio of CO_2 flowrate with the solvent flowrate. This regime facilitates rapid supersaturation, extracting the solvent more efficiently which leads to nucleation and subsequent production of particles [Palakodaty et. al. (1998)]. Other workers have reported that the dispersion in the jet at the nozzle outlet facilitates rapid (< 1 second) formation of particles of small size [Hanna (1994)]. This study also showed that HAp can be recrystallised by GAS and SEDS processing with particles size decreased in respect of the processing conditions of temperature, pressure and scCO_2 to solvent flowrate.

(a) GAS at 40 °C and 150 bar

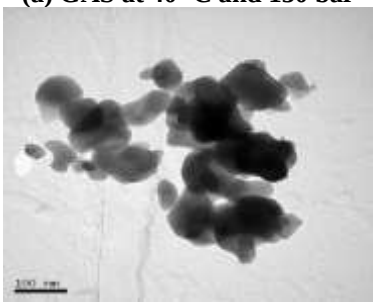

DLS: 168 ± 5 nm

(b) GAS at 60 °C and 150 bar

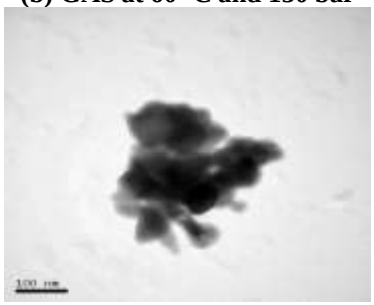

DLS: 186 ± 4 nm

(c) GAS at 50 °C and 100 bar

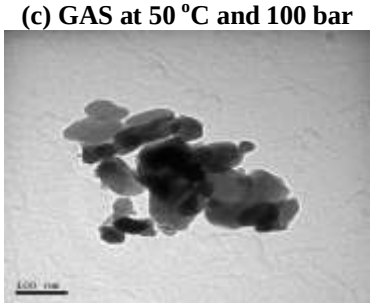

DLS: 177 ± 5 nm

(d) GAS at 50 °C and 200 bar

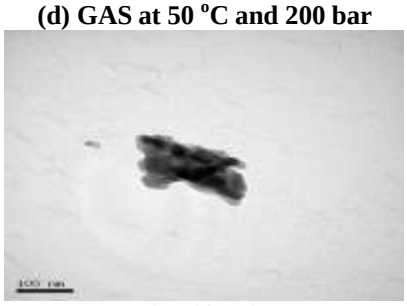

DLS: 163 ± 6 nm

(e) SEDS at 40 °C, 1 ml/min and 60 g/min of CO_2

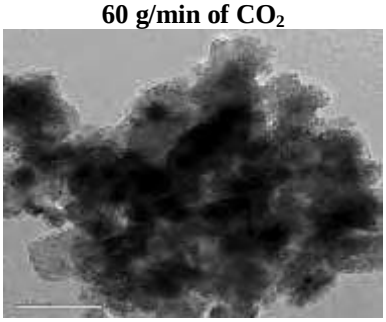

DLS: 131 ± 4 nm

(f) SEDS at 40 °C, 2 ml/min and 60 g/min of CO_2

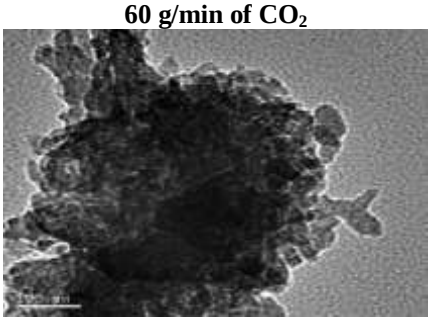

DLS:153 ± 4 nm

(g) SEDS at 50 °C, 1 ml/min and 60 g/min of CO_2

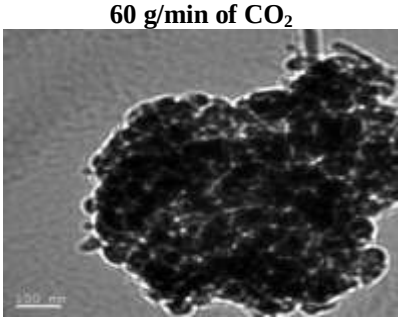

DLS:141 ± 5 nm

(h) SEDS at 50 °C, 2 ml/min and 60 g/min of CO_2

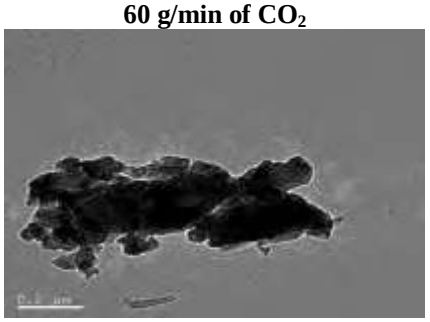

DLS:159 ± 3 nm

Figure 4.8 TEM images of some of the GAS and SEDS samples.

4.5 Conclusions

In this study, HAp particles were recrystallised by the GAS and SEDS supercritical processing techniques. The HAp samples produced by both techniques gave similar characterisations in term of FTIR, XRD and SEM analyses. They only differ in the particle size. The particle size decreased with respect to the operating conditions of temperature, pressure and antisolvent to solvent ratio. Overall, SEDS technique yield smaller particle size as compared to GAS technique.

4.6 References:

Adschiri, T. Arai, K. 2002. Hydrothermal synthesis of metal oxide nanoparticles under supercritical conditions, In: Ya-Ping Sun (Ed.), Supercritical Fluid Technology in Material Science and Engineering, Marcel Dekker Inc., New York, pp. 311 - 325.

Barry, J .J. A. Evseev, A. V. Markov, M. A. Upton, C. E. Scotchford, C. A. Popov, V. K. Howdle, S. M. 2008. In vitro study of hydroxyapatite-based photocurable polymer composites prepared by laser stereolithography and supercritical fluid extraction, Acta Biomaterialia 4, Issue 6: 1603 – 1610.

Byrappa, K. Ohara, S. Adschiri, T. 2008. Nanoparticles synthesis using supercritical fluid technology – towards biomedical applications, Advanced Drug Delivery Review 60: 299 – 327.

Chattopadhyay, P. Gupta, R. B. 2002. Supercritical CO_2 based production of magnetically responsive micro- and nanoparticles for drug targeting, Ind. Eng. Chem. Res. 41: 6049 – 6058.

DeSimone, J. M. 2002. Practical approaches to green solvents, Science 297: 799 – 803.

Epple, M. Sokolova, V. 2008. Inorganic Nanoparticles as Carriers of Nucleic Acids into Cells, Angew. Chem. Int. Ed. 47: 1382 – 1395.

Gallagher, P. M. Coffey, M. P. Krukonis, V. J. Klasutis, N. 1989. In Supercritical Fluid science and Technology. Johnston, K. P. Penniger, J. M. L. Eds. ACS Symposium Series 406, American Chemical Society, Washington DC.

Gallagher, P. M. Coffey, M. P. Krukonis, V. J. 1992. Gas Anti-Solvent Recrystallisation of a Difficult to Comminute Explosive. J. of Supercritical Fluids 5: 130 – 142.

Goodarzi, M. Duchowicz, P. R. Freitas, M. P. Fernandez, F. M. 2010. Prediction of the Hildebrand parameter of various solvents using linear and nonlinear approaches. Fluid Phase Equilibria 293: 130 – 136.

Hanna, M. York, P. 1994. Patent WO 95/0122 1.

Hay, J. N. Khan, A. 2002. Environmentally friendly coatings using carbon dioxide as the carrier medium, J. Mater. Sci. 37: 4743 – 4752.

Jenkins, R. Synder, R. L. 1996. Introduction to X-ray Powder Diffractometry, John Wiley and Sons, New York.

Kawata, M. Uchida, H. Itatani, K. Okada, I. Koda, S. Aizawa, M. 2004. Development of porous ceramics with well-controlled porosites and pore sizes from apatite fibers and their evaluations, J. Mater. Sci. Mater. Med. 817 – 823.

Kenneth, T. D. Artie, M. 2003. Dimethylsulfoxide (DMSO) solvent formulation for exterior aircraft coatings removal. 2003 Aerospace Coatings Removal and Coatings Conference. 1 – 10.

Krajewski, A. Mazzocchi, M. Buldini, P. L. Ravaglioli, A. Tinti, Taddei, P. Fagnano, C. 2005. Synthesis of carbonated hydroxyapatites: efficiency of the substitution and critical evaluation of analytical methods, Journal of Molecular Structure. 744: 221 – 228.

Lucien, F. P. Rajasingam, R. Lioe, L. Tuan Pham, Q. 2004. Solubility of carbon dioxide in dimethylsulfoxide and *N*-methyl-2-pyrrolidone at elevated pressure. Journal of Supercritical Fluids 31: 227 – 234.

Ma, G. Liu, X. Y. 2009. Hydroxyapatite: Hexagonal or Monoclinic?, Crystal Growth & Design Vol. 9, No. 7: 2991 – 2994.

Mishima, K. 2008. Biodegradable particle formation for drug and gene delivery using supercritical fluid and dense gas, Advanced Drug Delivery Reviews 60: 411 – 432.

Miyaji, F. Kono, Y. Suyama, Y. 2005. Formation and structure of zinc-substituted calcium hydroxyapatite, Mater. Res. Bull. 40: 209 – 213.

Palakodaty, S. York, P. Pritchard, J. 1998. Supercritical fluid processing of materials from aquoes solutions: the application of SEDS to lactose as a model substance, Pharm. Res. 15: 1835 – 1843.

Palakodaty, S. Sloan, R. Kordikowski, A. 2002. Pharmaceutical and biological materials processing with supercritical fluids, In: Ya-Ping Sun (Ed.), Supercritical Fluid Technology in Material Science and Engineering, Marcel Dekker Inc., New York, pp. 439 – 490.

Pons, M. N. Vivier, H. Delcour, V. Authelin, J. R. Pailleres-Hubert, L. 2002. Morphological analysis of pharmaceutical powders, Powder Tech. 128: 276 – 286.

Shimbayashi, S. Hashimoto, N. Kawamura, H. Uno, T. 1996. Mineral Scale Formation and Inhibition, In: Amjad, Z (Ed.), Plenum Press: New York, 14 – 15.

Tservistas, M. Levy, M. S. Lo-Yim, M. Y .A. O'Kennedy, R .D. York, P. Humphrey, G. O. Hoare, M. 2001. The formation of Plasmid DNA loaded Pharmaceutical Powders Using Supercritical Fluid Technology, John Wiley & Sons, Inc.

Varma, H. Babu, S. S. 2005. Synthesis of calcium phosphate bioceramics by citrate gel pyrolysis method, Ceram. Int. 31: 109 – 114.

5.0 A systematic investigation of Calcium Phosphates (CaP) precipitation processes

5.1 Introduction

A systematic study on the formation of calcium phosphates by varying the calcium to phosphorus ratio is reported in this chapter. The calcium precursor used is calcium nitrate tetrahydrate, $Ca(NO_3)_2.4H_2O$, the same calcium precursor as used in the sol-gel method and supercritical fluid (SCF) work mentioned in Chapter 3 and 4. Meanwhile, the phosphate precursor is diammonium phosphate, $(NH_4)_2HPO_4$, substituting phosphorus pentoxide (P_2O_5) as the phosphate precursor. This new calcium phosphate investigation was carried out by two methods, the wet chemistry (direct precipitation) and supercritical anti-solvent (SEDS) methods.

5.2 Materials and methods

5.2.1 Materials

Calcium nitrate tetrahydrate, $Ca(NO_3)_2.4H_2O$ [CAS number 13477-34-4], diammonium phosphate $(NH_4)_2HPO_4$ [CAS number 7783-28-0], concentrated aqueous ammonia (NH_4OH) [CAS number 7664-41-7] and dimethyl sulfoxide, DMSO [CAS number 67-68-5, 99.5% purity and 400 ppm residual water)] were obtained from Sigma-Aldrich UK and were used without further purification. The CO_2 for SEDS processing [CAS number 124-38-9] was supplied by BOC UK (99% purity).

5.2.2 Direct precipitation method

The direct precipitation method was carried out according to the procedure reported by Jarcho et al. (1979). The molar ratio studies conducted for the Ca/P were 1.00:2.50, 1.50:2.00, 1.50:1.50, 2.00:1.50, 1.67:1.00 and 2.50:1.00. This study was based upon the main Ca/P ionic ratios mentioned on Table 2.1. As an example, for the Ca/P molar ratio of 1.50:1.50, 150 mM each of calcium nitrate tetrahydrate and diammonium phosphate precursors were dissolved in 100 ml of double distilled water. The pH of both solutions was corrected between 11 and 12 by adding concentrated aqueous ammonia (35% concentration). The calcium nitrate solution was vigorously stirred at 1200 rpm at a temperature of 20 ^{o}C and then the diammonium phosphate solution was added dropwise for a duration of 30 minutes (dropwise flowrate of 3.33 ml/min). The reaction mixture was stirred for 12 hours and then centrifuged at 2000 rpm for 10 minutes, the supernatant decanted and the precipitate was resuspended in double distilled water. This washing procedure was repeated a further two times. The centrifuged precipitate was then dried at 80 ^{o}C for 24 hours and ground with a pestle and mortar.

5.2.3 SEDS method

The SEDS method was carried out according to the procedure described earlier in Chapter 3. The molar ratios studied for this method were based upon the flowrate of the calcium and phosphate precursors dissolved in DMSO into the reaction vessel, *via* two separate nozzles. An additional peristaltic pump (Thar Tech. Inc.) was used to deliver the calcium precursor solution into the reaction vessel. The flowrates studied were 1) 0.50 ml/min of calcium precursor : 1.50 ml/min of phosphate precursor (molar ratio of 0.33), 2) 1.00 ml/min of calcium precursor : 1.00 ml/min of phosphate precursor (molar ratio of 1.00) and 3) 1.50 ml/min of calcium precursor : 0.50 ml/min of phosphate precursor (molar ratio of 3.00) at fixed concentrations of 100 mM for both precursors. This study was based upon the main Ca/P ionic ratios mentioned on Table 2.1, but fewer Ca/P molar ratios were studied compared to the direct precipitation method due to the limitation of the peristaltic pump used for introducing the calcium precursor solution into the reaction vessel. The SEDS processing conditions were set at 50 ^{o}C and 150 bar for all of the experimental work. These conditions were chosen as CO_2 has high solubility (0.30 mole fraction) and volume expansion (50%) in DMSO. The CO_2 supply into the reaction vessel was maintained at 60 g/min which provided a high antisolvent to solvent ratio within the system. These conditions produced smaller HAp particles as observed in Chapter 4. Each molar ratio processed by SEDS was repeated 6 times. The results were reproducible and the experimental data is presented in Appendix for Chapter 5.

5.2.4 Particle characterisation techniques

Particle characterisation techniques undertaken were similar to those mentioned in Chapter 3 and 4, namely X-ray Diffraction (XRD) for phase analysis, FTIR analysis for determining the functional groups, Dynamic Light Scattering (DLS) and Transmission Electron Microscope (TEM) and Scanning Electron Microscope (SEM) for particle size estimation and particle morphology.

5.3 Results and discussion

5.3.1 Effect of molar ratios on the precipitates collected

5.3.1.1 Direct precipitation method

The molar ratio studies conducted for the direct precipitation method were at the Ca/P ratios as shown in Table 5.1 below:

Ca/P precursor concentration (mM/mM)	Ca/P ratio
100/250	0.40
150/200	0.75
150/150	1.00
200/150	1.33
167/100	1.67
250/100	2.50

Table 5.1 Ca/P molar ratio studied for the direct precipitation method.

The XRD patterns for Ca/P ratios 2.50, 1.67 and 1.33 showed the occurrence of dicalcium phosphate dihydrate (DCPD) phase, otherwise known as brushite, due to the most intense peak occurring at 20.9° 2θ and other corresponding peaks at 29.2°, 30.5°, 31.3°, 34.2°, 34.4°, 37.1°, 41.6°, 42.0°, 43.4°, 50.2°, and 59.5°. The XRD patterns for Ca/P ratios of 2.50, 1.67 and 1.33 are shown in Figure 5.1 below:

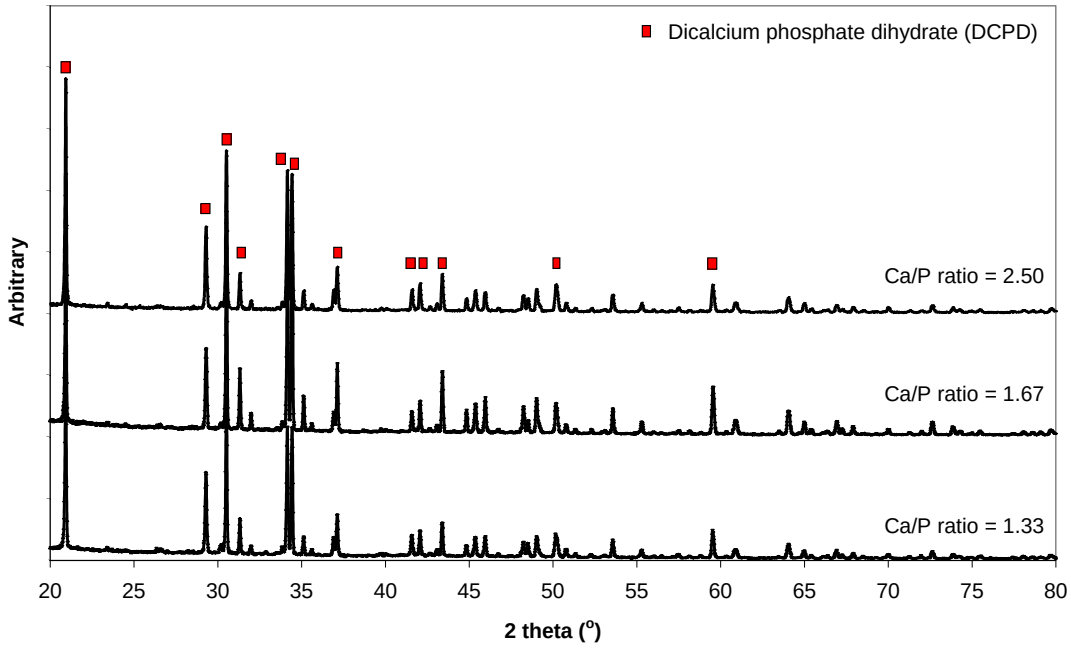

Figure 5.1 XRD patterns of the precipitates for the Ca/P ratios of 2.50, 1.67 and 1.33.

The XRD patterns for the Ca/P ratios of 1.00, 0.75 and 0.40 are shown in Figure 5.2. The Ca/P ratios of 1.00 and 0.75 also showed the occurrence of the dicalcium phosphate dihydrate (DCPD)/brushite phase. For the Ca/P ratio of 0.40, the phase determination from its XRD peaks is unclear. This maybe due to the low concentrations of both precursors used, which induces incomplete reaction as a result of a low pH (5.58) within the formation process.

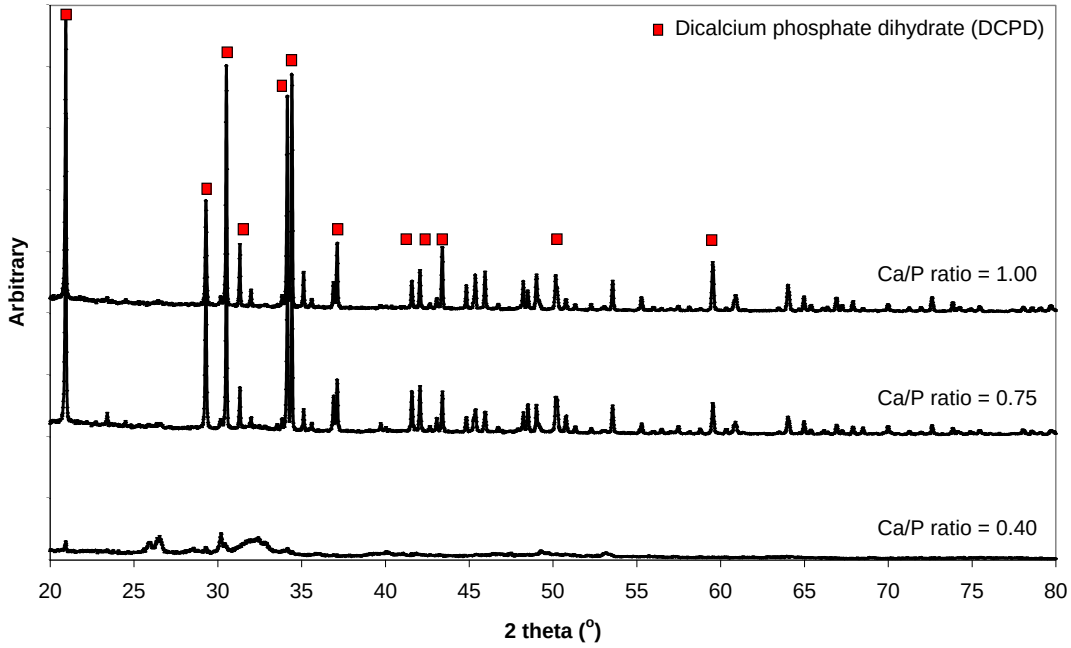

Figure 5.2 XRD patterns of the precipitates for the Ca/P ratios of 1.00, 0.75 and 0.40.

The FTIR spectra revealed that for the Ca/P ratios of 2.50, 1.67, 1.33, 1.00 and 0.75 have similar absorbance patterns, due to their phase identified as brushite from the XRD analysis. The bands at 526 and 577 cm^{-1} correspond to the medium intensity for P-O bending. Meanwhile, the bands at 660 and 790 correspond to the medium intensity for OH out of plane bending. Strong intensities for P-O (H) stretching are observed for the 875 and 985 bands. The 1060 and 1135 bands correspond to the

strong intensity for PO stretching. The 1217 band corresponds to strong intensity for motion of hydroxyl group and lastly, the 1652 band corresponds to strong intensity for inplane bending of water molecule [Petrov et al. (1967), Kawata et al. (2004) and Mijaya et al. (2005)]. For the Ca/P ratio of 0.40, the peaks assigned to the phosphate group are observed to be much broader, indicating the excess phosphate ions in the precipitates as compared to other Ca/P ratios. The FTIR spectra for the Ca/P ratios of 2.50, 1.67, 1.33, 1.00, 0.75 and 0.40 are shown in Figure 5.3.

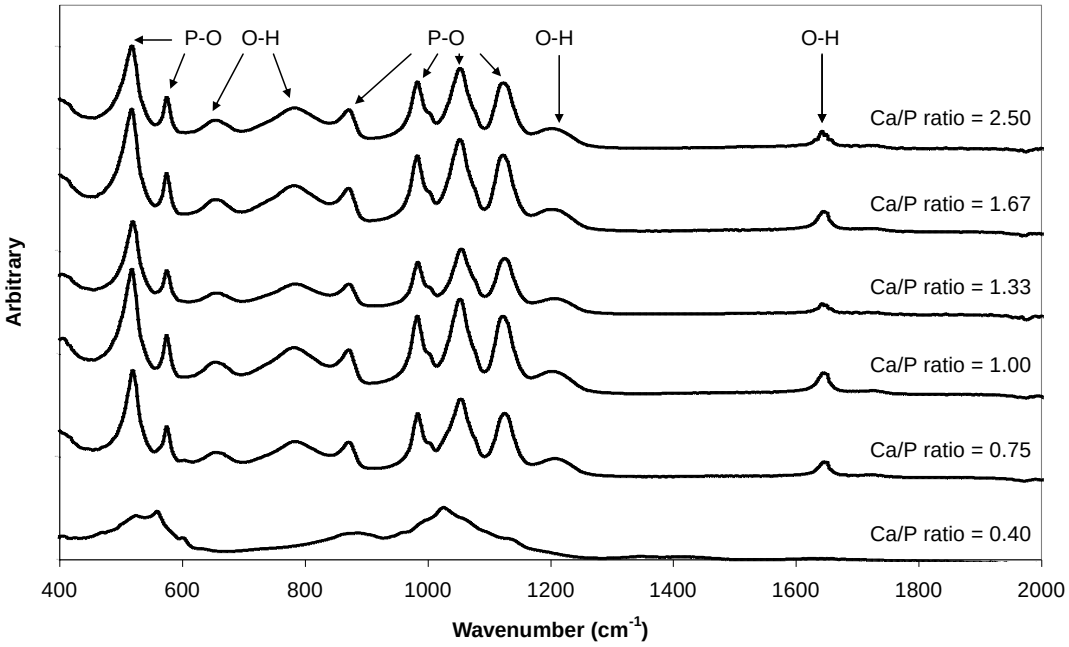

Figure 5.3 FTIR spectra for the precipitates from the direct precipitation method for Ca/P ratios of 2.50, 1.67, 1.33, 1.00, 0.75 and 0.40.

5.3.1.2 SEDS method

The Ca/P precursor flowrates investigated in the SEDS experiments are shown in Table 5.2 below:

Ca/P precursor flowrate (ml/ml per min, at fixed 100mM concentration for each precursor)	Ca/P ratio
1.50/0.50	3.00
1.00/1.00	1.00
0.50/1.50	0.33

Table 5.2 Ca/P molar ratios studied for the SEDS method.

Fewer Ca/P molar ratios were studied compared to the direct precipitation method due to the limitation of the peristaltic pump used for introducing the calcium precursor solution into the reaction vessel. The XRD patterns for the Ca/P ratios of 3.00 and 1.00 showed the occurrence of dicalcium phosphate anhydrous (DCPA) phase, otherwise known as monetite by the most intense peak occurring at 30.3^{o} 2θ and other corresponding peaks at 26.5^{o}, 32.5^{o}, 33.0^{o}, 35.9^{o}, 47.5^{o}, 49.3^{o} and 53.1^{o}. The phase for the Ca/P ratio of 0.33 might be monocalcium phosphate anhydrous, MCPA which has intense peaks at 26.6^{o}, 29.4^{o}, 30.2^{o} and 39.0^{o}. The XRD patterns for the Ca/P ratios of 3.00, 1.00 and 0.33 are shown in Figure 5.4.

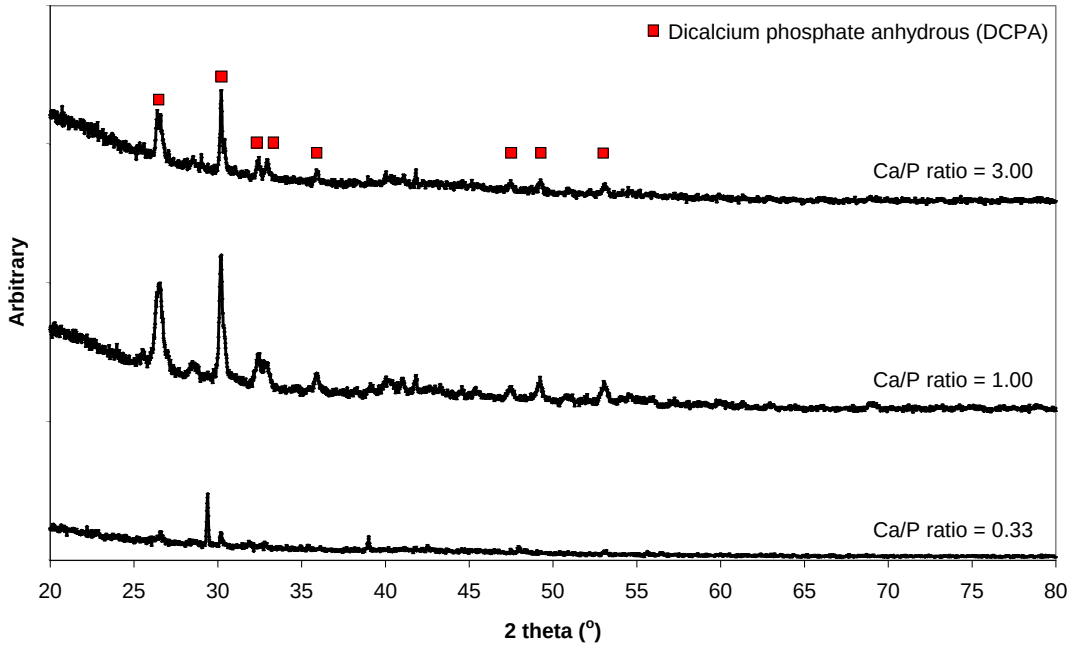

Figure 5.4 XRD patterns of the precipitates from the SEDS method for Ca/P ratios of 3.00, 1.00 and 0.33.

The FTIR spectra for the Ca/P ratios of 3.00 and 1.00 showed the presence of medium intensity for P-O bending for 526 cm^{-1} band. The 750 and 825 cm^{-1} band correspond to medium intensity for OH out of plane bending. Meanwhile, the 960 cm^{-1} band corresponds to strong intensity for P-O (H) stretching and the 1008 and 1060 cm^{-1} band correspond for strong intensities for PO stretching. The presence of carbonate (CO_3^{2-}) was identified by the broad peak at 1418 - 1462 cm^{-1}, which is not seen in the FTIR spectra of the direct precipitation method (see Figure 5.3). Lastly, the 1652 cm^{-1} band correspond to strong intensity for inplane bending of water molecule [Petrov et al. (1967), Kawata et al. (2004) and Mijaya et al. (2005)]. The FTIR spectra for the Ca/P ratios of 3.00, 1.00, and 0.33 are shown in Figure 5.5.

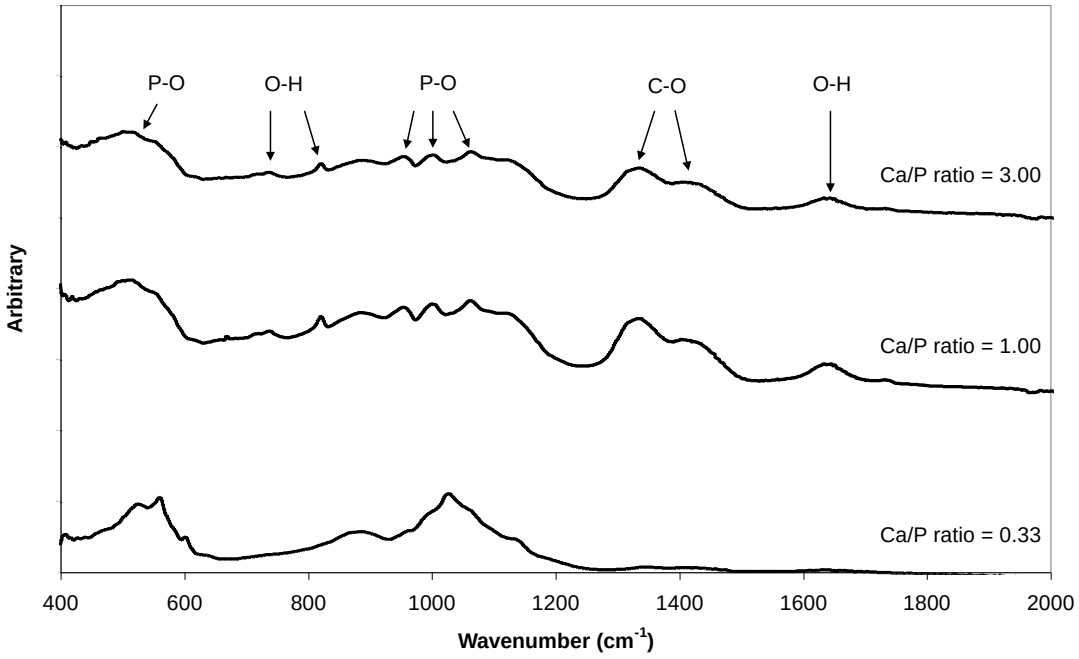

Figure 5.5 FTIR spectra for the precipitates produced by the SEDS method for Ca/P ratios of 3.00, 1.00 and 0.33.

5.3.1.3 Ca/P phase formation

Precipitation of solids from a homogeneous solution involves generation of supersaturation followed by nucleation and crystal growth. Aqueous calcium phosphate solution comprises of many different ions. The composition of these ions depends on the solution pH. The generation of supersaturation is highly dependent on the calcium and phosphorus concentration, the pH and temperature, and in the case of the SEDS method, pressure.

Brushite (dicalcium phosphate dehydrate, DCPD) was the only precipitated phase in the majority of the direct precipitation experiments, except for the experiment with a Ca/P ratio of 0.40, which did not show the intense peaks corresponding to the brushite

phase. This is in agreement with the identification of brushite phase from the literature [Boistelle and Lopez-Velero (1990), Elliot (1994), Madsen and Christaensson (1991), Ferreira et al. (20053), Marshall and Nancollas (1969), Abbona et al. (1998) and Wu and Nancollas (1998)]. The formation of brushite at a pH lower than 6.5 has been reported by numerous investigators [Boistelle and Lopez-Velero (1990), Elliot (1994), Madsen and Christaensson (1991), Faffeira et al. (2005), Marshall and Nancollas (1969), Abbona et al. (1998)]. Boistelle and Lopez-Valero (1990) and Abbona et al. (1998) reported that below pH 6.5, brushite is the dominant phase, whereas, above pH 6.5, formation of amorphous calcium phosphate (ACP) and octacalcium phosphate (OCP) is more likely. On the other hand, Wu and Nancollas (1998) claimed that although brushite and octacalcium phosphate readily precipitate from solution, they are thermodynamically metastable with respect to hydroxyapatite, HAp, and serve as a precursor phase. It has been reported that the kinetic coefficients of OCP and HAp are smaller than that of DCPD by 10 and 18 orders of magnitude at pH 6.5 [Boistelle & Lopez-Velero (1990)]. Even though the initial pH of the calcium and phosphorus precursor solution were brought between 11 and 12, the pH decreased during the precipitation process due to the presence of water in the solutions (200 ml of distilled water was used for each precipitation sample) and the slow absorption of carbon dioxide (CO_2) from the environment. This in turn would have lead to the formation of carbonic acid within the reaction solution, which made the solution acidic (pH 6.0).

Furthermore, as the concentration of calcium and phosphorus was increased in the reaction vessel (beaker), the nucleation occurred at a lower pH. Even for the same calcium concentration, the nucleation pH was lower for a higher phosphate concentration. The following equilibrium takes place during the precipitation process:

$$H_2PO_4^-H^+ = HPO_4^{2-} + 2H^+,$$

$$Ca^{2+} + H_2PO_4^- = CaH_2PO_4^+,$$

$$Ca^{2+} + HPO_4^{2-} = CaHPO_4.$$

The consumption of phosphate ion in the formation and growth of brushite would decrease the pH of the solution because of the release of the hydrogen ions from $H_2PO_4^{2-}$ dissociation. The higher the initial reagent concentration, the higher was the concentration of the remaining acid and the lower was the nucleation pH [Christoffersen et al. (1990), Boistelle & Lopez-Velero (1990), Hlabse & Walton (1965)] (the pH values range was between 5.58 and 6.55 for the direct precipitation for CaP ratios of 0.40 to 2.50).

The formation of brushite (direct precipitation method) and monetite (SEDS method) phases are observed in the present condition of the study. The order of their precipitation from a supersaturated solution is not only governed by the thermodynamic solubility product, but also by kinetic factors. The precipitated phase may undergo solution mediated transformation to more stable phases [Abbona et al. (1986)].

At room temperature, the occurrence of mainly three crystalline phases has been reported in the literature [Boistelle and Lopez-Velero (1990)]. In order of decreasing

solubility in water (H_2O), they are brushite, octacalcium phosphate and hydroxyapatite. In addition, amorphous calcium phosphate also precipites at room temperature. Supersaturation needed for the formation of hydroxyapatite (HAp), octacalcium phosphate (OCP) and brushite (DCPD) are in the order of HAp > OCP > DCPD. Brushite nucleates more easily than OCP and HAp at low pH (in the pH range of 5 to 6) [Boistelle and Lopez-Velero (1990)]. Therefore the formation and growth of brushite is favoured in the present conditions of the study.

Meanwhile, for the SEDS method, monetite (dicalcium phosphate anhydrous, DCPA) was the only precipitated phase observed for two of the CaP ratios, which are ratios of 3.00 and 1.00. Monetite is the anhydrous form of brushite (DCPD) and it is less soluble than DCPD due to the absence of water inclusions. The formation of monetite in these conditions was due to the lower pH as a result of a CO_2 rich environment within the system and also the use of DMSO instead of distilled water in dissolving the precursors. The residual water in the DMSO is 400 ppm (Sigma Aldrich, UK, CAS number 67-68-5, 99.5% purity), thus even with this small amount of water, the formation of carbonic acid is possible inside a CO_2 rich environment.

5.3.2 Effect of molar ratios on particle size and morphology

5.3.2.1 Direct precipitation method

A summary table containing the data for SEM, TEM and DLS for the direct precipitation method is shown in Table 5.3. The brushite crystals produced had plate-like morphology as observed by SEM. This morphology is in agreement with the morphology observed by Arifuzzaman & Rohani (2004). TEM images for each of the Ca/P ratios showed that the primary crystals are within the nanosized range (approximately 50 – 80 nm). Since all of the wet precipitation samples are identified as brushite, except for the Ca/P ratio of 0.40, they have similar characteristics in terms of their morphologies and particle sizes. The particle size data showed that the mean crystal sizes of the agglomerates are insensitive to the variation of initial calcium and phosphorus concentration.

The particle sizes reported here are the filtered precipitation samples prior to the DLS measurements. In the unfiltered samples, the particles rapidly aggregated to form agglomerates while the filtered samples, the particles formed stable agglomerates. The filtered samples resulted in smaller particles but the sizes still implied that aggregation of the primary particles had occurred.

Ca/P ratio	SEM (scalebar = 20 µm)	TEM	DLS, filtered (nm)
0.40	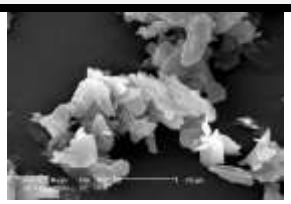		216 ± 2
0.75		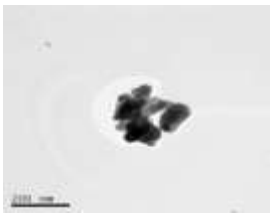	214 ± 3
1.00	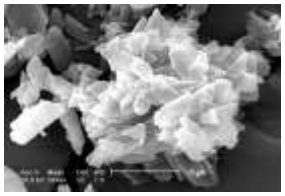	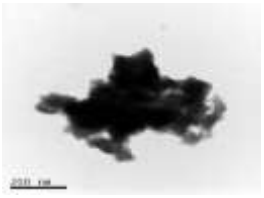	215 ± 4
1.33	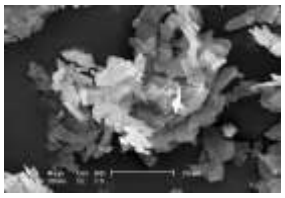	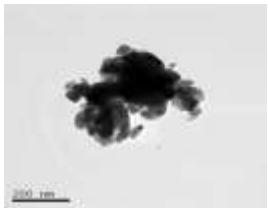	214 ± 2
1.67			218 ± 6
2.50	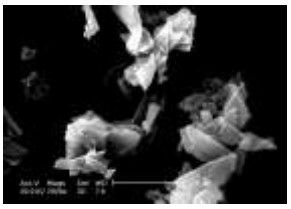	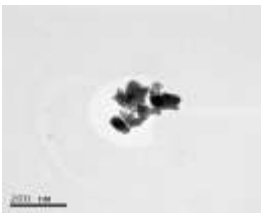	219 ± 7

Table 5.3 SEM, TEM & DLS particle size data obtained from the direct precipitation method.

5.3.2.2 SEDS method

A summarised table containing the data for SEM, TEM and DLS for the SEDS method is shown in Table 5.4. The monetite crystals produced had grain-like morphology as investigated by SEM (agglomerates with sizes approximately 50 µm). The TEM images showed the fractured particles (particle sizes approximately between 50 – 80 nm) from the larger particles shown in the SEM images.

Ca/P ratio	SEM (scalebar = 20 µm)	TEM	DLS, filtered (nm)
0.33	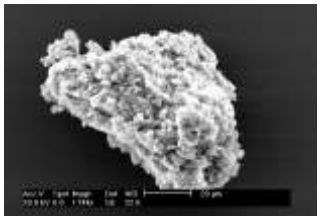	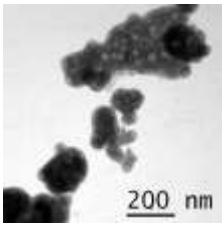	218 ± 3
1.00	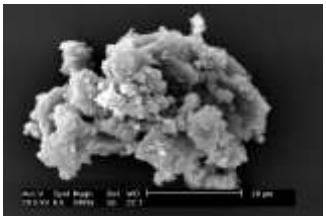	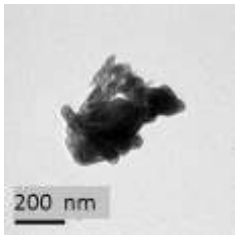	215 ± 6
3.00	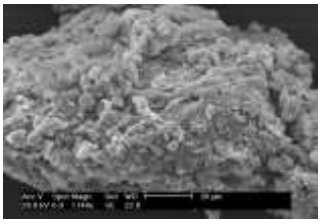	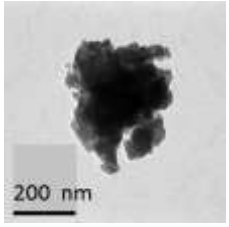	217 ± 5

Table 5.4 SEM, TEM and DLS particle size data obtained from the SEDS method.

5.4 Conclusions

The particles produced by the direct precipitation method were identified to be mostly the brushite phase. Meanwhile, the particles produced by the SEDS method were observed to be the monetite phase. The pH of the reaction solution during the precipitation process played an important role in forming these phases of CaP. It was noted that the pH decreased during the direct precipitation process due to the presence of carbonic acid by the mixture of water from the precursor solution and CO_2 from the environment, which made the reaction solution acidic. The decrease in the pH was also due to the release of the hydrogen ions from the $H_2PO_4^{2-}$ dissociation. A further investigation is to control the pH of the reaction solution throughout the precipitation process.

It was the similar case for the SEDS method, where the CO_2 rich environment within the system has lowered the pH during the precipitation process due to the minute amount of residual water in the DMSO (400 ppm) which may have turned it acidic due to the formation of carbonic acid. DMSO was used to dissolve the precursors due to its solubility with supercritical CO_2 and produced monetite (DCPA), the anhydrous form of brushite (DCPD).

5.5 References:

Abbona, F. Lundager-Madsen, H. E. Boistelle, R. 1986. The initial phases of calcium and magnesium phosphates precipitated from solutions of high medium concentrations, Journal of Crystal Growth, 74: 581 – 590.

Abbona, F. Christiansson, F. Angela, M. F. Lundager-Madsen, H. E. 1998. Crystal habit and growth conditions of brushite, $CaHPO_4.2H_2O$, Journal of Crystal Growth, 131: 331 – 346.

Arifuzzaman, S. M. Rohani, S. 2004. Experimental study of brushite precipitation, Journal of Crystal Growth, 267: 624 – 634.

Boistelle, R. Lopez-Velero, I. 1990. Growth units and nucleation: The case of calcium phosphates, Journal of Crystal Growth, 102: 609 – 617.

Christoffersen, M. R. Christoffersen, J. Kibalczyc, W. 1990. Apparent solubilities of two amorphous calcium phosphates and of octacalcium phosphate in the temperature range 30 – 42 ^oC, Journal of Crystal Growth, 106: 349 – 354.

Elliot, J. C. 1994. Structure and Chemistry of the Apatites and Other Calcium Orthophosphates, Elsevier, Amsterdam.

Ferreira, A. Oliveira, C. Rocha, F. 2003. The different phases in the precipitation of dicalcium phosphate dihydrate, Journal of Crystal Growth, 252: 599 – 611.

Hlabse, T. Walton, A. G. 1965. The nucleation of calcium phosphate from solution, Analytica Chimica Acta, 33: 373 – 377.

Jarcho, M. Salsbury, L. Thomas, M. B. Doremus, R. H. 1979. Synthesis and fabrication of beta-tricalcium phosphate (whitlockite) ceramics for potential prosthetic applications, Journal of Materials Science, 14: 142 – 150.

Kawata, M. Uchida, H. Itatani, K. Okada, I. Koda, S. M. Aizawa, M. 2004. Development of porous ceramics with well-control porosites and pore sizes from apatite fibers and their evaluations, Journal of Material Science. Med., 817 – 823.

Lundager-Madsen, H. E. Christaensson, F. 1991. precipitation of calcium phosphate at 40 ^oC from neutral solution, Journal of Crystal Growth 114: 613 – 618.

Miyaji, F. Kono, Y. Suyama, Y. 2005. Formation and structure of zinc-substituted calcium hydroxyapatite, Materials Reserach Bulletin 40: 209 – 213.

Marshall, R. W. Nancollas, G. H. 1969. The kinetics of crystal growth of dicalcium phosphate dihydrate, Journal of Physical Chemistry, 73 (11): 3838 – 3833.

Petrov, I. Soptrajanov, B. Fuson, N. Lawson, J. R. 1967. Spectrochim Acta 23A: 2637.

Wu, W. Nancollas, G. H. 1998. The dissolution and growth of sparingly soluble inorganic salts: A kinetic and surface energy approach, Pure Applied Chemistry, 70 (10): 1867 – 1872.

6.0 Attachment of calcium phosphate particles prepared by sol-gel, supercritical anti-solvent and new calcium phosphate route with plasmid DNA (pDNA) and *in-vitro* transfection studies of CaP-pDNA post co-precipitation complexes

6.1 Introduction

The technique of calcium phosphate co-precipitation with plasmid DNA (pDNA) for *in vitro* transfection is used as a routine laboratory procedure [James et al. (1987)]. This method relies heavily on the fact that divalent metal cations, such as Ca^{2+}, Mg^{2+}, Mn^{2+}, and Ba^{2+} can form ionic complexes with the helical phosphates of DNA [Bloomfield (1997) and Truong-Le (1999)]. Calcium phosphate can therefore form complexes with the nucleic acid backbone and thus may impart a stabilising function to certain DNA structures. DNA is reported to bind with HAp particles by the strong affinity between the phosphate groups of the DNA, which are negatively charged and the calcium ions of HAp [Okazaki et al. (2001)]. Calcium has a small hydrodynamic radius and therefore a high charge-to-surface area [Kulkarni et al. (2006)]. The complexes can then be carried across cell membrane via ion channel mediated endocytosis [Truong-Le (1999)]. The specificity of calcium over other divalent metals is because it not only effectively condenses DNA, but does it in such a way that it is still functional following successful delivery to the cell nucleus, which is a result of Coulombic interactions [Walters & Welsh (1999)]. Calcium phosphate has been used to effectively transfect bone tissue *in vivo* recently [Kuroda et al. (2005) & Endo et al. (2006)].

In-vitro transfection studies of calcium phosphate – plasmid DNA (CaP-pDNA) post co-precipitation on two cell cultures, the NIH/3T3 fibroblasts and MC3T3 osteoblasts is reported in this chapter. The calcium phosphates that formed the complexes were from the particles produced by the sol-gel method (Chapter 3), supercritical fluid, SCF (Chapter 4) and new calcium phosphate precipitation process route (Chapter 5). This transfection investigation was carried out as to evaluate the effectiveness of the CaP-pDNA complexes as pDNA carrier into the cells.

6.2 Experimental methods

6.2.1 pDNA attachment

6.2.1.1 *In-situ* co-precipitation attachment by Gas Anti-solvent (GAS) and Solution Enhanced Dispersion by Supercritical fluids (SEDS) techniques.

The pDNA used in this work is the pDNA mammalian expression vector encoding for green fluorescent protein (gWIZ^{TM} – GFP) and was sourced from GenoVac, Germany (pDNA stock concentration of 5 g/L). *In-situ* co-precipitation of hydroxyapatite (HAp) particles by GAS method with plasmid DNA (pDNA) was carried out by adding 1 ml of TE-$CaCl_2$ buffer (Tris-EDTA), which contained 10 µg of pDNA (pDNA concentration of 10 mg/L) to a 30 ml volume of HAp in DMSO [Sigma Aldrich, UK, CAS number 67-68-5] solution in a 50 ml beaker. The concentration of HAp in the DMSO solution was 3 mg/L. The final solution volume was 31 ml. The GAS method processing rig consisted of a 500 ml pressure vessel (Parr, Moline, USA) in which the beaker containing the HAp and pDNA solution was placed inside (refer to Figure 4.1 in Chapter 4). The carbon dioxide (CO_2) [BOC UK, CAS number

124-38-9] flowrate supply was set by the CO_2 pump, using an integral software (Thar Instrument Process Suite). Prior to the GAS processing, the rig was heated to the desired operating temperature, which was also controlled by the integral software. The CO_2 flow was then introduced into the system to reach the respective set pressure. A back pressure regulator was used to maintain the pressure within the system. The CO_2 supply was then stopped after 5 hours and the GAS processing rig was depressurised and cooled down. During the anti-solvent process, the CO_2 expanded the DMSO solvent, which led to supersaturation and the formation of the HAp-pDNA containing particles. The particles produced were retained inside the beaker and were removed for further analysis. The waste DMSO solvent was collected by opening the cyclone valve and was further analysed for pDNA detection. The experimental work was carried out at 40 ^{o}C, 50 ^{o}C or 60^{o}C at a fixed pressure of 150 bar. The CO_2 flowrate supply into the vessel was set at 40 g/min for all of the experimental work. The GAS experiments were repeated for 6 times.

In-situ co-precipitation of hydroxyapatite (HAp) particles by SEDS method with plasmid DNA (pDNA) was carried out by adding 17 ml of TE-$CaCl_2$ buffer (Tris-EDTA), which contained 170 µg of pDNA (pDNA concentration of 10 mg/L) to a 500 ml volume of HAp in DMSO solution. The SEDS processing procedure is the same as mentioned in section 4.2.1.2 in Chapter 4.

6.2.1.2 Post co-precipitation attachment of pDNA on calcium phosphates (CaP) particles produced by other processing techniques.

This experimental work is based on Barralet et al's work [Barralet et al. (2008)]. In the post co-precipitation of CaP particles from the sol-gel technique (refer to Chapter 3), anti-solvent techniques, GAS and SEDS (refer to Chapter 4) and new calcium phosphate route (refer to Chapter 5), the concentration of pDNA used was 50 mg/L. 10 µg (2µl) of pDNA from a stock solution of 5 g/L was dissolved in 198 µl of TE-$CaCl_2$ buffer (Tris-EDTA), giving a final volume of 200 µl. This solution was then mixed with 150 µg of CaP samples for each, which was vortexed for 15 seconds (Vortex Genie 2, Scientific Industries Inc., USA). The CaP-pDNA complex was incubated for 10 minutes at room temperature. Each post co-precipitation attachment of pDNA was repeated for 6 times.

6.2.2 Gel electrophoresis

In this work, Tris/Borate/EDTA (TBE), the running buffer for separating the pDNA was used. This buffer contained a mixture of 90 mM Tris, 90 mM boric acid and 2 mM EDTA at pH 8, which was made up a 5x concentration stock. The running buffer of 0.5x was prepared by diluting 100 ml of the 5x concentration stock into a 1 L volumetric flask with distilled water (dH_2O). 1% agarose matrix was prepared by dissolving 1 gram of agarose Type II powder [Sigma Aldrich, UK, CAS number 9012-36-6] in 100 ml of 1x TBE buffer and the agarose solution was poured into the gel rack container. The wells/slots were prepared by inserting a comb at one side of the agarose matrix, located about 5 - 10 mm from the end of the gel rack container. The agarose matrix was let to set for 30 minutes. Once it became solid, it was put into

the electrophoresis tank, and 0.5x TBE running buffer (500 ml) was poured until the agarose matrix was completely submerged under the running buffer solution.

The wells were then filled with pDNA loaded CaP samples and pDNA marker was filled at the first well as reference of the pDNA molecular weight size. The electrophoresis measurements were undertaken at 75 volt (V) for 1 hour. When the electrophoresis measurement has stopped, the gel matrix was transferred into a container and ethidium bromide was poured to stain the pDNA for 45 minutes. The gel was washed several times with distilled water. Lastly, the gel was placed in an Ultraviolet Transilluminator device and images were taken using the Kodak UV Imagersoftware.

6.2.3 Binding efficiency analysis (pDNA mass balance)

The binding efficiency analysis was done by first making a standard curve (R^2 = 0.9988, see Appendix for Chapter 6) for the unbound pDNA. Different amount of pDNA from stock solution of 5 mg/L (0 µg in 200 µl of TE-$CaCl_2$ buffer, 2.5 µg in 199.5 µl of TE-$CaCl_2$ buffer, 5.0 µg in 199 µl of TE-$CaCl_2$ buffer, 7.5 µg in 198.5 µl of TE-$CaCl_2$ buffer and 10.0 µg in 198 µl of TE-$CaCl_2$ buffer) were prepared and its absorbance was taken at 260 nm using a UVIKON 922 spectrophotometer (Kontron Instruments). After the CaP-pDNA complex was incubated for 10 minutes at room temperature, the particles were separated by centrifugation (Centrifuge 5418, Eppendorf A. G. Germany) at 7000 rpm for 5 minutes and the supernatant absorbance was once again measured at 260 nm. The amount of unbound pDNA was quantified by comparing the absorbance to the standard curve. The amount of bound pDNA was obtained by extracting the known amount of unbound pDNA with the initial amount of pDNA used in the post co-precipitation experimental work (10 µg) to complete the mass balance.

6.2.4 *In-vitro* transfection studies

6.2.4.1 Materials

NIH/3T3 fibroblast and MC3T3 osteoblast cell lines were donated by the School of Dentistry, University of Birmingham. 10 % Dulbecco's Modified Eagle's Medium (MEM), 10 % foetal bovine serum (FBS) and Dulbecco's Phosphate-Buffered Saline (PBS) solution were obtained from Sigma-Aldrich UK. Buffer P2 lysis buffer and PolyFect were obtained from Qiagen UK. The 24-well cell culture dish was supplied by Corning Costar.

6.2.4.2 Cell culture preparation

NIH/3T3 fibroblast and MC3T3 osteoblast cell cultures were grown in 10 % Dulbecco's Modified Eagle's Medium (MEM) supplemented with 10 % foetal bovine serum (FBS). Before transfection experiments, cells were plated 24 hour in advance at a density of 2 x 10^4 cells/well (1 ml volume) in a 24-well cell culture dish. Cells were plated into each well by using a 1000 µl capacity pippette with steriled pippette tip.

6.2.4.3 CaP-pDNA complexes preparation and *in-vitro* transfection procedure

The CaP-pDNA complexes were prepared by mixing 2 µl (10 µg) of gWiz-GFP pDNA mammalian expression vector encoding green fluorescent protein (GFP) into 198 µl of TE-$CaCl_2$ buffer which were then mixed with 150 µg of each of the CaP sample, which were also vortexed for 15 seconds (Vortex Genie 2, Scientific Industries Inc., USA). The CaP-pDNA complex was incubated for 10 minutes at room temperature.

Each CaP-pDNA complex was then transfer to a cell wall plated 24 hour before transfection by using a 1000 µl capacity pippette with steriled pippette tip. PolyFect (Qiagen UK) was used as a positive control to monitor consistency of the transfection experiments. Controls included cells without any treatment and cells transfected with only the CaP particles. GFP expression was monitored 24 and 48 hour post-transfection by fluorescence microscopy (Carl Zeiss Axiolab) and fluorescence light micrographs taken by Canon PowerShot G5 camera mounted on top of the microscope. Fluorescence was quantified in cell lysates using a microplate reader (Promega Glomax Multi Detection System) 48 hour post-transfection. Cells were lysed by using Buffer P2 lysis buffer. In this procedure, each well was washed with 1 ml PBS to remove residual media. Then, 400 µl of the cell lysis buffer were added to each well. The culture dish was incubated on ice for 5 minutes. Cells were scraped and sonicated briefly. Lastly, the extract was centrifuged for 10 minutes at 14,000 rpm in a cold microfuge and supernatant removed for fluorescence quantification analysis by using a micropate reader.

6.3 Results and discussion

6.3.1 pDNA attachment *in-situ* onto particles using the GAS and SEDS techniques

pDNA *in-situ* co-precipitation on particles by the GAS technique showed inefficient binding of the pDNA onto the HAp particles obtained. The amount of unbound (free) pDNA in the recovered DMSO solution was found to be in the region of 88 to 92 %. One reason for the low co-precipitation of HAp with pDNA by the GAS technique was assumed to be due to the low concentration of the pDNA within the prepared solution. The final concentration of pDNA in the prepared solution was only 0.32 mg/L (10 μg of pDNA in 31 ml of HAp-DMSO solution). This was the similar case for the pDNA *in-situ* co-precipitation on particles by the SEDS technique. SEDS has high rates of mass transfer and the affinity of pDNA to HAp particles would been in competition with pDNA and DMSO, which would have led to pDNA being stripped from the system before it could attach onto the HAp particles. For the post precipitation attachment (CaP by sol-gel, GAS, SEDS and new calcium phosphate route), the final pDNA concentration within the incubation system was 50 mg/L. A higher concentration would have led to an increase in the electrostatic interaction between the pDNA and the HAp crystals. Furthermore, as the GAS method is a slow anti-solvent precipitation process (compared to SEDS), the pDNA, which is naturally polar due to its negatively charged phosphate backbone [Truong-Le (1999)] and total miscibility in the DMSO solution, may have easily been stripped away by the supercritical CO_2 and DMSO mixture. The low concentration of the HAp in the prepared solution (3 mg/L) might also have affected the co-precipitation process. A gel for detecting the presence of pDNA for the pDNA attachment *in-situ* by the GAS method is shown in Figure 6.1 It clearly shows that there were no detectable bands for all of the conditions for the co-precipitation by this technique. Tservistas et al. (2000) have reported on the processing of nucleic acids by the SEDS technique,

to produce dry powder formulations of pDNA with mannitol as the main excipient from aqueous solution. They showed that the pDNA was degraded as a result of the low pH within the processing system due to the presence of carbonic acid. The DMSO used in this study for pDNA attachment *in-situ* onto HAp particles using the GAS and SEDS techniques had residual water content of 400 ppm, thus even with this small amount of water, the formation of carbonic acid is possible inside a CO_2 rich environment. This would have led to a pH drop during processing and might degrade the pDNA in this study.

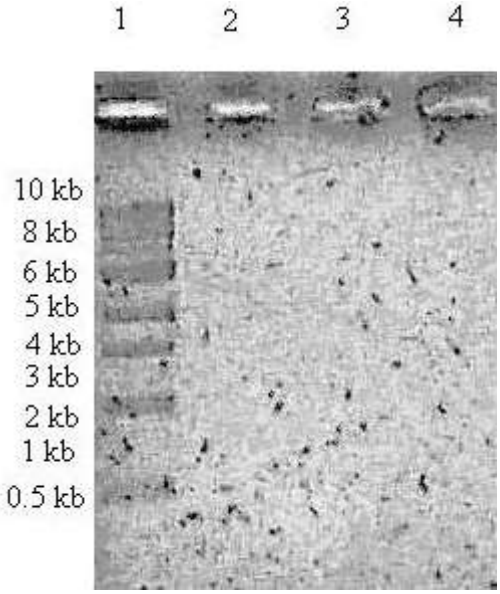

Figure 6.1 Gel electrophoresis of *in-situ* co-precipitation of GAS technique particles with pDNA. Lane 1: M.W. marker, Lane 2 - 4: GAS at 40 ^{o}C, 50 ^{o}C and 60 ^{o}C *in-situ* (*i.e* under pressure) co-precipitation. All GAS samples were carried out at a pressure of 150 bar. SEDS samples also showed similar behavior to the GAS samples.

6.3.2 pDNA post co-precipitation attachment

The gels for the post-precipitation attachment showed the presence of pDNA on/within the particles by the bands on the respective gel. These are clearly shown in Fig. 6.2 and 6.3. The pDNA molecular weight used in these studies can be determined from the pDNA standard molecular weight ladder (shown on Lane 1 of each respective gel). The molecular weight of the pDNA used is 5757 base pair (5.7 kb) shown by the position of the last strip of the band (representing the open circular pDNA), which is located between the 5 kb and 6 kb of the standard pDNA ladder. The post co-precipitation method is therefore an efficient method to bind pDNA to CaP particles as compared to *in-situ* co-precipitation. Many previous studies by other groups have showed the efficiency of post co-precipitation, for example James et al. (1987), Truong-Le (1999) and Elliott (1994). Jordan et al. (1996) reported that pDNA-calcium phosphate co-precipitates can arise spontaneously in supersaturated solutions, but only in a narrow range of physico-chemical conditions, with principally the calcium and phosphate concentrations being the most significant.

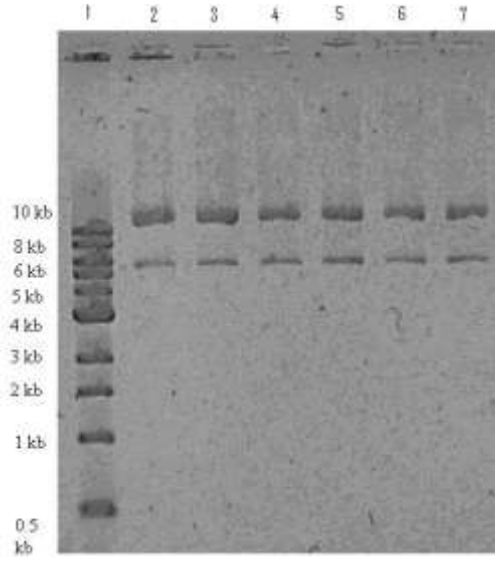

Figure 6.2 Gel electrophoresis of HAp post co-precipitation with pDNA for sol-gel and GAS particle processing methods. Lane 1: M.W. marker, Lane 2: HAp prepared by sol-gel at 200 rpm, Lane 3: HAp prepared by sol-gel at 2200 rpm, Lane 4: HAp prepared by sol-gel at 7000 rpm, Lane 5: HAp prepared by GAS at 40 ^{o}C, Lane 6: HAp prepared by GAS at 50 ^{o}C and Lane 7: HAp prepared by GAS at 60 ^{o}C. All GAS samples were carried out at a pressure of 150 bar.

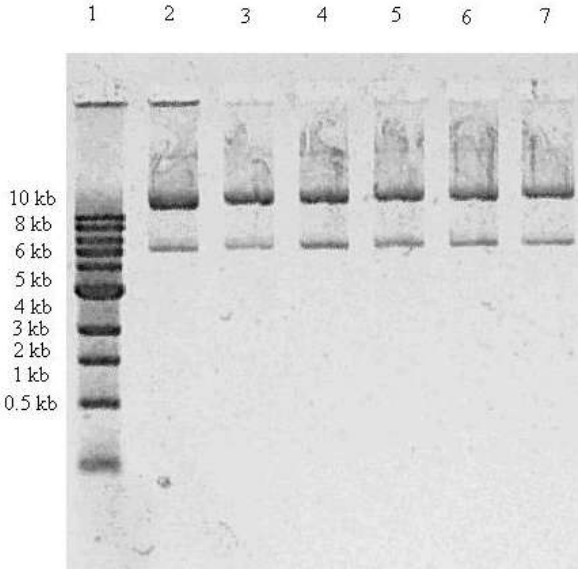

Figure 6.3 Gel electrophoresis of new CaP route post co-precipitation with pDNA. Lane 1: M.W. marker, Lane 2: CaP prepared by direct precipitation with Ca/P ratio of 0.40, Lane 3: CaP prepared by direct precipitation with Ca/P ratio of 1.00, Lane 4: CaP prepared by direct precipitation with Ca/P ratio of 2.50, Lane 5: CaP prepared by SEDS method with Ca/P ratio of 0.33, Lane 6: CaP prepared by SEDS method with Ca/P ratio of 1.00 and Lane 7: CaP prepared by SEDS method with Ca/P ratio of 3.00.

Barralet et al.'s method [Barralet et al. (2008)] showed the efficiency of the post co-precipitation and they reported a binding efficiency as high as 97% for co-precipitation of the same pDNA used in this work with their CaP nanoparticles which had primary particle size in the range of 20 – 150 nm determined by DLS.

6.3.3 Binding efficiencies

To determine the binding efficiency for each of the post co-precipitate CaP samples, the amount of unbound pDNA was analysed. The amount of unbound pDNA was quantified by comparing the absorbance of the supernatant after the incubated post co-precipitation with the standard curve (see 6.2.3). The amount of bound (attached) pDNA was obtained by extracting the known amount of unbound (free) pDNA from the standard curve with the initial amount of pDNA used which was 10 µg in all of the CaP samples. In all cases, the error was no worse than ± 4% as shown in Table 6.1.

An example calculation for the determination of post- co-precipitation bound pDNA onto a CaP sample for the GAS method at 40 ^{o}C and 150 bar is shown below:

Mass balance of pDNA (equation from the standard curve),

Value of supernatant obtained by spectrometry, $y = mx + c$

$0.151^{*} = 0.100\ x - 0.003$

$0.151 + 0.003 = 0.100\ x$

$0.154 = 0.100\ x$

$x = 1.540$ µg

* absorbance reading from spectrophotometry

pDNA unbound (%) = 1.540 µg / 10 µg = 15.40 % ≈ 15 %

pDNA bound (%) = (100 – 15) % = 85 %

This result is shown as number 8 on Table 6.1

All other binding calculations are tabulated in Appendix for Chapter 6. A table for the pDNA binding efficiency for various CaP samples prepared by post co-precipitate is shown in Table 6.1 The binding efficiency investigated is based upon selecting several CaP particle size and processing technique samples.

Sample	Binding efficiency	CaP non pDNA particle, sized by DLS (nm)
1) *In-situ* GAS co-precipitate	~ 3 % *	196 ± 8
2) Sol-gel at 200 rpm and 20 ^{o}C	84 ± 2 %	211 ± 3
3) Sol-gel at 200 rpm and 40 ^{o}C	82 ± 3 %	219 ± 3
4) Sol-gel at 2200 rpm and 20 ^{o}C	88 ± 2 %	148 ± 1
5) Sol-gel at 2200 rpm and 40 ^{o}C	87 ± 2 %	152 ± 2
6) Sol-gel at 7000 rpm and 20 ^{o}C	91 ± 1 %	145 ± 1
7) Sol-gel at 7000 rpm and 40 ^{o}C	92 ± 2 %	145 ± 3
8) GAS at 40 ^{o}C and 150 bar	85 ± 2 %	168 ± 5
9) GAS at 50 ^{o}C and 150 bar	84 ± 3 %	173 ± 3
10) GAS at 60 ^{o}C and 150 bar	82 ± 2 %	186 ± 4
11) GAS at 50 ^{o}C and 100 bar	84 ± 3 %	177 ± 5
12) GAS at 50 ^{o}C and 200 bar	86 ± 2 %	163 ± 6
13) SEDS at 40 ^{o}C, 1 ml/min and 60 g/min of CO_2	94 ± 2 %	131 ± 4
14) SEDS at 40 ^{o}C, 2 ml/min and 60 g/min of CO_2	88 ± 2 %	153 ± 4
15) SEDS at 50 ^{o}C, 1 ml/min and 60 g/min of CO_2	92 ± 2 %	141± 5
16) SEDS at 50 ^{o}C, 2 ml/min and 60 g/min of CO_2	86 ± 3 %	159 ± 3
17) New CaP route at 0.40 Ca/P ratio	80 ± 2 %	216 ± 2
18) New CaP route at 0.75 Ca/P ratio	82 ± 3 %	214 ± 3
19) New CaP route at 1.00 Ca/P ratio	83 ± 2 %	215 ± 4
20) New CaP route at 1.33 Ca/P ratio	83 ± 2 %	214 ± 2
21) New CaP route at 1.67 Ca/P ratio	83 ± 2 %	218 ± 6
22) New CaP route at 2.50 Ca/P ratio	83 ± 2 %	219 ± 7
23) New CaP route (0.33 Ca/P ratio by SEDS)	79 ± 3 %	218 ± 3
24) New CaP route (1.00 Ca/P ratio by SEDS)	83 ± 2 %	215 ± 6
25) New CaP route (3.00 Ca/P ratio by SEDS)	83 ± 2 %	217 ± 5

Table 6.1 Binding efficiency data of various CaP-pDNA complexes.

* most pDNA stripped away and recovered in cyclone (97 %).

6.3.4 Comparison of analytical data from the post co-precipitation attachment of sol-gel, anti-solvent methods (GAS & SEDS) and new CaP route with pDNA.

There is little difference in pDNA binding efficiencies between one CaP sample and the other. Overall, it can be said that smaller particle sizes led to better binding efficiencies. Theoretically, with smaller particle size and higher ratio of Ca^{2+} ions in the CaP structure, its binding capacity is higher [Truong-Le (1999)]. This would lead to larger specific area for the smaller particles and greater potential for binding interaction between the phosphate backbones of pDNA with more Ca^{2+} ions in the apatitic structure. For the sol-gel method, HAp particles produced at higher stirring rates gave higher binding capacity. As an example, HAp produced at sol-gel conditions of 7000 rpm at 40 ^{o}C (with average particle size of 145 nm) had binding capacity of 92 %, as compared to the HAp produced at 200 rpm at 40 ^{o}C (with average particle size of 211 nm), which the binding capacity was 82 %. For the HAp samples produced by the supercritical technique, the GAS post co-precipitation samples showed binding efficiencies between 83 to 86 %. The limited range of these values showed that GAS process conditions (temperature and pressure) were insignificant to the binding efficiencies based upon the resultant particle sizes.

For the SEDS post co-precipitation samples, the HAp at 40 ^{o}C, solvent flowrate of 1 ml/min and antisolvent flowrate of 60 g/min (with average particle size of 131 nm) showed a binding capacity of 94 %, giving the highest binding capacity among all of the samples analysed. Once again, this high binding capacity was due to the small particle size of the mentioned SEDS sample. In contrast, for the HAp SEDS processed sample at 50 ^{o}C, solvent flowrate of 1 ml/min and antisolvent flowrate of 60 g/min (with average particle size of 141 nm), the binding capacity

was 92 %. Lastly, for the new CaP route by direct precipitation, the Ca/P ratio of the 2.50 (with average particle size of 219 nm) gave a binding capacity of 83 % and the Ca/P ratio of 0.40 (with average particle size of 216 nm) gave a binding capacity of 80 %. As the particle sizes produced by the new CaP route by direct precipitation are similar, the higher binding efficiency could be due to the amount of calcium present in respective sample, though this is only an assumption and may be insignificant. For the new CaP route by SEDS processing, the Ca/P ratio of 3.00 (with average particle size of 217 nm) gave a binding capacity of 83 % and the Ca/P ratio of 0.33 (with average particle size of 218 nm) gave a binding capacity of 79 %. Again this could be an effect of the amount of calcium present in the respective sample. Varying the Ca/P ratio had no noticeable effect on the binding efficiency for these particles.

The binding efficiencies results obtained will be used for the transfection studies, where some of the best and poor binding efficiencies will be considered. For the fluorescence quantification analysis, the best CaP binding efficiency sample from each production technique (CaP by sol-gel, GAS, SEDS and new calcium phosphate route) will be chosen and compared with the commercial transfection agent, PolyFect. The cellular uptake of gene vector is by endocytosis mechanism, where a particle size limit of around 200 nm has been reported [Xiang et al. (2006)]. All the particles produced are within this size limit.

6.3.5 GFP expression

Transfection was detected by fluorescence microscopy after the incubation of the NIH/3T3 fibroblast and MC3T3 osteoblast cell lines with the CaP-pDNA complexes. From the GFP expression observed by the fluoresence microscopy, it was noted that all of the CaP-pDNA complexes were taken up by both cell lines and the gWiz-GFP pDNA mammalian expression vector encoding green fluorescent protein fluoresced under the fluorescence microscope. PolyFect, a commercial transfection vector which was used as a positive control to monitor consistency of the transfection experiments also showed that the pDNA bound to it were taken up by both cell lines. In this study, controls included cells without any treatment and cells transfected in the absence of pDNA (just CaP particles). Fluoresence light micrographs for both controls in the two cell lines showed no GFP expression, just as expected. The fluorescence light micrographs of some of the transfected CaP-pDNA complexes in the NIH/3T3 fibroblast and MC3T3 osteoblast cell lines are shown in Table 6.2. The green fluorescence indicates the pDNA uptake by the cells and subsequently the GFP expression.

Sample	Cell culture	
	NIH/3T3 fibroblasts	**MC3T3 osteoblasts**
1) Cells without CaP-pDNA complex (control).	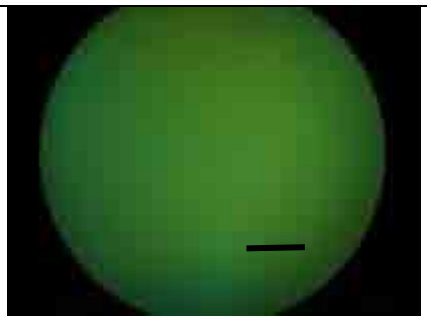	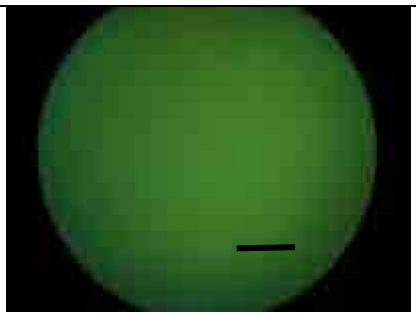
2) Cells with only CaP particles (control).	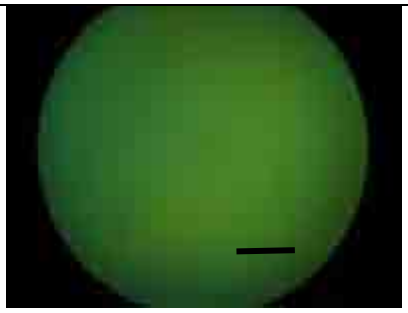	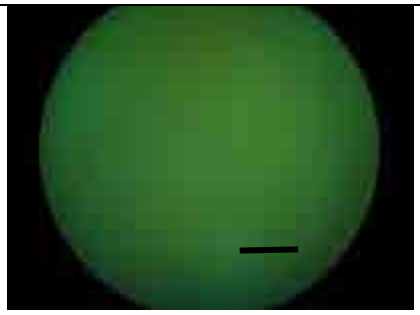
3) HAp produced at 200 rpm and 20 ^{o}C by agitator.	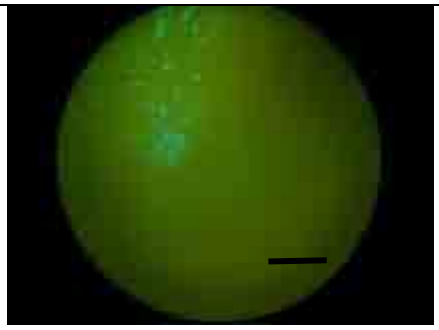	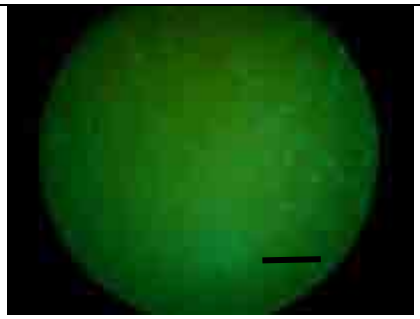
4) HAp produced at 2200 rpm and 20 ^{o}C by agitator.		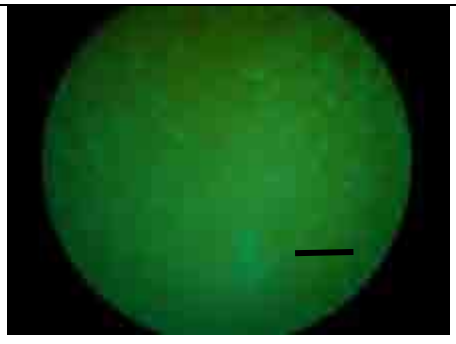

Sample	Cell culture	
	NIH/3T3 fibroblasts	MC3T3 osteoblasts
5) HAp produced at 3000 rpm and 20 ^{o}C by homogeniser.	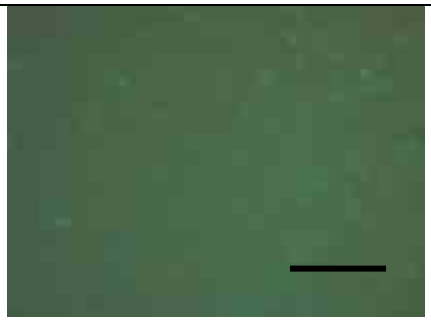	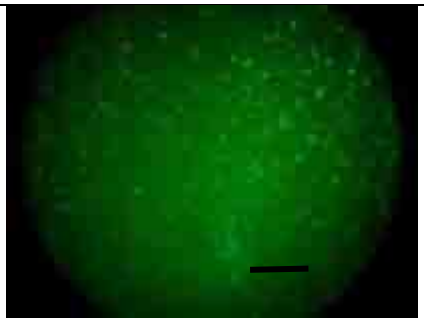
6) HAp produced at 7000 rpm and 20 ^{o}C by homogeniser.	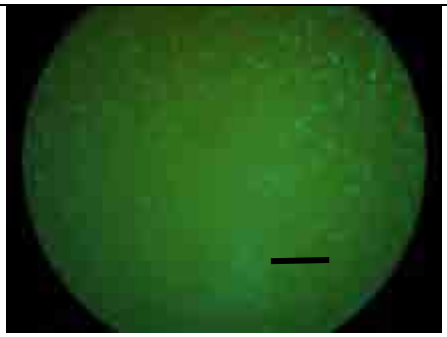	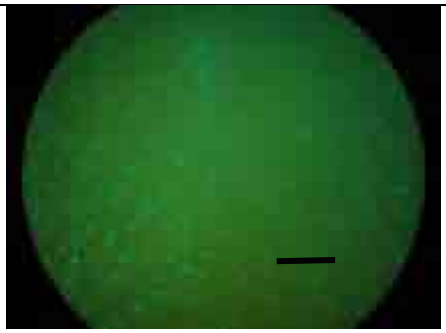
7) HAp produced by GAS at 40 ^{o}C and 150 bar.	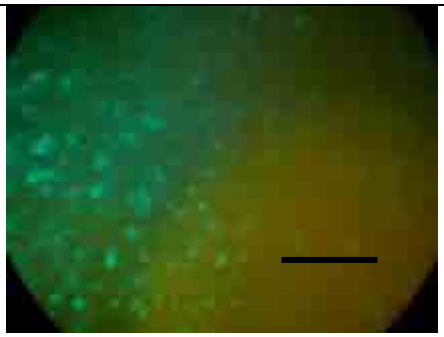	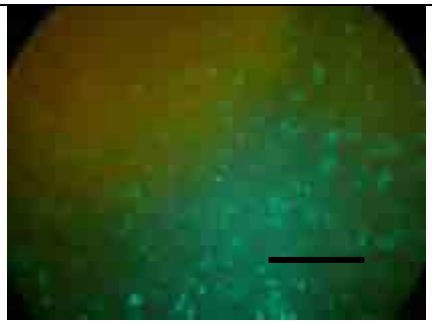
8) HAp produced by SEDS at 50 ^{o}C, 1 ml/min of solvent flowrate and 60 g/min of CO_2.	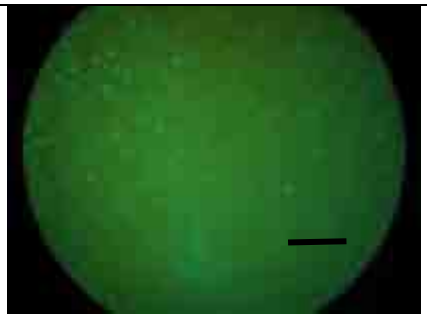	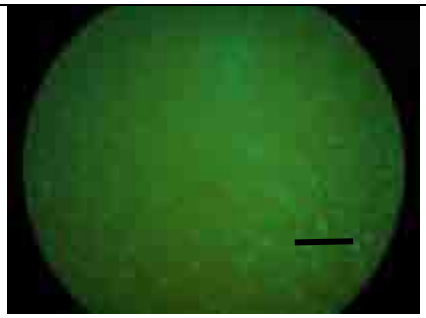

Sample	Cell culture	
	NIH/3T3 fibroblasts	**MC3T3 osteoblasts**
9) New route at Ca/P ratio of 0.40.	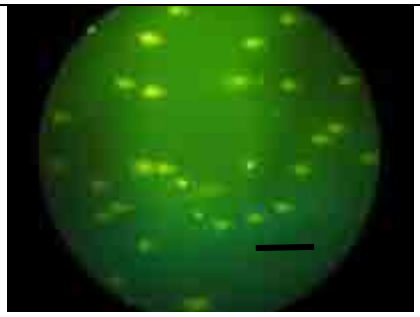	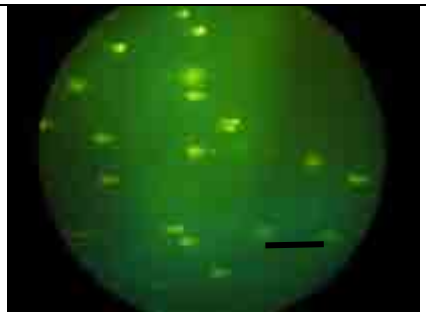
10) New route by SEDS at Ca/P ratio of 3.00.	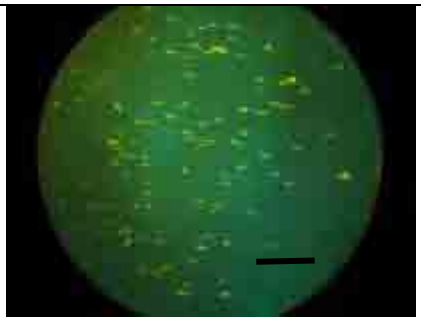	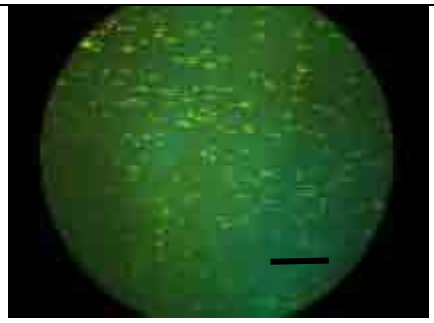
11) New route by SEDS at Ca/P ratio of 0.33.	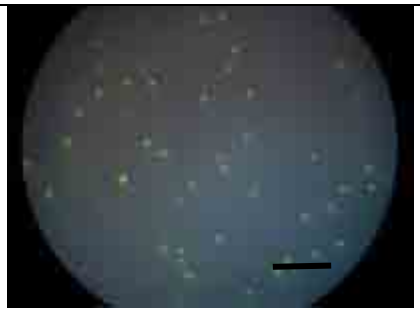	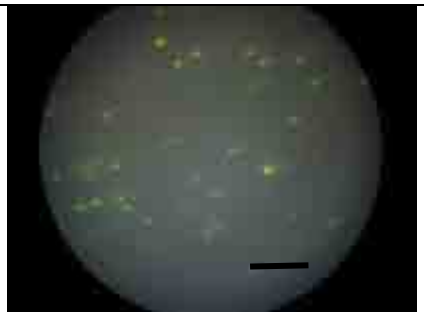
12)PolyFect (positive control).	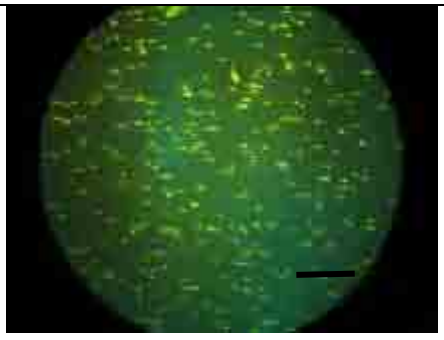	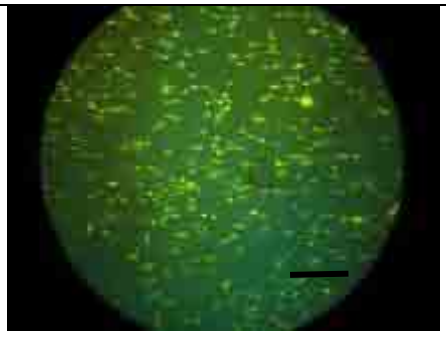

Table 6.2 Fluoresence light micrographs of the NIH/3T3 fibroblast and MC3T3 osteoblast cell lines transfected with some of the CaP-pDNA complexes (scale bar unit is 250 µm). The green fluorescence indicates the pDNA uptake by the cells and subsequently the GFP expression.

Calcium phosphate has been used for transfecting therapeutic genes into mammalian cell lines since 1973. In that year, Graham and van der Eb (1973) prepared the calcium phosphate carrier for transfection by mixing of calcium chloride solution with DNA and a subsequent addition of phosphate-buffered saline solution produced nano- and microparticles of calcium phosphate with DNA. This dispersion is then added to a cell suspension, and the nanoparticles were taken up by the cells. There are a number of reported works on using calcium phosphate as a gene vector includes Chowdhury et al. (2004), where they reported a high-efficiency gene delivery for expression in mammalian cells (HeLa and NIH/3T3 cell lines) by nanoprecipitates of Ca-Mg phosphate with particle size range of 120 – 500 nm, determined by DLS. Meanwhile, Epple et al. (2004 and 2006) reported the effectiveness of transfection of cells with multi-shell calcium phosphate-DNA nanoparticles with particle size range of 10 – 20 nm, determined by TEM in T-HUVEC (transformed human umbilical vein endothelial cells), HeLa (human transformed and cervix epithelial cells) and LTK (mouse L cells lacking thymidine kinase) cell lines. Maitra et al. (2005) reported on a highly efficient non-viral vector for gene delivery by using pDNA loaded calcium phosphate nanoparticles with particle size range of 100 – 120 nm, determined by DLS in HeLa cell line.

Most recent works included that of Giger et al. (2011) who reported on gene delivery with biphosphonate-stabilised calcium phosphate nanoparticles with particles sizes of around 200 nm determined by DLS. Olton et al. (2011) reported on the intracellular trafficking pathways involved in the gene transfer of nano-structured calcium phosphate-pDNA particles, however, they have not reported on the particle size.

6.3.6 Fluorescence quantification

The quantity of GFP expressed by transfected cells was determined by quantifying the fluorescence of the cell lysates. Transfection of NIH/3T3 fibroblast cell line with CaP-pDNA complexes was consistently around 20 – 30 % less than that of the commercial transfection agent PolyFect; however, gene expression levels were similar with that achieved with PolyFect in MC3T3 osteoblast cell line. This shows that the cell type has influence on the efficiency of gene expression. Transfection efficiencies of the CaP-pDNA complexes which were compared to PolyFect in NIH/3T3 and MC3T3 cell lines are shown in Figure 6.4 and 6.5 respectively.

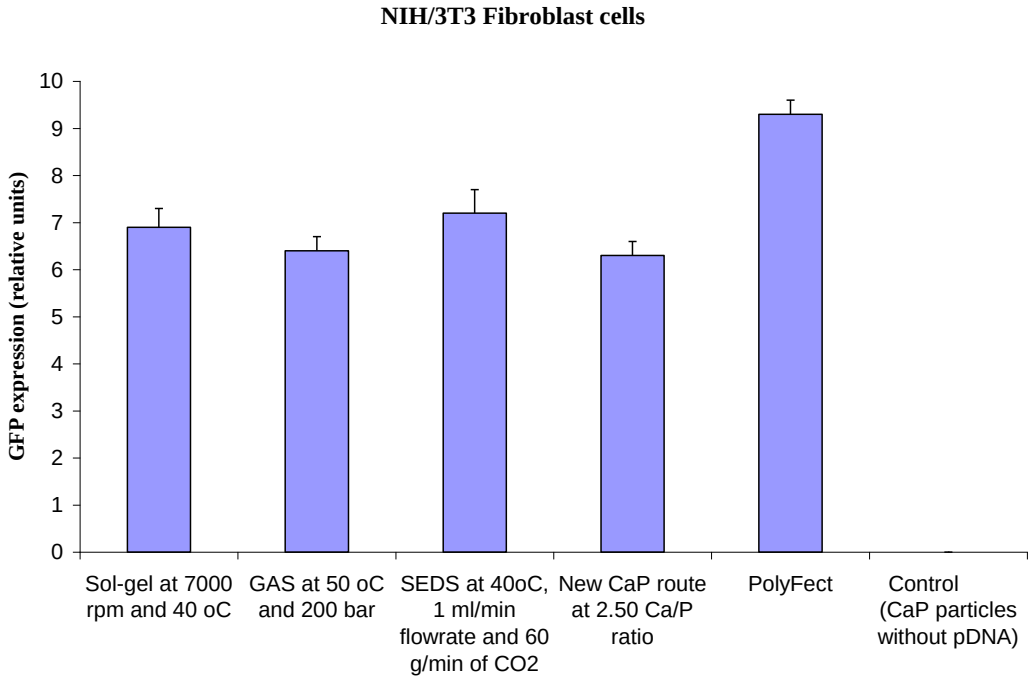

Figure 6.4 Transfection efficiencies of some of the CaP-pDNA complexes which were compared to PolyFect in NIH/3T3 fibroblast cell line.

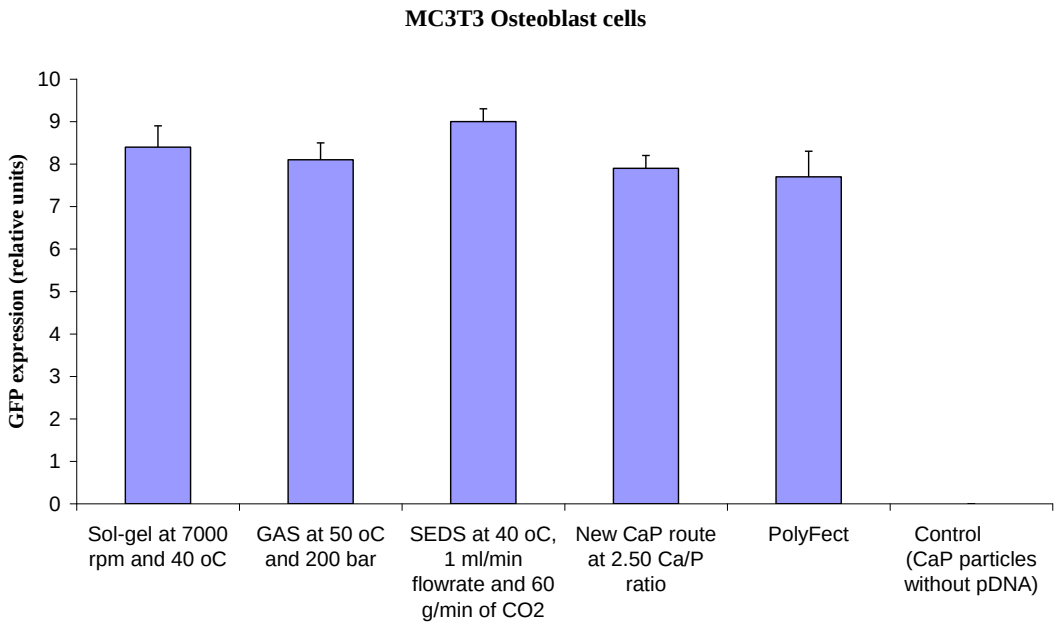

Figure 6.5 Transfection efficiencies of some of the CaP-pDNA complexes which were compared to PolyFect in MC3T3 osteoblast cell line.

The CaP-pDNA complexes were shown to be a reliable transfection vector in both the NIH/3T3 fibroblast and MC3T3 osteoblast cell lines. The CaP-pDNA complexes were readily taken up by the cells as shown by the fluorescence light micrographs in Table 6.2. Lee et al. (1999), Chowdhury et al. (2004) and Fu et al. (2005) had tested NIH/3T3 fibroblasts previously for transfection *in vitro*, as this cell line is a common cell choice given the abundance of fibroblasts in connective tissue.

Meanwhile, MC3T3 osteoblast cell line has been transfected using calcium phosphate previously by Kuroki et al. (1994). An osteoblastic cell line was chosen to demonstrate the potential for the

transfection of bone tissue which may have application in enhanced healing or tissue engineering of hard tissues. Kuroda et al. (2005) and Endo et al. (2006) have reported on calcium phosphate that has been used to effectively transfect bone tissue *in vivo*.

Barralet et al. (2008) reported in their work that they have achieved a transfection in their NIH/3T3 fibroblast cells of around 40 – 50 % as compared to the commercial transfection agent PolyFect; however, gene expressions levels were found to be often greater than three times than that achieved with PolyFect in their MC3T3-E1 osteoblastic cells. The differences in the results between this work and theirs may be due to the differences in the calcium phosphate particle size (they reported a primary particle size range of 20 – 150 nm by DLS) and also the strains of NIH/3T3 fibroblast and MC3T3-E1 osteoblast cell lines that they used. In this study, the fluorescence quantification for the SEDS sample produced at the conditions of 40 ^{o}C, solvent flowrate of 1 ml/min and CO_2 flowrate of 60 g/min showed the highest value as compared to three other best CaP samples produced by different methods in both cell lines. This may be due once again to the resultant particle size (with average particle size of 131 nm) which gave higher binding efficiency as mentioned earlier, thus higher GFP expression in both cell lines. This sample also showed that it was around 20 % less efficient as compared to the commercial transfection agent, PolyFect in the NIH/3T3 cell line; however, gene expression levels were around 20 % higher than that achieved with Polyfect in the MC3T3 cell line.

6.4 Conclusions

The *in-situ* co-precipitation of pDNA and HAp particles by the GAS and SEDS techniques had shown that it was not successful due to low concentration of bound pDNA as a result of it being removed by the CO_2 and DMSO mixture. pDNA would have greater affinity to DMSO than CaP under the process conditions. Furthermore, the residual water content in the DMSO solvent would have led to the formation of carboxylic acid, thus lowering the pH and might degrade the pDNA. Post co-precipitation results have shown that high pDNA binding efficiencies are achievable with binding efficiencies between 79 to 94 %. The lowest value of 79 % was obtained for the CaP sample of new CaP route for a Ca/P ratio of 0.33 obtained by SEDS processing. The highest value of 94 % was the HAp SEDS processed sample at 40 ^{o}C, solvent flowrate of 1 ml/min and antisolvent flowrate of 60 g/min (with average particle size of 131 nm). This sample also showed good gene expression as determined by the fluorescence quantification in both the NIH/3T3 and MC3T3 cell lines. The binding efficiencies were shown to be affected primarily by the respective particle size and also the amount of calcium present in the samples, but this effect is only an assumption and may be insignificant.

It was noted that all of the CaP-pDNA complexes were taken up by the NIH/3T3 fibroblastic and MC3T3 osteoblastic cell lines as evidenced from the qualitative fluorescence light micrographs. The CaP-pDNA complexes were also observed to be less effective (around 20 – 30 % less) as the commercial transfection vector, PolyFect in the NIH/3T3 fibroblastic cell line, however similar gene expression levels were observed with that achieved with PolyFect in MC3T3 osteoblastic cell line, as observed by the quantified fluorescence from the cell lysates. The HAp SEDS

processed sample at 40 ^{o}C, solvent flowrate of 1 ml/min and antisolvent flowrate of 60 g/min showed good gene expression in relation to PolyFect, as compared to three other best CaP samples produced from three different methods.

6.5 References:

Barralet, J. E. Pedraza, E. C. Bassett, D. C. McKee, M. D. Nelea, V. Gbureck, U. 2008. The importantce of particle size and DNA condenstation salt for calcium phosphate nanoparticle transfection. Biomaterials 29: 3384 – 3392.

Bloomfield, V. A. 1997. DNA condensation by multivalent cations. Biopolymers 44(3): 269 – 282.

Chowdhury, E. H. Kunou, M. Nagaoka, M. Kundu, A. K. Hoshiba, T. Akaike, T. 2004. High-efficiency gene delivery for expression in mammalian cells by nano-precipitates of Ca-Mg phosphate. Gene. 341: 77 – 82.

Elliot, J. C. 1994. Structure and Chemistry of the Apatites and Other Calcium Orthophosphates, Elsevier, Amsterdam.

Endo, M. Kuroda, S. Kondo, H. Maruoka, Y. Ohya, K. Kasugai, S. 2006. Bone regeneration by modified gene-activated matrix: effectiveness in segmental tibial defects in rats. Tissue Engineering 12(3): 489 – 497.

Epple, M. Welzel, T. Radtke, I. Meyer-Zaika, W. Heumann, R. 2004. Transfection of cells with custom-made calcium phosphate nanoparticles coated with DNA. Journals of Materials Chemistry. 14: 2213 – 2217.

Epple, M. Sokolova, V. V. Radtke, I. Heumann, R. 2006. Effective transfection of cells with multi-shell calcium phosphate-DNA nanoparticles. Biomaterials. 27: 3147 – 3153.

Fu, H. H. Hu, Y. H. McNelis, T. Hollinger, J. O. 2005. A calcium phosphate-based gene delivery system. Journal of Biomedical Materials Research Part A. 74A(1): 40 – 48.

Giger, E. V. Puigmarti-Luis, J. Schlatter, R. Castagner, B. Dittrich, P. S. Leroux, J. C. 2011. Gene delivery with biphosphonate-stabilised calcium phosphate nanoparticles. Journal of Controlled Release. 150: 87 – 93.

Graham, F. L. van der Eb, A. J. 1973. Transformation of rat cells by DNA of human adenovirus 5. Virology. 52: 456 – 467.

James, R. F. L. Grosveld, F. G. 1987, Techniques in molecular biology. In: Walker, J. M., Gaastra, W. (Eds.) 187 - 202.

Jordan, M. Schallhorn, A. Wurm, F. M. 1996. Transfecting mammalian cells. Optimization of critical parameters affecting calcium-phosphate precipitate formation. Nucleic Acids Res. 24: 596 – 601.

Kulkarni, V. I. Shenoy, V. S. Dodiya, S. S. Rajyaguru, T. H. Murthy, R. R. 2006. Role of calcium in gene therapy. Expert opinion on Drug Delivery. 3(2): 235 – 245.

Kuroda, S. Kondo, H. Ohya, K. Kasugi, S. 2005. A new technique with calcium phosphate precipitate enhances efficiency of in vivo plasmid DNA gene transfer. Journal of Pharmacological Sciences. 97(2): 227 – 233.

Kuroki, Y. Shiozawa, S. Sugimoto, T. Kanatani, M. Kaji, H. Miyauchi, A. 1994. Constitutive c-fos expression in osteoblastic mc3t3-e1 cells stimulates osteoclast maturation and osteoclastic bone-resorption. Clinical and Experimental Immunology. 95(3): 536 – 539.

Lee, J. H. Zabner, J. Welsh, M. J. 1999. Delivery of an adenovirus vector in a calcium phosphate co-precipitate enhances the therapeutic index of gene transfer to airway epithelia. Human Gene Therapy. 10: 603 – 613.

Maitra, A. Bisht, S. Bhakta, G. Mitra, S. 2004. pDNA loaded calcium phosphate nanoparticles: highly efficient non-viral vector for gene delivery. International Journal of Pharmaceutics. 288: 157 – 168.

Okazaki, M. Yoshida, Y. Yamaguchi, S. Kaneno, M. Elliot, J. C. 2001 Affinity binding phenomena of DNA onto apatite crystals, Biomaterials 22: 2459 – 2464.

Olton, Y. E. D. Close, J. M. Sfeir, C. S. Kumta, P. N. 2011. Intracellular trafficking pathways involved in the gene transfer of nano-structured calcium phosphate-pDNA particles. Biomaterials. 32: 7662 – 7670.

Truong-Le, V. L. Walsh, S.M. Schwabert, E. Mao, H. Q. Guggino, W. B. August, J. T. Leong, K. W. 1999. Gene transfer by DNA-Gelstin nanospheres. Arch. Biochem. Biophys. 47 - 56.

Tservistas, M. Levy, M. S. Lo-Yim, M. Y. A. O'Kennedy, R. D. York, P. Humphrey, G. O. Hoare, M. 2001. The formation of plasmid DNA loaded pharmaceutical powders using supercritical fluid technology. John Wiley & Sons, Inc.

Walters, R. W. Welsh, M. J. 1999. Mechanism by which calcium phosphate coprecipitation enhances adenovirus-mediated gene transfer. Gene Therapy. 6(11): 1845 – 1850.

Xiang, S.D. Scholzen, A. Minigo, G. David, C. Apostolopoulus, V. Mottram, P. L. 2006. Pathogen recognition and development of particulate vaccines: does size matter?, Methods 40 (1): 1 – 9.

7.0 Overall conclusions

For the HAp and intercalated HAp – Mg particles produced by sol-gel method in chapter 3, it can be concluded that the primary particle size for both the HAp and HAp – Mg particles decreased with higher agitation rates and can be explained in terms of the power input and turbulence within the mixing zone, which influences the nucleation rate. At higher agitation rates the filtered DLS data showed the formation of stable agglomerates as the agitation rate did not significantly affect the particle size above 2200 rpm. An increase in temperature from 20 to 40 ^{o}C had a slight effect on particle size. The intercalation of Mg into the HAp structure led to a decrease in particle size with increased $MgCl_2$ concentration and increased agitation rate, although this became less significant at agitation rates above 2200 rpm. The HAp particles produced at process conditions of 20 ^{o}C and 7000 rpm had an average size of 145 nm obtained by filtered DLS measurements, which was the smallest particle size for the HAp produced by the sol-gel method. Meanwhile, the intercalated HAp – Mg particles produced at process conditions of 20 ^{o}C, 7000 rpm and 140 mM $MgCl_2$ concentration had an average size of 141 nm obtained by filtered DLS measurements, which was the smallest particle size for the intercalated HAp – Mg produced by the sol-gel method. Different particle morphologies can be obtained at different agitation rates, which are dependant on equipment selection. Cuboid-like particles were obtained at lower agitation rates with the overhead stirrer while elongated particles can be obtained at higher agitation rate using the homogeniser.

From the supercritical processing techniques of GAS and SEDS that were carried out, HAp particles were successfully recrystallised. The HAp samples produced by both techniques gave similar characteristics in term of their FTIR, XRD and SEM analyses. They only differ in the particle size, where it can be concluded that SEDS processing technique yield smaller particle size as compared to GAS processing technique. The HAp particles produced by the SEDS technique at process conditions of 40 ^{o}C, 1 ml/min solvent flowrate and 60 g/min of CO_2 flowrate had an average particle size of 131 nm obtained by filtered DLS measurements. The SEDS technique was much superior than that of the GAS technique, due to the rate of supersaturation that it created whitin the sytem, where more CO_2 antisolvent interaction led to faster supersaturation and smaller nuclei. The particle size was shown to decreased with respect to the operating conditions of temperature, pressure and antisolvent to solvent ratio.

The particles produced by the direct precipitation method were identified to be mostly the brushite or dicalcium phosphate dihydrate (DCPD) phase as characterized by the intensed peak of 20.9^{o} 2θ on the XRD patterns. Meanwhile, the particles produced by the SEDS method were observed to be the monetite or dicalcium phosphate anhydrous (DCPA) phase, as characterized by the intensed peak of 30.3^{o} 2θ on the XRD patterns. The formation of these phases of CaP was due to the pH of the reaction solution during the precipitation process. It was noted that the pH decreased during the direct precipitation process due to the presence of carbonic acid by the mixture of water from the precursor solution and the CO_2 from the environment, which made the reaction solution acidic. The decrease in the pH was also due to the release of the hydrogen ions from the $H_2PO_4^{2-}$ dissociation. The particle size data by the filtered DLS measurements for the

direct precipitation process showed that the mean crystal sizes of the agglomerates are insensitive to the variation of initial calcium and phosphorus concentration.

In the SEDS method, the CO_2 rich environment within the system has lowered the pH during the precipitation process due to the minute amount of residual water in the DMSO (400 ppm) which may turn it acidic due to the formation of carbonic acid. DMSO was used to dissolve the precursors due to its solubility with supercritical CO_2 and produced monetite (DCPA), the anhydrous form of brushite (DCPD). Once again, the particle size data by the filtered DLS measurement for the SEDS technique showed that the mean crystal sizes of the agglomerates are insensitive to the variation of initial calcium and phosphorus ratio.

The *in-situ* co-precipitation of pDNA and HAp by the GAS method had shown that it was not successful due to low concentration of the pDNA and the stripping of the DMSO solvent by CO_2 which contained it. pDNA has much greater affinity to DMSO than CaP under the process conditions. Post co-precipitation results have shown that binding efficiency are achievable with efficiency binding between 79 to 94%, the lowest being the CaP sample of new CaP route at Ca/P ratio of 0.33 by SEDS processing, which was 79% and the highest was the HAp SEDS processed sample at 40 ^{o}C, solvent flowrate of 1 ml/min and antisolvent flowrate of 60 g/min (particle size of 131 nm).

The binding efficiencies were shown to be affected primarily by the respective particle size and also the amount of calcium present in the samples. The binding efficiency results could be further proven by undertaking transfection studies.

8.0 Future work

8.1 More characterisation of the produced HAp and CaP nanoparticles.

The HAp and CaP nanoparticles produced in this thesis by the wet chemistry method, supercritical fluid techniques of GAS and SEDS and also by the new route synthesis have shown to be a useful transfection vector in NIH/3T3 fibrolastic and MC3T3 osteoblastic cell lines. For this vector to be used intensively in *in-vitro* or *in vivo* studies, it will be necessary to further characterize both the specific surface area and the surface charge of the resultant nanoparticles.

The specific surface area of the nanoparticles gives the surface area measurement that is available for the attachment of the plasmid DNA. Surface charge measurement by zeta potential gives information of the surface charge before and after the CaP-pDNA co-precipitation. Besides that the investigation on the complex study of CaP crystal habit can be carried out in order to evaluate the changing crystal habit that may form amorphous or crystalline particles.

8.2 HAp produced by other supercritical processing techniques.

It is interesting to evaluate other potential supercritical processing techniques, such as Supercritical Anti-Solvent (SAS), which is similar in procedure with the Solution Enhanced Dispersion of Supercritical Fluids (SEDS) for the formation of HAp and CaP particles. Besides that, different solvent system can be investigated, such as using supercritical water. As the previous supercritical processings studies yield HAp and CaP particles in small quantities, the investigation of scale up in the respective supercritical processing will be of interest.

8.3 *In-vivo* study of the CaP-pDNA complex.

A further step, after the *in-vitro* transfection study, is to evaluate the potential of the produced CaP-pDNA complexes to be used in *in vivo* study. This will further explore its usage as a potent transfection vector. Besides that, the usage of other transfection vector other than the commercial transfection vector, PolyFect used in this work could be investigated. Different type of plasmid DNA could also be considered for future work.

9.0 Appendix

Appendix for Chapter 3

Appendix 3 A

'Effect of processing conditions on the formation of hydroxyapatite nanoparticles',

a paper submitted to the Journal of Powder Technology.

Appendix 3 B

Crystallinity

By using the following equation :

$$X_c = 1 - \frac{V_{112/300}}{I_{300}}$$

where I_{300} is the intensity of (300) diffraction peak and $V_{112/300}$ is the intensity of the hollow between (112) and (300) diffraction peaks of hydroxyapatite, which completely disappears in non-crystal samples.

For the HAp sample produced at 200 rpm and 20 ^{o}C, the $V_{112/300}$ and I_{300} data obtained from the XRD database are 520 counts and 1404 counts respectively.

So, value of X_c = 1 – (520/1404)

= 1 – 0.37

= 0.63 @ 63%.

Apendix 3 C

Scherrer's formula calculation example

$$Xs = \frac{0.9\,\lambda}{FWHM\cos\theta}$$

where, Xs = crytsllite size (nm)

λ = wavelength of X-ray beam (λ = 0.15406 nm for Cu Kα radiation)

FWHM = full width at half maximum for the difrractionpeak under consideration (rad)

θ = diffraction angle (^{o}) (2θ = 26.04^o)

$$Xs = \frac{0.9\,(0.15406)}{[\,0.151^o \times \frac{\pi}{180^o}\,] \times \cos 13.02}$$

$$= \frac{0.13865}{2.63545 \times 10^{-3} \times 0.97429}$$

= 0.13865 / 2.56769 x 10-3

= **54.00 nm**

(for HAp particles produced at processing conditions of 200 rpm and 40 ^{o}C)

Appendix 3 D

Particle sizing for HAp by DLS produced by sol-gel method (unfiltered)

Record Number	Sample Name	Measurement Date and Time	Temperature (°C)	Z-Average (nm)	PDI
1	200 (Unfiltered) 20°C	16/12/2008 12:18	25	384.9	0.252
2	200 (Unfiltered) 20°C	16/12/2008 12:21	25	368.4	0.235
3	200 (Unfiltered) 20°C	16/12/2008 12:24	25	364.2	0.232
4	200 (Unfiltered) 20°C	16/12/2008 12:27	25	342.8	0.224
5	200 (Unfiltered) 20°C	16/12/2008 12:30	25	372.9	0.246
6	200 (Unfiltered) 20°C	16/12/2008 12:33	25	388.7	0.268
7	200 (Unfiltered) 20°C	16/12/2008 12:37	25	395.4	0.296
8	200 (Unfiltered) 20°C	16/12/2008 12:40	25	349.5	0.222
9	200 (Unfiltered) 20°C	16/12/2008 12:43	25	383.7	0.266
Record Number	Sample Name	Measurement Date and Time	Temperature (°C)	Z-Average (nm)	PDI
1	200 (Unfiltered) 40°C	16/12/2008 12:53	25	423	0.297
2	200 (Unfiltered) 40°C	16/12/2008 12:57	25	387.8	0.263
3	200 (Unfiltered) 40°C	16/12/2008 13:00	25	413.2	0.298
4	200 (Unfiltered) 40°C	16/12/2008 13:04	25	406.6	0.235
5	200 (Unfiltered) 40°C	16/12/2008 13:08	25	388.5	0.261
6	200 (Unfiltered) 40°C	16/12/2008 13:12	25	411.2	0.281
7	200 (Unfiltered) 40°C	16/12/2008 13:16	25	415.4	0.254
8	200 (Unfiltered) 40°C	16/12/2008 13:19	25	408.6	0.276
9	200 (Unfiltered) 40°C	16/12/2008 13:23	25	389.8	0.259
Record Number	Sample Name	Measurement Date and Time	Temperature (°C)	Z-Average (nm)	PDI
1	1200 (Unfiltered) 20°C	16/12/2008 13:31	25	332.5	0.271
2	1200 (Unfiltered) 20°C	16/12/2008 13:34	25	365.1	0.287
3	1200 (Unfiltered) 20°C	16/12/2008 13:37	25	324.4	0.226

4	1200 (Unfiltered) 20°C	16/12/2008 13:40	25	360.2	0.277
5	1200 (Unfiltered) 20°C	16/12/2008 13:43	25	383.5	0.238
6	1200 (Unfiltered) 20°C	16/12/2008 13:47	25	369.1	0.261
7	1200 (Unfiltered) 20°C	16/12/2008 14:00	25	366.8	0.238
8	1200 (Unfiltered) 20°C	16/12/2008 14:03	25	340.6	0.215
9	1200 (Unfiltered) 20°C	16/12/2008 14:06	25	323.9	0.245
Record Number	Sample Name	Measurement Date and Time	Temperature (°C)	Z-Average (nm)	PDI
1	1200 (Unfiltered) 40°C	16/12/2008 14:21	25	453.2	0.217
2	1200 (Unfiltered) 40°C	16/12/2008 14:24	25	432.7	0.256
3	1200 (Unfiltered) 40°C	16/12/2008 14:28	25	414.2	0.273
4	1200 (Unfiltered) 40°C	16/12/2008 14:31	25	406.4	0.249
5	1200 (Unfiltered) 40°C	16/12/2008 14:34	25	428.6	0.236
6	1200 (Unfiltered) 40°C	16/12/2008 14:38	25	417.5	0.254
7	1200 (Unfiltered) 40°C	16/12/2008 14:53	25	425	0.266
8	1200 (Unfiltered) 40°C	16/12/2008 14:56	25	410.3	0.272
9	1200 (Unfiltered) 40°C	16/12/2008 14:59	25	446.1	0.283

Particle sizing for HAp by DLS produced by sol-gel method (filtered)

Record Number	Sample Name	Measurement Date and Time	Temperature (°C)	Z-Average (nm)	PDI
1	200 (Filtered) 20°C	19/03/2009 16:56	25	219.8	0.132
2	200 (Filtered) 20°C	19/03/2009 17:00	25	213.9	0.115
3	200 (Filtered) 20°C	19/03/2009 17:05	25	201.4	0.133
4	200 (Filtered) 20°C	19/03/2009 17:10	25	215.9	0.118
5	200 (Filtered) 20°C	19/03/2009 17:14	25	218.8	0.131
6	200 (Filtered) 20°C	19/03/2009 17:19	25	207.2	0.115
7	200 (Filtered) 20°C	19/03/2009 17:25	25	219.7	0.156
8	200 (Filtered) 20°C	19/03/2009 17:30	25	216.9	0.108
9	200 (Filtered) 20°C	19/03/2009 17:34	25	185.1	0.14
Record Number	Sample Name	Measurement Date and Time	Temperature (°C)	Z-Average (nm)	PDI
1	200 (Filtered) 40°C	19/03/2009 18:57	25	222.9	0.136
2	200 (Filtered) 40°C	19/03/2009 19:00	25	205.2	0.124
3	200 (Filtered) 40°C	19/03/2009 19:03	25	221.7	0.12
4	200 (Filtered) 40°C	19/03/2009 19:06	25	209.5	0.115
5	200 (Filtered) 40°C	19/03/2009 19:09	25	222.7	0.124
6	200 (Filtered) 40°C	19/03/2009 19:12	25	223.1	0.132
7	200 (Filtered) 40°C	19/03/2009 19:18	25	221.9	0.112
8	200 (Filtered) 40°C	19/03/2009 19:21	25	219.8	0.135
9	200 (Filtered) 40°C	19/03/2009 19:24	25	220	0.127
Record Number	Sample Name	Measurement Date and Time	Temperature (°C)	Z-Average (nm)	PDI
1	1200 (Filtered) 20°C	20/03/2009 10:46	25	164.7	0.137
2	1200 (Filtered) 20°C	20/03/2009 10:51	25	152.9	0.115
3	1200 (Filtered) 20°C	20/03/2009 10:55	25	169	0.109
4	1200 (Filtered) 20°C	20/03/2009 11:00	25	154.5	0.124
5	1200 (Filtered) 20°C	20/03/2009 11:04	25	168.4	0.097
6	1200 (Filtered) 20°C	20/03/2009 11:08	25	160.8	0.115

7	1200 (Filtered) 20°C	20/03/2009 12:03	25	169.7	0.124
8	1200 (Filtered) 20°C	20/03/2009 12:08	25	162.3	0.14
9	1200 (Filtered) 20°C	20/03/2009 12:12	25	155.6	0.069
Record Number	Sample Name	Measurement Date and Time	Temperature (°C)	Z-Average (nm)	PDI
1	1200 (Filtered) 40°C	20/03/2009 15:48	25	174.4	0.14
2	1200 (Filtered) 40°C	20/03/2009 15:51	25	159.1	0.113
3	1200 (Filtered) 40°C	20/03/2009 15:56	25	162.3	0.13
4	1200 (Filtered) 40°C	20/03/2009 15:59	25	163.8	0.117
5	1200 (Filtered) 40°C	20/03/2009 16:02	25	177.2	0.119
6	1200 (Filtered) 40°C	20/03/2009 16:05	25	158.2	0.067
7	1200 (Filtered) 40°C	20/03/2009 16:08	25	163.5	0.101
8	1200 (Filtered) 40°C	20/03/2009 16:12	25	172.8	0.114
9	1200 (Filtered) 40°C	20/03/2009 16:15	25	167	0.068

Appendix for Chapter 4

Appendix 4 A

Phosphate calibration curve

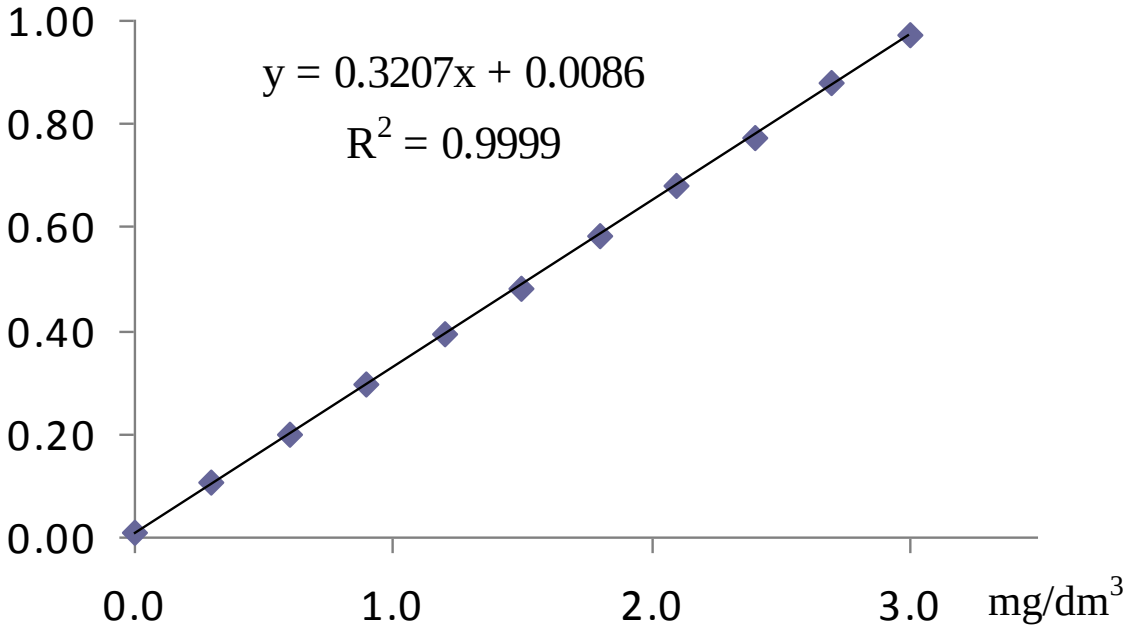

Phosphate determination of HAp was done by using Molybdate – vanadate reagent and its absorbance was determined photometrically at 400 nm. A 100 mg P/dm^3 solution was prepared by dissolving 0.11 g of KH_2PO_4 in 250 cm^3 of distilled water. Then, 100 cm^3 was transferred to a 250 cm^3 volumetric flask.

Known P concentrations (mg/dm^3),

P (mg)	**0.3**	**0.6**	**0.9**	**1.2**	**1.5**	**1.8**	**2.1**	**2.4**	**2.7**	**3.0**
Volume (ml)	7.5	15	22.5	30	37.5	45	52.5	60	67.5	75

For solubility of HAp in DMSO, absorbance obtained = 0.188, P = 0.5594 mg

Concentration of HAp in DMSO = 3.02 ± 0.02 mg

Appendix 4B

Particle sizing for HAp by DLS produced by GAS technique (filtered)

Record Number	Sample Name	Measurement Date and Time	Temperature (°C)	Z-Average (nm)	PDI
1	HAp 40, 150	17/8/2009 11:48	25	163.5	0.136
2	HAp 40, 150	17/8/2009 11:51	25	166.9	0.122
3	HAp 40, 150	17/8/2009 11:54	25	174.6	0.132
4	HAp 40, 150	17/8/2009 11:58	25	165.5	0.131
5	HAp 40, 150	17/8/2009 12:01	25	170.2	0.128
6	HAp 40, 150	17/8/2009 12:04	25	169.1	0.126
7	HAp 40, 150	17/8/2009 12:07	25	175.1	0.133
8	HAp 40, 150	17/8/2009 12:10	25	160.6	0.124
9	HAp 40, 150	17/8/2009 12:13	25	169.2	0.135
Record Number	Sample Name	Measurement Date and Time	Temperature (°C)	Z-Average (nm)	PDI
1	HAp 50, 150	17/8/2009 12:19	25	176.2	0.131
2	HAp 50, 150	17/8/2009 12:22	25	173.1	0.123
3	HAp 50, 150	17/8/2009 12:25	25	172.3	0.131
4	HAp 50, 150	17/8/2009 12:35	25	174.6	0.124
5	HAp 50, 150	17/8/2009 12:38	25	177.1	0.135
6	HAp 50, 150	17/8/2009 12:41	25	170.1	0.129
7	HAp 50, 150	17/8/2009 12:49	25	173.2	0.123
8	HAp 50, 150	17/8/2009 12:52	25	171.4	0.132
9	HAp 50, 150	17/8/2009 12:55	25	169.3	0.138
Record Number	Sample Name	Measurement Date and Time	Temperature (°C)	Z-Average (nm)	PDI
1	HAp 60, 150	17/8/2009 14:16	25	190.7	0.129
2	HAp 60, 150	17/8/2009 14:20	25	184.3	0.132
3	HAp 60, 150	17/8/2009 14:23	25	187.3	0.122

4	HAp 60, 150	17/8/2009 14:28	25	185.9	0.127
5	HAp 60, 150	17/8/2009 14:31	25	180.4	0.133
6	HAp 60, 150	17/8/2009 14:34	25	186.7	0.135
7	HAp 60, 150	17/8/2009 14:39	25	183.2	0.127
8	HAp 60, 150	17/8/2009 14:42	25	186.4	0.123
9	HAp 60, 150	17/8/2009 14:45	25	192.3	0.141
Record Number	Sample Name	Measurement Date and Time	Temperature (°C)	Z-Average (nm)	PDI
1	HAp 50, 100	17/8/2009 15:30	25	173.8	0.114
2	HAp 50, 100	17/8/2009 15:33	25	175	0.107
3	HAp 50, 100	17/8/2009 15:36	25	181.4	0.126
4	HAp 50, 100	17/8/2009 15:47	25	176.4	0.131
5	HAp 50, 100	17/8/2009 15:50	25	171.7	0.127
6	HAp 50, 100	17/8/2009 15:53	25	180.7	0.132
7	HAp 50, 100	17/8/2009 15:57	25	173.5	0.134
8	HAp 50, 100	17/8/2009 16:00	25	186.2	0.124
9	HAp 50, 100	17/8/2009 16:03	25	171.3	0.138
Record Number	Sample Name	Measurement Date and Time	Temperature (°C)	Z-Average (nm)	PDI
1	HAp 50, 200	17/8/2009 16:20	25	158.7	0.123
2	HAp 50, 200	17/8/2009 16:23	25	165.1	0.128
3	HAp 50, 200	17/8/2009 16:26	25	172.5	0.131
4	HAp 50, 200	17/8/2009 16:31	25	156	0.121
5	HAp 50, 200	17/8/2009 16:33	25	168.3	0.129
6	HAp 50, 200	17/8/2009 16:37	25	163.8	0.125
7	HAp 50, 200	17/8/2009 16:40	25	160.6	0.124
8	HAp 50, 200	17/8/2009 16:43	25	169.7	0.137
9	HAp 50, 200	17/8/2009 16:46	25	156.4	0.115

Particle sizing for HAp by DLS produced by SEDS technique (filtered)

Record Number	Sample Name	Measurement Date and Time	Temperature (°C)	Z-Average (nm)	PDI
1	HAp 40, 1, 20	24/8/2009 09:36	25	155.5	0.133
2	HAp 40, 1, 20	24/8/2009 09:39	25	150.4	0.127
3	HAp 40, 1, 20	24/8/2009 09:42	25	152.2	0.119
4	HAp 40, 1, 20	24/8/2009 09:50	25	147.1	0.124
5	HAp 40, 1, 20	24/8/2009 09:53	25	153.7	0.136
6	HAp 40, 1, 20	24/8/2009 09:57	25	156.3	0.131
7	HAp 40, 1, 20	24/8/2009 10:02	25	155	0.126
8	HAp 40, 1, 20	24/8/2009 10:05	25	150.2	0.119
9	HAp 40, 1, 20	24/8/2009 10:08	25	151.8	0.122
Record Number	Sample Name	Measurement Date and Time	Temperature (°C)	Z-Average (nm)	PDI
1	HAp 40, 1, 60	24/8/2009 10:28	25	130.5	0.123
2	HAp 40, 1, 60	24/8/2009 10:31	25	134.6	0.134
3	HAp 40, 1, 60	24/8/2009 10:34	25	133.3	0.127
4	HAp 40, 1, 60	24/8/2009 10:39	25	126.4	0.114
5	HAp 40, 1, 60	24/8/2009 10:42	25	131.2	0.135
6	HAp 40, 1, 60	24/8/2009 10:45	25	134.5	0.141
7	HAp 40, 1, 60	24/8/2009 10:50	25	135.3	0.129
8	HAp 40, 1, 60	24/8/2009 10:53	25	125.5	0.132
9	HAp 40, 1, 60	24/8/2009 10:56	25	131.8	0.119
Record Number	Sample Name	Measurement Date and Time	Temperature (°C)	Z-Average (nm)	PDI
1	HAp 40, 2, 40	24/8/2009 12:11	25	159.9	0.118
2	HAp 40, 2, 40	24/8/2009 12:14	25	150.4	0.122
3	HAp 40, 2, 40	24/8/2009 12:17	25	156.5	0.135
4	HAp 40, 2, 40	24/8/2009 12:22	25	156.3	0.133
5	HAp 40, 2, 40	24/8/2009 12:25	25	152.3	0.128
6	HAp 40, 2, 40	24/8/2009 12:28	25	146.2	0.12

7	HAp 40, 2, 40	24/8/2009 12:34	25	155.1	0.119
8	HAp 40, 2, 40	24/8/2009 12:37	25	159.4	0.127
9	HAp 40, 2, 40	24/8/2009 12:40	25	150.1	0.136
Record Number	Sample Name	Measurement Date and Time	Temperature (°C)	Z-Average (nm)	PDI
1	HAp 50, 1, 20	24/8/2009 12:50	25	161.2	0.133
2	HAp 50, 1, 20	24/8/2009 12:53	25	175.1	0.126
3	HAp 50, 1, 20	24/8/2009 12:56	25	165.3	0.123
4	HAp 50, 1, 20	24/8/2009 13:01	25	163.8	0.118
5	HAp 50, 1, 20	24/8/2009 13:04	25	168.9	0.128
6	HAp 50, 1, 20	24/8/2009 13:07	25	160.1	0.13
7	HAp 50, 1, 20	24/8/2009 13:11	25	167.6	0.125
8	HAp 50, 1, 20	24/8/2009 13:14	25	163.3	0.129
9	HAp 50, 1, 20	24/8/2009 13:17	25	169.5	0.133
Record Number	Sample Name	Measurement Date and Time	Temperature (°C)	Z-Average (nm)	PDI
1	HAp 50, 1, 60	24/8/2009 15:33	25	136.9	0.117
2	HAp 50, 1, 60	24/8/2009 15:36	25	143.3	0.125
3	HAp 50, 1, 60	24/8/2009 15:39	25	140.4	0.128
4	HAp 50, 1, 60	24/8/2009 15:43	25	141.1	0.134
5	HAp 50, 1, 60	24/8/2009 15:46	25	147.6	0.13
6	HAp 50, 1, 60	24/8/2009 15:49	25	133.3	0.126
7	HAp 50, 1, 60	24/8/2009 15:55	25	146.4	0.119
8	HAp 50, 1, 60	24/8/2009 15:58	25	140.1	0.127
9	HAp 50, 1, 60	24/8/2009 16:01	25	144.2	0.132
Record Number	Sample Name	Measurement Date and Time	Temperature (°C)	Z-Average (nm)	PDI
1	HAp 50, 2, 40	24/8/2009 16:12	25	166.8	0.126
2	HAp 50, 2, 40	24/8/2009 16:15	25	162.3	0.118
3	HAp 50, 2, 40	24/8/2009 16:18	25	169.4	0.132
4	HAp 50, 2, 40	24/8/2009 16:22	25	161.3	0.133
5	HAp 50, 2, 40	24/8/2009 16:25	25	159.7	0.124

6	HAp 50, 1, 60	24/8/2009 16:28	25	166.5	0.128
7	HAp 50, 1, 60	24/8/2009 16:33	25	160.2	0.13
8	HAp 50, 1, 60	24/8/2009 16:36	25	164.4	0.119
9	HAp 50, 1, 60	24/8/2009 16:39	25	167.8	0.122

Appendix for Chapter 5

Particle sizing for Ca/P by DLS produced by direct precipitation method (filtered)

Record Number	Sample Name	Measurement Date and Time	Temperature (°C)	Z-Average (nm)	PDI
1	Ca/P 0.40	14/4/2010 10:05	25	213.8	0.13
2	Ca/P 0.40	14/4/2010 10:08	25	216.5	0.121
3	Ca/P 0.40	14/4/2010 10:11	25	218.6	0.128
4	Ca/P 0.40	14/4/2010 10:15	25	214.7	0.117
5	Ca/P 0.40	14/4/2010 10:18	25	215.9	0.124
6	Ca/P 0.40	14/4/2010 10:21	25	217.8	0.129
7	Ca/P 0.40	14/4/2010 10:26	25	216.6	0.132
8	Ca/P 0.40	14/4/2010 10:29	25	214.3	0.133
9	Ca/P 0.40	14/4/2010 10:32	25	217.3	0.118
Record Number	Sample Name	Measurement Date and Time	Temperature (°C)	Z-Average (nm)	PDI
1	Ca/P 0.75	14/4/2010 10:40	25	213.3	0.142
2	Ca/P 0.75	14/4/2010 10:43	25	218.9	0.134
3	Ca/P 0.75	14/4/2010 10:46	25	215.1	0.126
4	Ca/P 0.75	14/4/2010 10:51	25	215.4	0.135
5	Ca/P 0.75	14/4/2010 10:54	25	211.2	0.129
6	Ca/P 0.75	14/4/2010 10:57	25	214.5	0.117
7	Ca/P 0.75	14/4/2010 11:02	25	210.7	0.122
8	Ca/P 0.75	14/4/2010 11:05	25	216.4	0.128

9	Ca/P 0.75	14/4/2010 11:08	25	213.1	0.116
Record Number	Sample Name	Measurement Date and Time	Temperature (°C)	Z-Average (nm)	PDI
1	Ca/P 1.00	14/4/2010 11:12	25	218.1	0.117
2	Ca/P 1.00	14/4/2010 11:15	25	211.8	0.131
3	Ca/P 1.00	14/4/2010 11:18	25	216.2	0.128
4	Ca/P 1.00	14/4/2010 11:22	25	212.5	0.124
5	Ca/P 1.00	14/4/2010 11:25	25	219.3	0.133
6	Ca/P 1.00	14/4/2010 11:28	25	214.5	0.139
7	Ca/P 1.00	14/4/2010 11:34	25	212.8	0.123
8	Ca/P 1.00	14/4/2010 11:37	25	221.7	0.119
9	Ca/P 1.00	14/4/2010 11:40	25	211.4	0.126
Record Number	Sample Name	Measurement Date and Time	Temperature (°C)	Z-Average (nm)	PDI
1	Ca/P 1.33	14/4/2010 12:00	25	215.6	0.124
2	Ca/P 1.33	14/4/2010 12:03	25	217.8	0.128
3	Ca/P 1.33	14/4/2010 12:06	25	212.3	0.133
4	Ca/P 1.33	14/4/2010 12:11	25	214.5	0.141
5	Ca/P 1.33	14/4/2010 12:14	25	216.3	0.129
6	Ca/P 1.33	14/4/2010 12:17	25	213.4	0.117
7	Ca/P 1.33	14/4/2010 12:21	25	216.2	0.121
8	Ca/P 1.33	14/4/2010 12:24	25	213.8	0.136
9	Ca/P 1.33	14/4/2010 12:27	25	210.1	0.126
Record Number	Sample Name	Measurement Date and Time	Temperature (°C)	Z-Average (nm)	PDI
1	Ca/P 1.67	14/4/2010 15:36	25	220.9	0.14
2	Ca/P 1.67	14/4/2010 15:39	25	211.8	0.131
3	Ca/P 1.67	14/4/2010 15:42	25	219.5	0.126
4	Ca/P 1.67	14/4/2010 15:46	25	218.7	0.122

5	Ca/P 1.67	14/4/2010 15:49	25	221.6	0.118
6	Ca/P 1.67	14/4/2010 15:52	25	214.8	0.123
7	Ca/P 1.67	14/4/2010 15:57	25	205.8	0.13
8	Ca/P 1.67	14/4/2010 16:00	25	224.1	0.125
9	Ca/P 1.67	14/4/2010 16:03	25	220.3	0.128
Record Number	Sample Name	Measurement Date and Time	Temperature (°C)	Z-Average (nm)	PDI
1	Ca/P 2.50	14/4/2010 16:13	25	221.9	0.129
2	Ca/P 2.50	14/4/2010 16:16	25	207.8	0.134
3	Ca/P 2.50	14/4/2010 16:19	25	222.7	0.118
4	Ca/P 2.50	14/4/2010 16:24	25	218.8	0.127
5	Ca/P 2.50	14/4/2010 16:27	25	222.6	0.131
6	Ca/P 2.50	14/4/2010 16:30	25	221.5	0.124
7	Ca/P 2.50	14/4/2010 16:34	25	207.2	0.136
8	Ca/P 2.50	14/4/2010 16:37	25	224	0.129
9	Ca/P 2.50	14/4/2010 16:40	25	221.8	0.116

Particle sizing for Ca/P by DLS produced by SEDS method (filtered)

Record Number	Sample Name	Measurement Date and Time	Temperature (°C)	Z-Average (nm)	PDI
1	Ca/P 0.33	19/5/2010 10:33	25	217.8	0.121
2	Ca/P 0.33	19/5/2010 10:36	25	214.5	0.126
3	Ca/P 0.33	19/5/2010 10:39	25	218.9	0.139
4	Ca/P 0.33	19/5/2010 10:45	25	218.3	0.117
5	Ca/P 0.33	19/5/2010 10:48	25	219.8	0.125
6	Ca/P 0.33	19/5/2010 10:51	25	216.6	0.128
7	Ca/P 0.33	19/5/2010 10:55	25	219.7	0.133
8	Ca/P 0.33	19/5/2010 10:58	25	212.5	0.141
9	Ca/P 0.33	19/5/2010 11:01	25	219.5	0.127
Record Number	Sample Name	Measurement Date and Time	Temperature (°C)	Z-Average (nm)	PDI
1	Ca/P 1.00	19/5/2010 11:10	25	211.5	0.118
2	Ca/P 1.00	19/5/2010 11:13	25	220.8	0.127
3	Ca/P 1.00	19/5/2010 11:16	25	218.6	0.13
4	Ca/P 1.00	19/5/2010 11:21	25	217.9	0.131
5	Ca/P 1.00	19/5/2010 11:24	25	207.3	0.126
6	Ca/P 1.00	19/5/2010 11:27	25	219.6	0.123
7	Ca/P 1.00	19/5/2010 11:32	25	218.6	0.121
8	Ca/P 1.00	19/5/2010 11:35	25	215.9	0.116
9	Ca/P 1.00	19/5/2010 11:38	25	205.7	0.135
Record Number	Sample Name	Measurement Date and Time	Temperature (°C)	Z-Average (nm)	PDI
1	Ca/P 3.00	19/5/2010 11:44	25	218.3	0.14
2	Ca/P 3.00	19/5/2010 11:47	25	220.6	0.128

3	Ca/P 3.00	19/5/2010 11:50	25	216.4	0.131
4	Ca/P 3.00	19/5/2010 11:55	25	218.7	0.122
5	Ca/P 3.00	19/5/2010 11:58	25	214.9	0.116
6	Ca/P 3.00	19/5/2010 12:01	25	219.8	0.138
7	Ca/P 3.00	19/5/2010 12:05	25	219.5	0.134
8	Ca/P 3.00	19/5/2010 12:08	25	214.7	0.126
9	Ca/P 3.00	19/5/2010 12:11	25	205.8	0.136

Appendix for Chapter 6

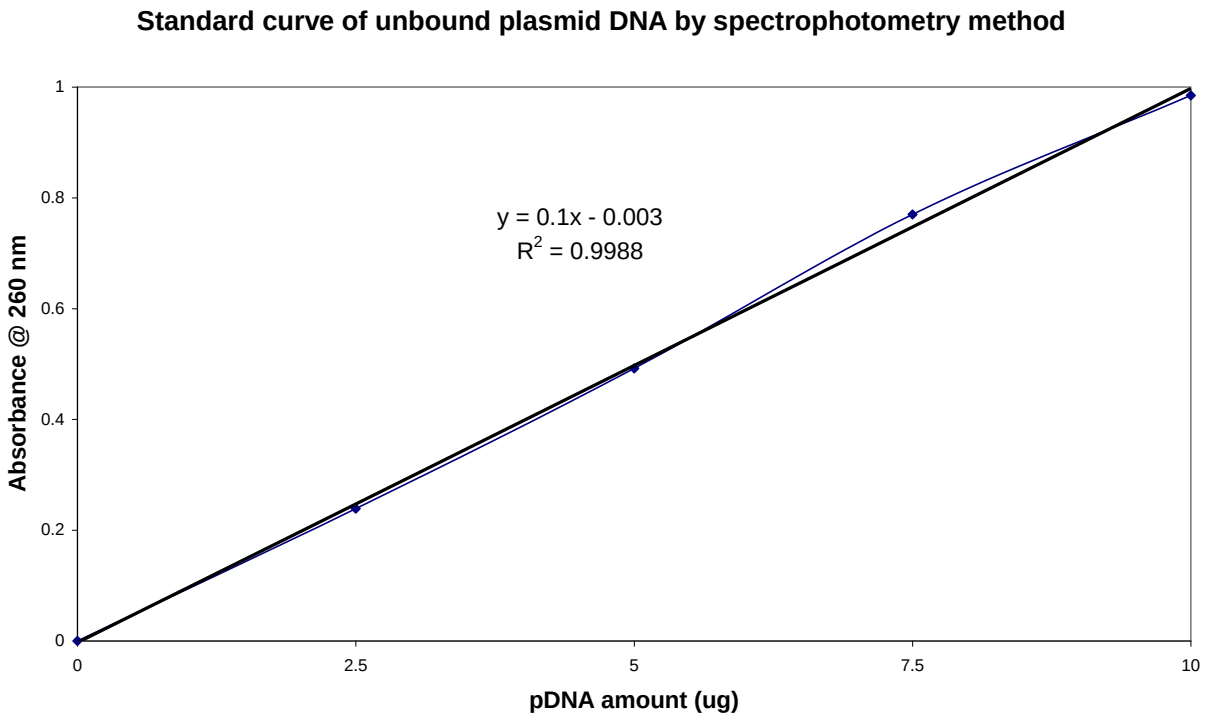

Calculation for the determination of post- co-precipitation bound pDNA onto a CaP sample for the Sol-gel method at 200 rpm and 20 ^{o}C is shown below:

Mass balance of pDNA (equation from the standard curve),

Value of supernatant obtained by spectrometry, $y = mx + c$

$0.154^{*} = 0.100\ x - 0.003$

$0.154 + 0.003 = 0.100\ x$

$0.157 = 0.100\ x$

$x = 1.570$ µg

* absorbance reading from spectrophotometry

pDNA unbound (%) = 1.570 µg / 10 µg = 15.70 % ≈ 16 %

pDNA bound (%) = (100 – 16) % = 84 %

Tabulated data for the determination of post- co-precipitation bound pDNA onto CaP samples

CaP sample	Absorbance reading from spectrophotometry	Amount of unbound pDNA (µg) (Initial amount of 10 µg pDNA)	Percentage of bound pDNA
1) Sol-gel method at 200 rpm and 40 ^{o}C.	0.180	1.830	82 %
2) Sol-gel method at 2200 rpm and 20 ^{o}C.	0.112	1.150	88 %
3) Sol-gel method at 2200 rpm and 40 ^{o}C.	0.125	1.280	87 %
4) Sol-gel method at 7000 rpm and 20 ^{o}C.	0.088	0.910	91 %
5) Sol-gel method at 7000 rpm and 40 ^{o}C.	0.076	0.790	92 %
6) GAS method at 40 ^{o}C and 150 bar.	0.146	1.490	85 %
7) GAS method at 50 ^{o}C and 150 bar.	0.152	1.550	84 %
8) GAS method at 60 ^{o}C and 150 bar.	0.172	1.750	82 %
9) GAS method at 50 ^{o}C and 100 bar.	0.159	1.620	84%
10) GAS method at 50 ^{o}C and 200 bar.	0.134	1.370	86 %
11) SEDS method at 40 ^{o}C, solvent flowrate of 1 ml/min and 60 g/min of CO_2.	0.057	0.600	94 %

12) SEDS method at 40 ^{o}C, solvent flowrate of 2 ml/min and 60 g/min of CO_2.	0.118	1.210	88 %
13) SEDS method at 50 ^{o}C, solvent flowrate of 1 ml/min and 60 g/min of CO_2.	0.077	0.800	92 %
14) SEDS method at 50 ^{o}C, solvent flowrate of 2 ml/min and 60 g/min of CO_2.	0.141	1.440	86 %
15) New CaP route at 0.40 Ca/P ratio.	0.201	2.040	80 %
16) New CaP route at 0.75 Ca/P ratio.	0.174	1.770	82 %
17) New CaP route at 1.00 Ca/P ratio.	0.169	1.720	83 %
18) New CaP route at 1.33 Ca/P ratio.	0.162	1.650	83 %
19) New CaP route at 1.67 Ca/P ratio.	0.165	1.680	83 %
20) New CaP route at 2.50 Ca/P ratio.	0.170	1.730	83 %
21) New CaP route at 0.33 Ca/P ratio by SEDS.	0.211	2.140	79 %
22) New CaP route at 1.00 Ca/P ratio by SEDS.	0.167	1.700	83%
23) New CaP route at 3.00 Ca/P ratio by SEDS.	0.171	1.740	83 %